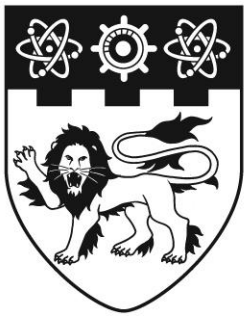

NANYANG TECHNOLOGICAL UNIVERSITY

Near-IR and Mid-IR (1.55 μm – 2 μm) Silicon Photonics Devices on Silicon-on-Insulator (SOI) Platform

ZHANG ZECEN

School of Electrical & Electronic Engineering

2018

Near-IR and Mid-IR (1.55 µm – 2 µm) Silicon Photonics Devices on Silicon-on-Insulator (SOI) Platform

ZHANG ZECEN

School of Electrical & Electronic Engineering

A thesis submitted to the Nanyang Technological University

in partial fulfillment of the requirements for the degree of

Doctor of Philosophy

2018

Statement of Originality

I hereby certify that the work embodied in this thesis is the result of original research and has not been submitted for a higher degree to any other university or institution.

---------- ----------

Date Zhang Zecen

Acknowledgements

The works presented in this thesis would not have been possible without the help of many others. It is my great honor to study and work as a PhD candidate in such a friendly, creative and energetic research group of Nanyang Technological University in the past few years. These years are impressive and meaningful experience in my whole life. Here I would like to sincerely show my gratefulness to those individuals who have helped me in the pursuit of PhD degree.

First and foremost, I am deeply grateful to my supervisor Professor Ng Geok Ing. Owing to his visionary foresight, rich experience and patient guidance, I learned to consider problems and conduct experiments in an effective and efficient way. These precious experience would be a priceless treasure for my future career. I would like to thank Professor Wang Hong, Dr. Liu Chongyang, and Mrs. Tina. They have offered me the necessary experimental resources to enable me to carry out my experiments effectively. I am also grateful to Dr. Hu Ting, Dr. Qiu Haodong and Dr. Wang Wanjun who have helped me in the field of silicon photonics and patiently tolerated my endless questioning with their expertise in these years. They are excellent mentors and elder brothers who give me a lot of help both on life and research work. I also would like to thank Dr. Liu Zhihong, Dr. Ye Gang, Dr. Li Yang, Dr. Qiao Zhongliang, Dr. Mohamed S. Rouifed, Dr. Xing Weichuan, Dr. Bao Shuyu, Li Xiang, Li Wei, Zhou Jin, Sia Jiaxu and Zheng Yi who have taught and helped me with various clean-room fabrication processes, which significantly facilitated my research. As close friends,

they also support me a lot in my PhD student life. Besides, I am grateful to all the collaborators from Optoelectronics Research Centre of University of Southampton for the support and help in my research. As the pioneers and experts in the field of silicon photonics, Professor Graham T. Reef, Dr. Callum G. Littlejohns, and Dr. Milos Nedeljkovic have shared their unique viewpoints and fruitful discussions with me.

Of course, I would not underestimate the contribution of all the lab technicians, Muhd Fauzi Bin Abudullah and Seet Lye Ping in the Characterization Lab, Mohamad Shamsul Bin Mohamad, Mak Foo Wah, Chuang Kwok Fai, Yang Xiaohong, Ngo Ling Ling, Chong Gang Yih, Irene Chia Ai Lay etc. in the Nanyang Nano-Fabrication Center for the professional maintenance of the equipments, which is very crucial for the device fabrication.

Finally, I would like to thank my parents for their selfless love, and my fiancée Xu Yimeng for her encouragement and devotion to me.

Abstract

In the last several decades, there has been considerable research interest in silicon photonics based on silicon-on-insulator (SOI) platform. Many useful applications have been developed in the near-infrared (NIR) data- and tele- communication band (1.3-1.6 μm), such as sensors, switches, modulators, and various passive devices. Furthermore, the mid-infrared (MIR, 2-15 μm) band is also very crucial as many gases and molecules have unique absorption fingerprints in this regime. Hence there is enormous interest in practical realization of passive and optoelectronic devices operating in the MIR range, including optical sensing and environmental monitoring, free-space communications, bio-medical and thermal imaging. Besides, 2 μm wavelength is a promising solution to extend the operating wavelength of communication system to short MIR wavelengths. The objective of this project is to develop SOI platform-based on-chip photonic devices including passive devices, sensors and optical modulators operating in the NIR and MIR bands.

In order to build various photonic systems, several key on-chip fundamental passive components operating at 2 μm wavelength are developed and analyzed at the beginning of this project. These fundamental building blocks include waveguides, grating couplers, and microring resonators. These components are successfully fabricated with good performance. For example, the grating coupler operating at 2 μm wavelength was firstly fabricated and experimentally measured with a loss of 6.5 dB, which is comparable to the widely used grating couplers operating at 1.55 μm

communication band. The extinction ratio (ER) and the quality factor (Q factor) of the compact microring resonator (radius = 10 μm) integrated with above grating couplers were firstly measured as 12 dB and 11200 respectively.

As a practical method to improve the performance of sensors and modulators, Fano devices with sharp asymmetric transmission lineshape and electromagnetically induced transparency (EIT) devices with time delay at the narrow optical transparency peak residing in a broader transmission absorption valley are designed, fabricated and characterized. In this work, an EIT transmission lineshape was experimentally generated with an all-pass microring-Bragg grating coupled resonant system for the first time. Based on the same system, the conversion between EIT and Fano transmissions was experimentally verified and the inner mechanism was discussed in detail. Subsequently, tunable and convertible EIT and Fano transmissions were experimentally realized in a Mach–Zehnder interferometer (MZI)-assisted microring-Bragg grating based coupling resonant system, which is believed to be the first report of its kind.

Optical filters are also vital for modulators. For the dual-band optical filter (DBOF), since it can double the available modulating channels, it is also an effective solution to improve the efficiency of signal processing. In this work, two types of DBOFs based on partially-reflective-element-embedded microring resonators were theoretically and experimentally demonstrated for the first time. As measured, the separation between two resonance dips and the insertion loss are 0.5 nm and <0.5 dB

respectively. The Q factors of the two dips achieve 30900 and 34400 respectively. The performance is comparable to the up-to-date reported works.

By utilizing the fundamental building blocks and taking the advantages of suspended structure, the bio-chemical sensor operating at 2 μm wavelength based on a suspended microracetrack resonator with sub-wavelength-grating (SWG) lateral metamaterial cladding is designed, fabricated and characterized for the first time. The expected sensitivity of the fundamental TE mode was calculated as 337.5 nm/RIU. This is believed to be the first demonstration of on-chip photonic bio-chemical sensor operating at 2 μm wavelength with sensitivity comparable to the latest reported results at 1.55 μm wavelength.

With additional implantation and electrode fabrication processes, thermal-optic (TO) and electro-optic (EO) modulators operating at 2 μm wavelength were also experimentally demonstrated for the first time. The DC shifting rate and the -3 dB bandwidth of the TO modulator are measured as 0.05 nm/V and ~30.8 KHz respectively. The -3 dB bandwidth of the EO modulator is measured as >12.5 GHz. The eye-diagrams at the speed of 5 Gb/s, 7.5 Gb/s, 10 Gb/s and 12.5 Gb/s are measured. And the SNR at 12.5 Gb/s was calculated as 8.325. Although the preliminary performance of these modulators is not as good as the latest reported modulators operating in the NIR communication band, they pave the way for extending the operating wavelength of communication system to short MIR wavelengths.

Table of Contents

List of Figures

Chapter 1
Introduction

1.1 Motivation: Why Silicon Photonics in NIR and MIR

In the past decades, silicon photonics has attracted considerable research interests, as they can be used in many applications, such as revolutionary short-reach interconnects [1-4], signal processing [5-10], and compact bio-chemical sensors [11-14]. So far, majority of the research effort in Si photonics is focused on tele- and data-communication wavelengths between 1.3 and 1.6 μm. With the advantages of the compatibility with mature industrial standard complementary-metal-oxide-semiconductor (CMOS) fabrication process, the fabrication cost of silicon photonic devices can be greatly reduced. Besides, large volume monolithic integration and versatile silicon photonic systems become possible as various functional and compact components are developed [15-17]. Many commercial silicon photonic products have been developed and launched in the commercial market, such as 100G optical transceivers from Intel, variable optical attenuators from Kotura, active optical cables from Luxtera, and bio-chemical detectors from Genalyte. Hence, to-date, photonics components and systems operating at NIR have been well developed and adopted in many applications.

In addition to the NIR band, the mid-infrared (MIR, λ = 2 - 20 μm) regime is also a very crucial band as many molecules have unique absorption fingerprints in this

regime. Hence there is enormous interest to realize practical passive and optoelectronic devices operating in the MIR range for applications such as optical sensing and environmental monitoring, free-space communications, bio-medical and thermal imaging [18-20]. There are two atmospheric transmission windows (3 - 5 μm and 8 - 15 μm) in MIR range, which can be utilized for low loss free-space communications. The MIR detectors can be used in both civil and military for "home security" with bio-medical and thermal imaging. In addition, this spectral range is attractive for highly precise surgical procedures and medical ablation of tissue because of its high absorption in water, and hence small penetration depths, especially for wavelengths around 3 μm where the penetration depth can be as small as a few microns [21]. Besides, 2 μm wavelength is also a promising solution to extend the operating wavelength of communication system to short MIR wavelengths. Therefore, MIR is a very useful wavelength regime which needs further exploration.

Although in the last decades, high power, room temperature-operational MIR light sources and sensitive mid-IR detectors have been developed. Limited work has been reported in developing the passive and active silicon photonic components for the MIR [22], especially for the silicon based devices working at 2 μm wavelength. In fact, silicon has many advantages in fabricating devices for 2 μm wavelength. Firstly, silicon widely exists in nature and easily obtainable hence the cost is low. Secondly, as shown in Fig. 1.1, the transmission curve of a 5 mm-thick Si sample is plotted as a function of the wavelengths from 1 μm to 25 μm [23]. As seen, silicon has the highest

transmission at the wavelengths from 2 - 5 μm, which acts as an excellent material for carrying and guiding light. Furthermore, it is also compatible with the extremely well-developed industrial standard CMOS fabrication techniques; hence, silicon-based devices and on-chip integrated photonic circuits can be fabricated at a low cost.

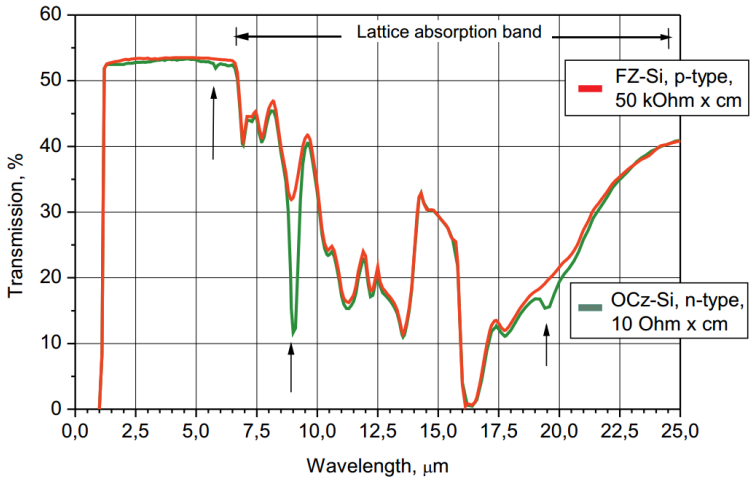

Fig.1.1 The transmission curve of a 5 mm-thick Si sample.

Besides, the need for high volume of transmitting information has increased tremendously. Dense Wavelength Division Multiplexing (DWDM) performs as an important method to realize the multiple-channel transmission of information by using different wavelengths of laser light. But the limitation of DWDM is the available wavelengths range, which is focused at wavelengths of 1.3 - 1.6 μm. Due to the increasing demands for higher bandwidth, more channels and available wavelengths are needed. The low absorption of 2 μm wavelengths makes these wavelengths good candidates for expanding the range of WDM, which can also increases the volume of information transmission [24,25]. In order to utilize the 2 μm wavelength, modulators are the key devices needed to be developed. For this wavelength, limited work on

modulators has been reported. R. Soref calculated the functions and parameters for free-carrier electro-refraction and electro-absorption modulation for silicon over 1-14 μm [26], which can be a useful tool to simulate and predict the performance of modulation. Besides, thermal modulation could be an option but the speed is much lower than electro-optic modulation.

Hence, in this work, the main objectives are on the development and improvement of core components of photonic integrated circuits, such as passive devices, sensors and modulators, operating in NIR and MIR regime on silicon-on-insulator (SOI) platform.

1.2 Silicon-on-Insulator Platform and Waveguide Theory

Photonic integrated circuits (PIC) consist of many basic components, such as couplers, waveguides, micro-resonators, Bragg gratings etc.. In Fig. 1.2, a typical PIC is shown. All these optic components are based on the confinement of light in these photonics structures and the total reflection.

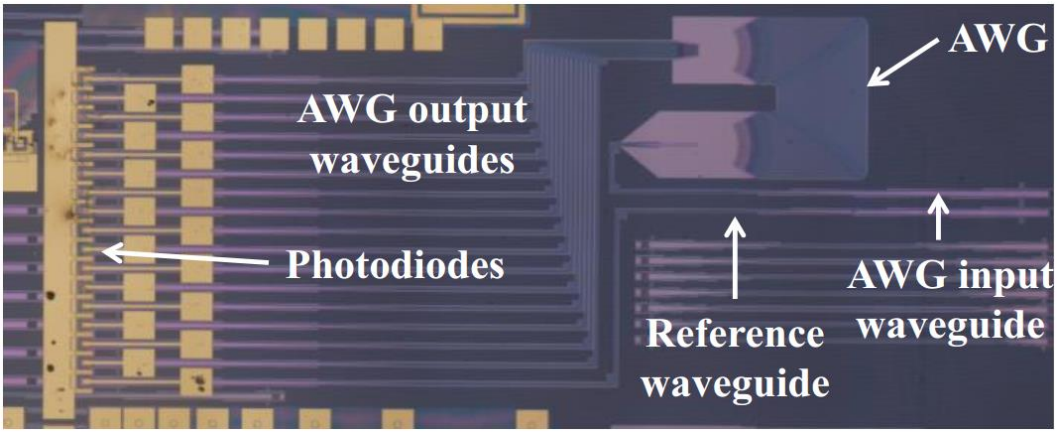

Fig.1.2 A typical PIC [27].

As shown in Fig. 1.3, in a commercial SOI wafer, due to the large refractive index between the cladding/substrate layer and the silicon layer, total reflections are able to occur at the boundary. The cladding layer material can be different from the substrate, such as in sensors the cladding layer can be air or various testing chemicals. In an original SOI wafer, the light can be confined in the vertical direction by the upper and lower boundaries. But due to the lack of confinement in lateral direction, the light will suffer a high propagation loss, which means the light cannot be guided to transmit for a long distance. In order to have a guided light (guided mode), lateral and vertical confinement are both needed. The fundamental structure that can guide light through a long distance with a low propagation loss is waveguide.

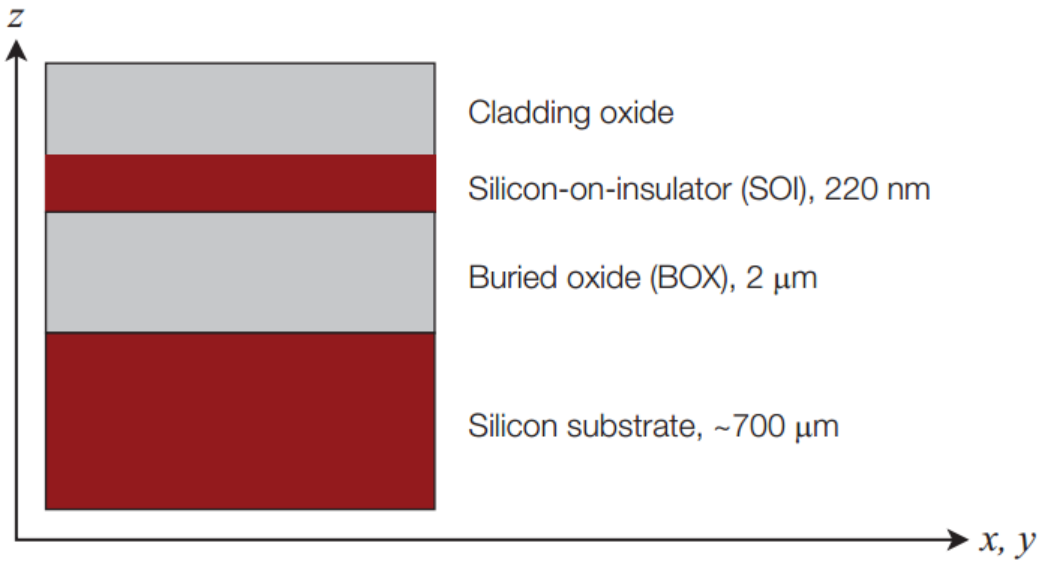

Fig.1.3 The cross-section schematic of one kind of commercial SOI wafers with SiO_2 upper cladding layer [28].

Two kinds of widely used waveguides on SOI platform, strip waveguide and rib

waveguide, are demonstrated in Fig. 1.4. With the total reflection of light at the sidewalls of waveguides caused by the large difference of refractive index between Si and SiO_2, light can propagate through a long distance with a low propagation loss (generally ~3 dB/cm). For strip waveguides, the lateral confinement is better thus one can avoid radiation loss when bending structures are utilized. For rib waveguides, the existence of slab is crucial for the conductivity of the modulating electric signal. Once the light is guided with a low transmission loss, various functions can be realized by developing new combinations.

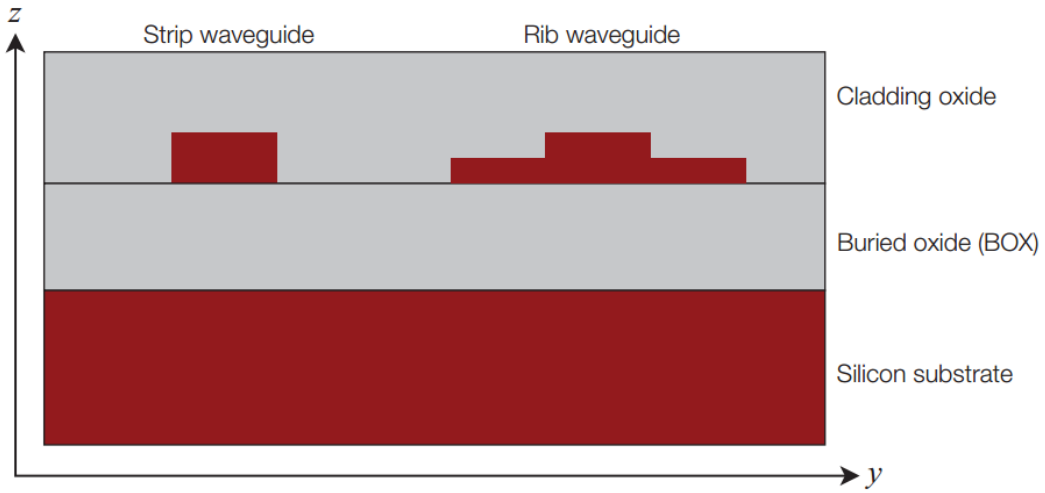

Fig.1.4 The schematic of strip waveguide and rib waveguide [28].

1.3 Silicon Photonics Applications

While we have the waveguides to carry and guide the light, we still need to inject light into these structures. Conventionally, grating coupling and butt coupling are widely adopted. Butt coupling is based on tapers, which are utilized to gather the light

mode from the fiber and transform the light mode to the guided mode for transmission in waveguides. But due to the absence of natural cleavage plane, in order to maintain a low reflective loss at the surface, polishing process is needed, which is time-consuming and has the risk of contaminations. In contrast, grating coupling is more robust and reliable method. Grating coupler is a periodic structure utilizing the interference of light diffracted from free-space into waveguide to get high efficiency of coupling. As shown in Fig. 1.5, the size of pitch, duty-cycle, the etching depth and input/output angle need to be carefully designed. Grating couplers have the advantages of more straightforward back-end process, convenience for coupling light in and out from any location on the chip and potentially low coupling loss [29]. Besides, grating coupler can be designed intentionally as a mode filter to let only TE or TM mode coupling in/out, which is quite crucial for some polarization dependent applications.

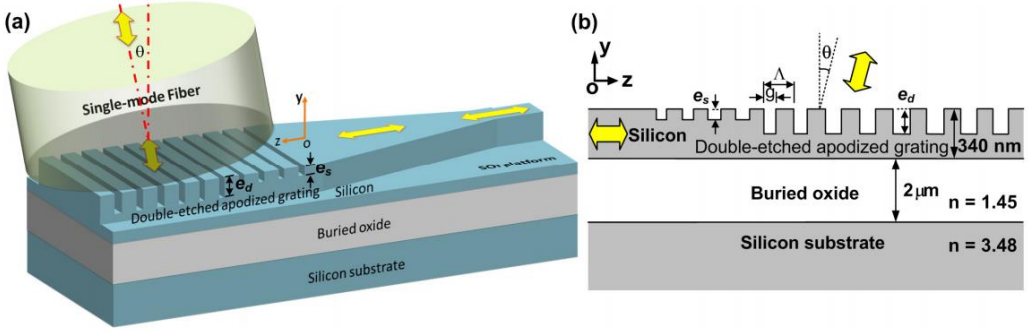

Fig.1.5 The schematic of one kind of grating coupler [30].

Micro-resonator is a complex but very useful device. It is based on confining light in a cavity and forming resonances, hence to get various transmission spectra. Microring resonator and microdisk resonator are two kinds of very typical structures to achieve

this goal. For microring resonators, they are divided into two groups depending on with or without add-drop bus waveguide. However, the basic principles of these two kinds of microring resonators are similar. For a microring with the radius of r, the optical path length difference (OPD) for a round trip can be calculated by

$$\mathrm{OPD} = 2 * \pi * \mathrm{r} * n_{eff} \tag{1.3}$$

where n_{eff} is the effective index of waveguide decided by the waveguide dimension and the cladding material. The condition of generating resonance in microring is

$$\mathrm{OPD} = \mathrm{m} * \lambda_m \tag{1.4}$$

where m is an integer and λ_m is the corresponding wavelength of m. It means the OPD must be an integral multiple of the corresponding wavelength so that the resonance can be formed in the microring. As shown in Fig. 1.6, an all-pass microring (APMRR) has only one input-pass waveguide for coupling into and out from the microring. In contrast, an add-drop micro-ring (ADMRR) has one more add-drop bus waveguide. Generally, because of the presence of add-drop bus waveguide, the system is always operating in the under-coupling regime.

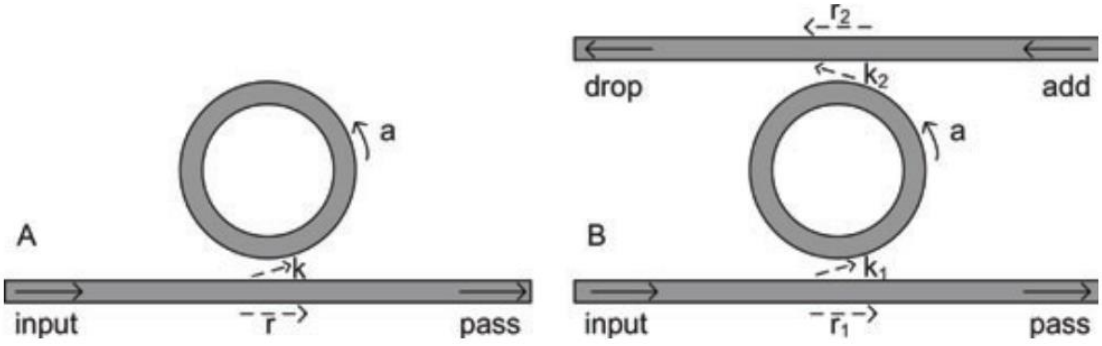

Fig.1.6 The schematic of all-pass microring resonator (left) and add-drop microring resonator (right) [31].

As shown in Fig. 1.7, microdisk resonators are based on a similar working principle as microring resonators. The difference is that the light in microdisk does not propagate with the reflections at both two sidewalls of waveguides as in the microring resonators. The reflection only happens at the edge sidewall of microdisk, which is called whispering gallery mode. The less reflections gives microdisk resonators much higher quality factor (Q factor), a parameter usually utilized for describing the sharpness of transmission spectrum, as less scattering loss. However, accompany with this advantage, the problem is that the coupling efficiency is lower than microring resonators. And due to the extreme high Q factor, when using microdisk to build a modulator, the modulating speed cannot be very high.

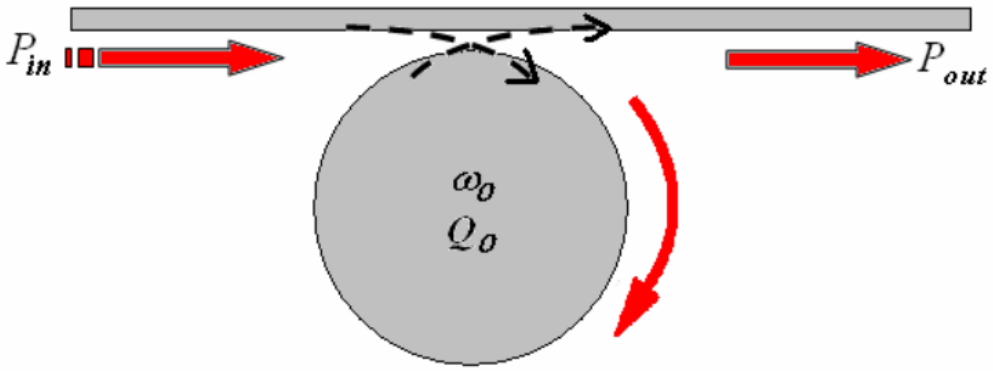

Fig.1.7 The schematic of microdisk resonator [32].

Based on these microring and microdisk resonators, various applications have been developed. Sensors are one of the most useful passive applications. Two kinds of microring sensors have been widely used: bio-chemical sensors and temperature sensors. One of the bio-chemical sensing methods is based on the change of refractive

index of cladding materials, which results in the change of effective index of the waveguide (n_{eff}). Consequently, OPD is changed and the resonant dips will shift at the same time. As shown in Fig. 1.8, while measuring the transmission at the original wavelength of the resonant dip, the transmission will change due to the shifting of the resonant dip so that the sensing can be realized. Besides, the temperature sensing is based on the large thermal-dependent refractive index of silicon. While the temperature of silicon is changed, the refractive index is also changed as well as the effective index of the waveguides. Similarly, the resonant dips will shift and the transmission at the original resonant dips will also change. As a result, the sensing can be realized.

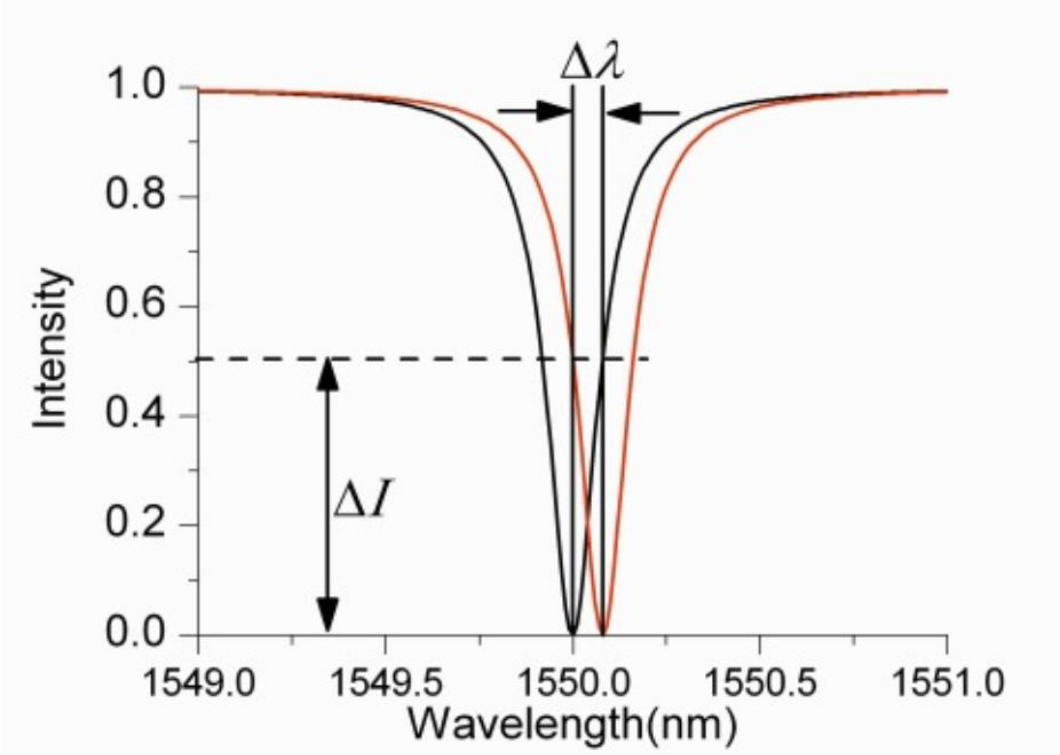

Fig.1.8 The transmission spectra of sensing applications [32].

Bragg grating is also a very useful structure, which has periodic corrugations at the

two sidewalls of a waveguide to generate partial reflection. As shown in Fig. 1.9, when light propagate through each one period of grating, part of light will be reflected and the rest will transmit through. Two Bragg gratings on one waveguide can form a Fabry-Perot (F-P) resonator, which is useful for building some coupling resonant system with other resonators, such as microring resonators.

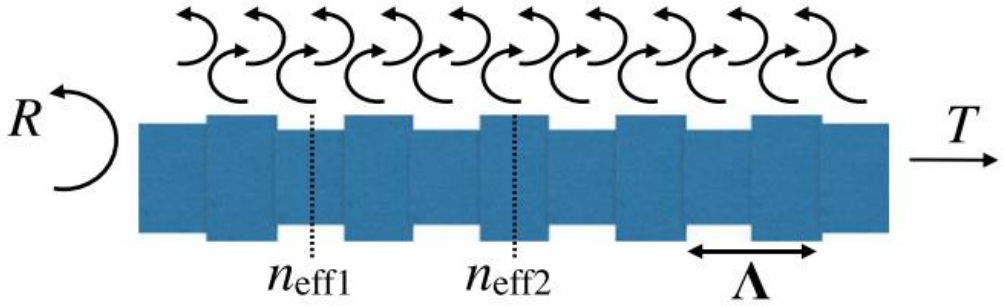

Fig.1.9 The schematic of Bragg grating [28].

When the passive components discussed above are prepared, doped regions and electrodes can be fabricated on microring or microdisk resonators with implantation and metal deposition processes. With the slabs beside the rib waveguide, free carriers can be conducted between the electrodes and the waveguide. As shown in Fig. 1.10, when voltage is applied at the two sides of the waveguide, free carriers can be injected or depleted from the waveguides. According to the free carrier plasma effect, the effective refractive index of waveguide will be changed correspondingly and subsequently the resonance peak will be shifted. This in turn will switch the transmission.

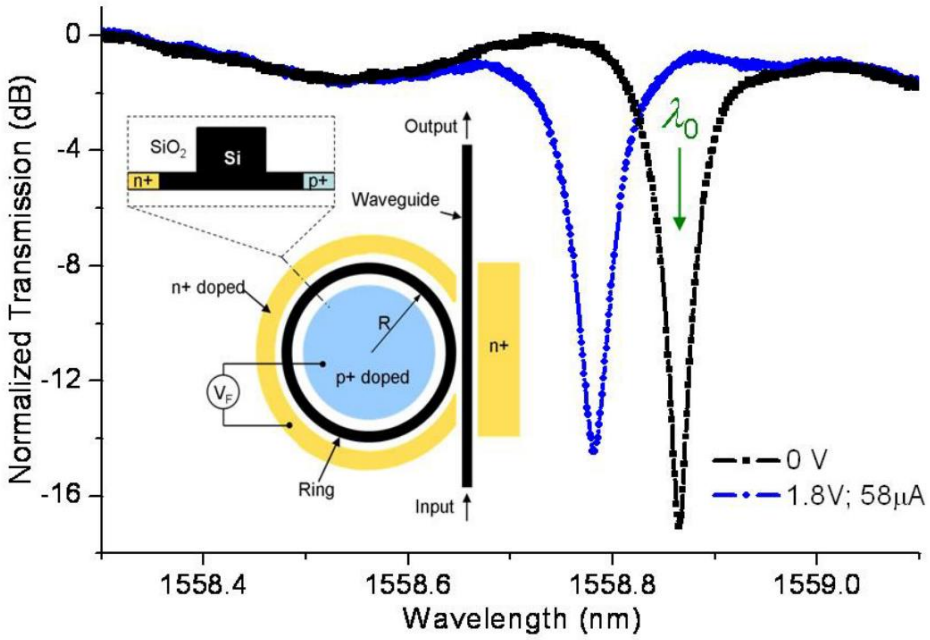

Fig.1.10 The schematic of micro-ring modulator [35].

Typically, Mach-Zehnder interferometer (MZI) based modulators can provide a better performance, such as a high ER and a fast modulating speed with a low switching voltage. However, the footprint of MZI based modulators is usually very large ~1 to 2 mm. Besides, MZI based modulators need a DC bias to set the working point, which increases the power consumption. Compared with MZI based modulators, the footprints of microring modulators and microdisk modulators are much smaller, which is vital for the large volume integration. But the performance of microring and microdisk modulators may not be as high as MZI based modulators.

The improvements of modulators usually rely on improving the passive structure, such as microrings. By various methods, the modulating speed and the modulating depth can be improved with a higher Q factor and a larger ER. In order to obtain a

sharp and deep resonant dip, many new structures have been developed. Fano transmission lineshape is one of the methods. Compared with the general symmetric microring resonant dip, asymmetric Fano transmission lineshape can offer a much sharper curve with a large ER. By building modulators based on passive Fano devices, the efficiency can be much improved.

The original definition of Fano resonance is from the discovery of quantum physics by U. Fano. It is discovered that the existence of alternative pathways for a transition between atomic states can give rise to the interference phenomenon. Based on the interference, an asymmetric line shape, as shown in Fig. 1.11, can be obtained. Compared to conventional symmetric Lorentz line shape, the sharpness is greatly improved.

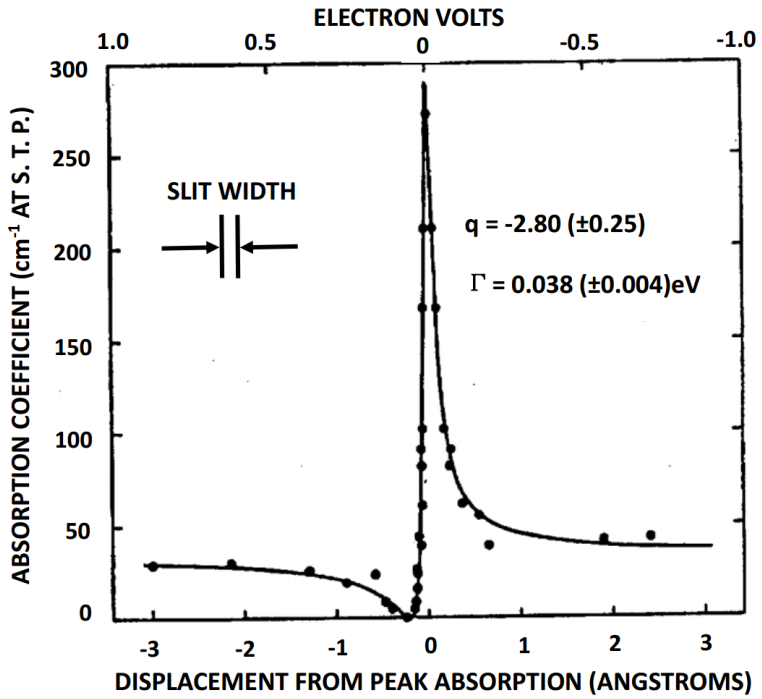

Fig.1.11 A typical Fano lineshape [36].

The definition of Fano lineshape is not limited in quantum physics but expanded into other fields for describing the asymmetric sharp line shape especially. In photonics, Fano resonance is usually generated from the coupling of two resonances. S. Fan proposed a typical numerical model consisted of two partially reflecting elements and a side coupled cavity [37]. As shown in Fig. 1.12, the two partial reflecting elements form a F-P resonator. With the coupling between two resonances, the ring resonator and the F-P resonator, Fano resonance is generated.

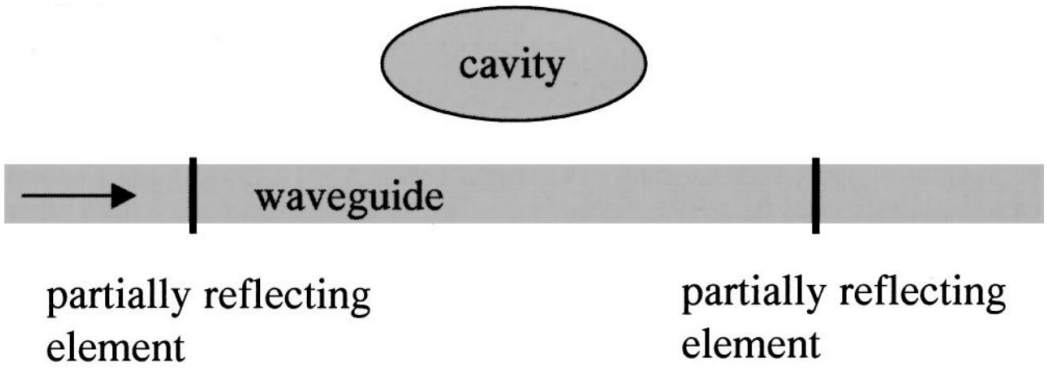

Fig.1.12 The schematic of a typical Fano device [37].

Compared with the scenario without two partially reflecting, the asymmetric Fano line shape can offer much better sharpness and can realize the same ER at much smaller wavelength shift as shown in Fig. 1.13. By using the transfer matrix method [28], the system can be expressed as:

$$T_{out} = T_p * T_{wg} * T_{cavity} * T_{wg} * T_p * T_{in} \quad (1.5)$$

Where T_{out} is the matrix of output light, T_p is the matrix of partially reflecting elements, T_{wg} is the matrix of waveguide, T_{cavity} is the matrix of cavity.

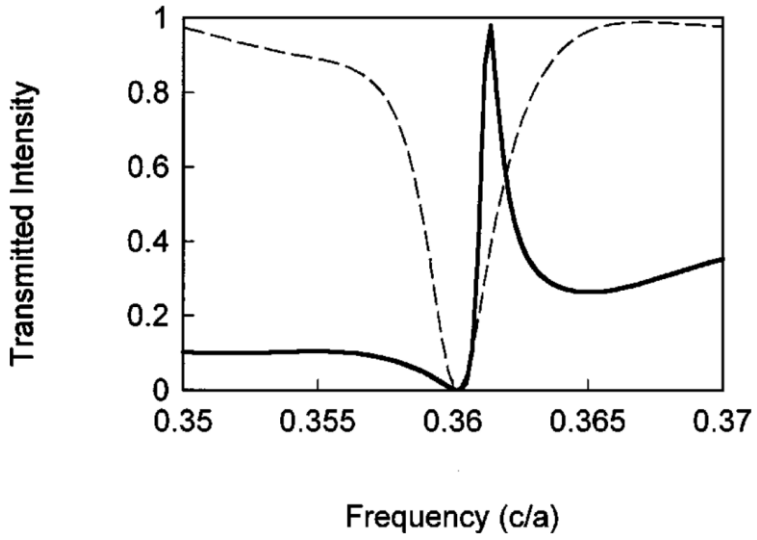

Fig.1.13 The comparison between the transmission spectra of single cavity and Fano system [37].

As S. Fan claimed, 16 times less wavelength shift for the same ER is achieved, which means much lower switching power is needed for building modulators and much more sensitive for building sensors based on Fano system. C. Qiu proposed a Fano device based on interference between a micro-ring and a micro-race-track [38]. As shown in Fig. 1.14, the length of R_o, R_i and L_o are nicely designed to modify the phase difference. When the two light path ways, inner and outer resonators, get interference, the asymmetric Fano line shape is realized.

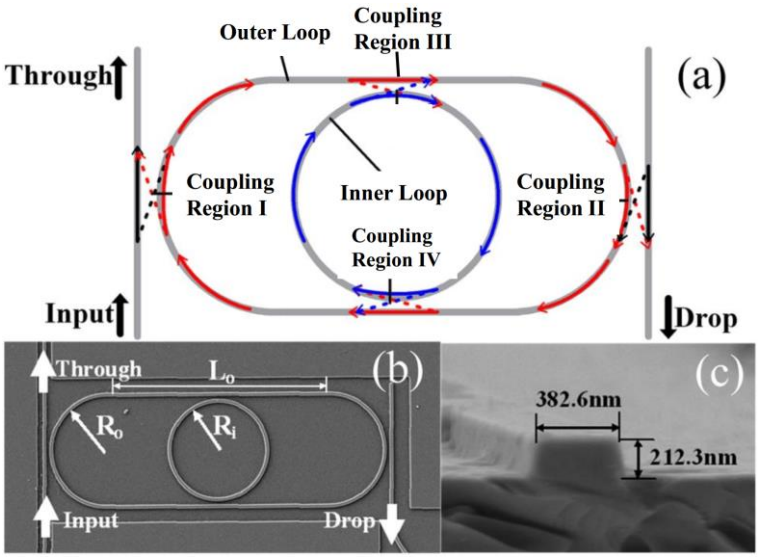

Fig.1.14 The schematic of eye-like micro-ring system [38].

P. Yu utilized nano-beam cavity as a side coupled resonator and photonic crystal holes as reflecting element to build a Fano device. The size of whole device is under 10 μm and can offer 4 times better switch function than only nano-beam cavity exists [39]. F. Wang designed a modulator based on Fano devices. The device is based on Mach-Zehnder optical switch employing dual-bus coupled ring resonator as two-beam interferometer [40]. As shown in Fig. 1.15, the twist cross ring can be equivalent to a general microring, and the phase shifter (PS) works as a modulation region to control the phase. As shown in Fig. 1.16, by introducing phase change by phase shifter (PS), the transmission spectrum will shift. And for the targeted wavelength of 1.59 μm, the state of E_{o2} port will be switched from off to on.

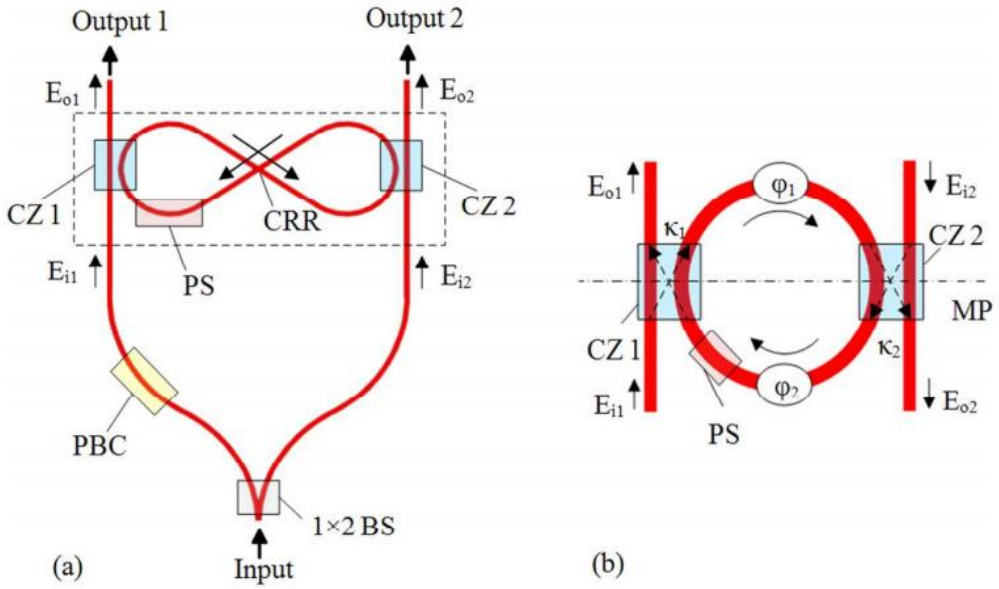

Fig.1.15 The schematic of Mach-Zehnder optical switch employing dual-bus coupled ring resonator as two-beam interferometer [40].

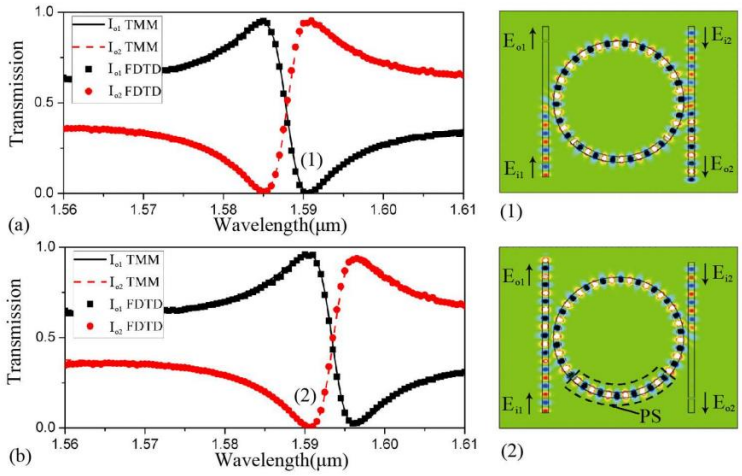

Fig.1.16 The transmission spectrum and the field profiles of on and off state [40].

T. Hu proposed a tunable Fano resonance based on two-beam interference in microring resonator [41]. In this work, the Fano resonance originates from the interference of two beams resonant in the micro-ring resonator. The lineshape of the Fano resonances is tunable through controlling the phase difference of the two

beams.

A.C. Ruege designed a two-mode waveguide coupled with a single mode microring resonator to generate sharp Fano resonance [42]. In this work, two modes are coupled into a single mode microring and get interference, which generates Fano resonance. Q. Huang proposed a microring embedded with Bragg gratings, which works as EIT devices [43]. The resonance of microring and embedded Bragg grating get interference and generates sharp Fano line shape. Q. Huang claimed EIT effect in a two-bus waveguides coupled microdisk resonator [44]. In this work, two modes are coupled in to micro-disk and get interference, which leads to the EIT like lineshape. By tuning the phase, the Fano line shape can be realized. Piao proposed a modulator based on plasmon-induced transparency (PIT) and realize it with plasmonic waveguides [45]. Leonardis designed a Bragg grating microring resonator on SOI platform to generate Fano transmission for sensing applications [46]. J. Zhang also proposed a microring resonator coupled MZI interferometer to generate Fano lineshape and get high sensitive sensors [47]. Mario claimed a two-microring resonator structure that can provide asymmetric Fano resonance and bistability so as to get high ER and low switching power [48]. Wang discovered asymmetric Fano line shape in a single-ring-resonator-based add/drop interferometer [49]. Meanwhile, in order to let the interference occur at the most efficient point, the phase and amplitude difference between resonators is needed to be carefully designed.

Besides, electromagnetically induced transparency (EIT) transmission lineshape is

also very interesting, which can achieve a very large Q factor and generate time delay with low insertion loss as shown in Fig. 1.17. EIT transmission has been utilized many applications, such as slow and fast light [51], modulation [52,53], optical signal processing [54] and sensing [55]. In 2006, Q. Xu first observed experimentally the EIT-like spectrum in an integrated two micro-size silicon microring resonators based system with a quality factor (Q factor) of 17000 [56,57]. In 2011, a EIT-like spectrum with a Q factor of 18000 in a ring-bus-ring geometry synergistically integrated with Mach-Zehnder interferometer is observed by S. Darmawan and Y. Zhang [58,59]. Besides, EIT transmissions can be utilized in MZI modulators as a reference arm. With the time delay and extreme sharp curve, high efficiency modulators can be developed. So building a compact Fano or EIT passive system is one of the main goals to achieve in this work.

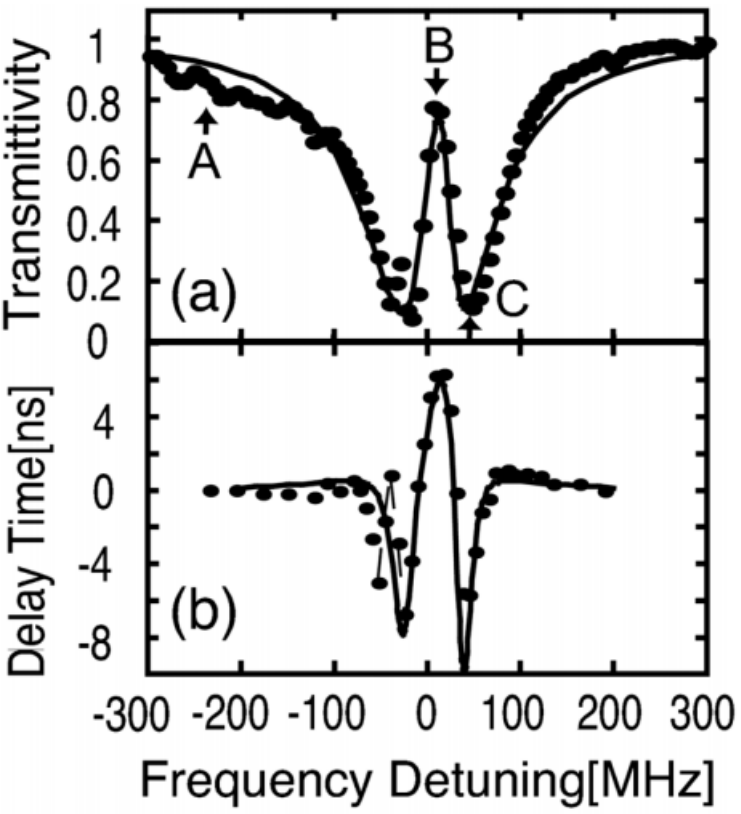

Fig.1.17 The EIT transmission spectrum and the corresponding time delay [50].

1.4 Thesis Outline

This thesis mainly focuses on the design, fabrication and characterization of fundamental components, Fano and EIT resonant devices, sensors and modulators working in NIR and MIR regime on SOI platform. The purpose of this PhD project is to prepare the SOI-based devices for the demand of integrated photonic circuits.

In chapter 2, the simulation environment, the fabrication process and the characterization platform are introduced. A brief introduction of several related simulation tools is to help better understand the device designing process. The

fabrication flow of the modulator is introduced in detail. The 3-dimension optical characterization platform and the characterization processes are introduced.

In chapter 3, fundamental building blocks, such as waveguides, grating couplers, microrings, are designed, fabricated and characterized. The working principles and related reported works are introduced. Compact microring resonator integrated with grating couplers working at 2 μm wavelength is demonstrated in detail.

In chapter 4, in the first part, an EIT-like transmission is generated in an all-pass microring-Bragg gratings (APMR-BG) based coupling resonant system. The working principle and the performance based on five main parameters are demonstrated and discussed in detail. The EIT-like transmission spectrum is experimentally measured and well fitted with the simulation results based on our specially developed numerical model. The time delay is calculated based on the fitting curve with the numerical model, which verifies the existence of the EIT effect. In the second part, tunable and convertible Fano and EIT transmission spectra are introduced. The inner mechanism of the tuning and conversion between Fano and EIT transmission lineshape is demonstrated in detail. The tunable and convertible transmission is experimentally verified. The experimental and simulation results are in a good agreement. In the last part of this chapter, tunable and convertible Fano and EIT resonances are experimentally realized in a MZI-assisted microring-Bragg grating based coupling resonant system. The thermal tuning is calculated and verified to be able to achieve the complete conversion between Fano and EIT transmission lineshapes. With the

tunable and convertibel Fano and EIT transmissions, it is more convenient to choose the optimized method to improve the efficiency of the modulation and sensing in NIR and MIR bands. Besides, although the EIT/Fano devices introduced here only operate at 1.55 μm wavelength, the ideas and concepts can be referred to build the similar device operating at MIR band along with adjusted the dimensional parameters of the devices.

In chapter 5, dual-band optic filters (DBOFs) based on two kinds of partial-reflective-element-embedded microring resonators are introduced. They are the DBOF based on the nanoholes embedded microring resonator and the DBOF based on the Bragg grating embedded microracetrack resonator. In these two systems, the embedded elements form an F-P resonator and get coupled with the microresonator, which gives rise to the dual-band filtering transmission spectra. The dual-band filtering transmission spectra can be utilized to increase the volume of signal processing in NIR band and further extended to be used in MIR band.

In chapter 6, the bio-chemical sensor operating at 2 μm wavelength based on a suspended microracetrack resonator with sub-wavelength-grating (SWG) lateral metamaterial cladding is demonstrated. The fundamental building block, suspended waveguide, is optimized at first. Then the suspended microracetrack resonator is fabricated and characterized. The experimental and simulation results are in a good agreement. Besides, the influences of three main parameters on sensitivity are investigated. And the expected sensitivity is calculated based on the specially

developed numerical model.

In chapter 7, thermal- and electro-optic modulators operating at 2 μm wavelength are demonstrated. The design, fabrication and characterization are introduced in detail. The DC and RF testing results of the thermal-optic microracetrack resonator-based modulator and the electro-optic MZI-based modulator are exhibited respectively. The eye-diagrams are also measured.

In chapter 8, the main results and key contributions of this thesis are summarized. Recommendations for the future work are also proposed.

References

[1] M. J. R. Heck, H. Chen, A. W. Fang, B. R. Koch, D. Liang, H. Park, M. N. Sysak, and J. E. Bowers, "Hybrid Silicon Photonics for Optical Interconnects," *IEEE Journal of Selected Topics in Quantum Electronics*, vol. 17, no. 2, pp. 333-346, Mar. 2011.

[2] G. Roelkens, L. Liu, D. Liang, R. Jones, A. Fang, B. Koch, and J. E. Bowers, "III-V/silicon photonics for on-chip and intra-chip optical interconnects," *Laser & Photon. Rev*, vol. 4, pp. 751–779, 2010.

[3] T. Barwicz, H. Byun, F. Gan, C. W. Holzwarth, M. A. Popovic, P. T. Rakich, M. R. Watts, E. P. Ippen, F. X. Kärtner, H. I. Smith, J. S. Orcutt, R. J. Ram, V. Stojanovic, O. O. Olubuyide, J. L. Hoyt, S. Spector, M. Geis, M. Grein, and T.

Lyszczarz, and J. U. Yoon, "Silicon photonics for compact, energy-efficient interconnects [Invited]," *J. Opt. Netw.*, vol. 6, pp. 63-73, 2007.

[4] A. V. Krishnamoorthy, R. Ho, X. Zheng, H. Schwetman, J. Lexau, P. Koka, G. Li, Ivan Shubin, and J. E. Cunningham, "Computer Systems Based on Silicon Photonic Interconnects," *Proceedings of the IEEE*, vol. 97, no. 7, pp. 1337-1361, Jul. 2009.

[5] Q. Xu, B. Schmidt, S. Pradhan, and M. Lipson, "Micrometre-scale silicon electro-optic modulator," *Nature*, vol. 435, pp. 325-327, May, 2005.

[6] G. T. Reed and C. E. J. Png, "Silicon optical modulators," *Materialstoday*, vol. 8, no. 1, pp. 40-50, Jan. 2005.

[7] F. Y. Gardes, D. J. Thomson, N. G. Emerson, and G. T. Reed, "40 Gb/s silicon photonics modulator for TE and TM polarisations," *Opt. Express*, vol. 19, pp. 11804-11814, 2011.

[8] W. M. J. Green, M. J. Rooks, L. Sekaric, and Y. A. Vlasov, "Ultra-compact, low RF power, 10 Gb/s silicon Mach-Zehnder modulator," *Opt. Express*, vol. 15, pp. 17106-17113, 2007.

[9] A. Liu, L. Liao, D. Rubin, H. Nguyen, B. Ciftcioglu, Y. Chetrit, N. Izhaky, and M. Paniccia, "High-speed optical modulation based on carrier depletion in a silicon waveguide," *Opt. Express*, vol. 15, pp. 660-668 (2007)

[10] C. Batten, A. Joshi, J. Orcutt, A. Khilo, B. Moss, C. W. Holzwarth, M. A. Popovi, H. Li, H. I. Smith, J. L. Hoyt, F. X. Kartner, R. J. Ram, V. Stojanovic, and K.

Asanovic, "Building Many-Core Processor-to-DRAM Networks with Monolithic CMOS Silicon Photonics," *IEEE Micro*, vol. 29, no. 4, pp. 8-21, Jul. 2009

[11] A. Densmore, D.-X. Xu, P. Waldron, S. Janz, P. Cheben, J. Lapointe, A. Delâge, B. Lamontagne, J. H. Schmid, and E. Post, "A Silicon-on-Insulator Photonic Wire Based Evanescent Field Sensor," *IEEE Photonics Technology Letters*, vol. 18, no. 23, pp. 2520-2522, Dec.1, 2006.

[12] G. Roelkens, A. Abassi, P. Cardile, U. Dave, A. de Groote, Y. de Koninck, S. Dhoore, X. Fu, A. Gassenq, N. Hattasan, Q. Huang, S. Kumari, S. Keyvaninia, B. Kuyken, L. Li, P. Mechet, M. Muneeb, D. Sanchez, H. Shao, T. Spuesens, A. Z. Subramanian, S. Uvin, M. Tassaert, K. van Gasse, J. Verbist, R. Wang, Z. Wang, J. Zhang, J. van Campenhout, X. Yin, J. Bauwelinck, G. Morthier, R. Baets and D. van Thourhout, "III-V-on-Silicon Photonic Devices for Optical Communication and Sensing," *Photonics*, vol. 2, no. 3, pp. 969-1004, 2015.

[13] M. Iqbal, M. A. Gleeson, B. Spaugh, F. Tybor, W. G. Gunn, M. Hochberg, T. Baehr-Jones, R. C. Bailey, and L. Cary Gunn, "Label-Free Biosensor Arrays Based on Silicon Ring Resonators and High-Speed Optical Scanning Instrumentation," *IEEE Journal of Selected Topics in Quantum Electronics*, vol. 16, no. 3, pp. 654-661, May, 2010.

[14] Y. Chen, H. Lin, J. Hu, and M. Li, "Heterogeneously Integrated Silicon Photonics for the Mid-Infrared and Spectroscopic Sensing," *ACS Nano*, vol. 8, no. 7, pp. 6955-6961, 2014.

[15] P. Dong, X. Liu, S. Chandrasekhar, L. L. Buhl, R. Aroca and Y. K. Chen, "Monolithic Silicon Photonic Integrated Circuits for Compact 100 Gb/s Coherent Optical Receivers and Transmitters," *IEEE Journal of Selected Topics in Quantum Electronics*, vol. 20, no. 4, pp. 150-157, Jul. 2014.

[16] B. G. Lee, A. V. Rylyakov, W. M. J. Green, S. Assefa, C. W. Baks, R. Rimolo-Donadio, D. M. Kuchta, M. H. Khater, T. Barwicz, C. Reinholm, E. Kiewra, S. M. Shank, C. L. Schow, and Y. A. Vlasov, "Monolithic Silicon Integration of Scaled Photonic Switch Fabrics, CMOS Logic, and Device Driver Circuits," *Journal of Lightwave Technology*, vol. 32, no. 4, pp. 743-751, Feb.15, 2014.

[17] C. R. Doerr, L. Chen, D. Vermeulen, T. Nielsen, S. Azemati, S. Stulz, G. McBrien, X. Xu, B. Mikkelsen, M. Givehchi, C. Rasmussen, and S. Y. Park, "Single-Chip Silicon Photonics 100-Gb/s Coherent Transceiver," *Optical Fiber Communication Conference, (Optical Society of America, 2014)*, paper Th5C.1.

[18] G. Z. Mashanovicha, S. Stankovicb, P. Y. Yanga, E. J. Teoc, F. Dell'Oliod, V. M. N. Passarod, A. A. Bettiolc, M. B. H. Breesec, G. T. Reeda, "Silicon waveguides for the mid-infrared wavelength region," *Proc. of SPIE.*, vol. 6898, no. 68980T, pp. 1-7, 2008.

[19] R. W. Waynant, I. K. Ilev and I. Gannot, "Mid-infrared laser applications in medicine and biology," *Phil. Trans. R. Soc. Lond. A* , vol. 359, pp. 635–644, 2001.

[20] F. K. Tittel, D. Richter, and A. Fried, "Mid-infrared laser applications in

spectroscopy," *Solid-State Mid-Infrared Laser Sources, Topics Appl. Phys.*, vol. 89, pp. 445–510, 2003.

[21] Anthony Krier, *Mid-infrared Semiconductor Optoelectronics*, Springer, vol. 118 (2006).

[22] Shankar, Raji, *Mid-Infrared Photonics in Silicon Shankar*, Harvard University (2013).

[23] Tydex, *Silicon Datasheet*, TYDEX Company (1994).

[24] R. Soref, "Mid-Infrared Photonics," *Opt. Fiber Comm. Conf.*, Mar. 2015.

[25] D. J. Richardson, "Filling the Light Pipe," *Science*, vol. 330, no. 6002, pp. 327-328, Oct. 2010.

[26] M. Nedeljkovic, R. Soref, and G. Z. Mashanovich, "Free-Carrier Electrorefraction and Electroabsorption Modulation Predictions for Silicon Over the 1–14-m Infrared Wavelength Range," *IEEE Photonics Journal*, vol. 3, no. 6, Dec. 2013.

[27] G. T. Reed, A. P. Knights, *Silicon Photonics-An Introduction*, Wiley (2004).

[28] L. Chrostowski, V. M. Hochberg, *Silicon Photonics Design From Devices to Systems*, Cambridge University Press (2015).

[29] Z. Cheng, X. Chen, C. Y. Wong, K. Xu, C. K. Y. Fung, Y. M. Chen, and H. K. Tsang, "Mid-Infrared Grating Couplers for Silicon-on-Sapphire Waveguides," *IEEE Photon. J.*, vol. 4, no. 1, pp. 104-113, 2012.

[30] C. Li, H. Zhang, M. Yu, and G. Q. Lo, "CMOS-compatible high efficiency

double-etched apodized waveguide grating coupler," *Opt. Express*, vol. 21, no. 7, pp. 7868-7874, 2013.

[31] W. Bogaerts, P. D. Heyn, T. V. Vaerenbergh, K. D. Vos, S. K. Selvaraja, T. Claes, P. Dumon, P. Bienstman, D. V. Thourhout, and R. Baets, "Silicon microring resonators," *Laser & Photonics Reviews*, vol. 6, no. 1, pp. 47-73, Jan. 2012.

[32] M. Soltani, S. Yegnanarayanan, and A. Adibi, "Ultra-high Q planar silicon microdisk resonators for chip-scale silicon photonics," *Opt. Express*, vol. 15, issue 18, pp. 4694-4704. 2007

[33] Z. Zhou, H. Yi, "Silicon microring sensors," *Proc. SPIE 8236, Laser Resonators, Microresonators, and Beam Control XIV*, pp. 823617, Feb. 2012.

[34] B. J. Frey, D. B. Leviton, T. J. Madison, "Temperature-dependent refractive index of silicon and germanium," *Proc. of SPIE 6273*, 2006.

[35] Q. Xu, *Controlling the flow of light on chip with microring-resonator-based silicon photonic devices*," Cornell University (2007).

[36] U. Fano, "Effects of Configuration Interaction on Intensities and Phase Shifts," *Physical review letters,* vol. 124, issue. 6, pp. Dec. 1961.

[37] S. Fan, "Sharp asymmetric line shapes in side-coupled waveguide-cavity systems," *Applied physics letter*, vol. 80, no. 908, 2002.

[38] C. Qiu, P. Yu, T. Hu, F. Wang, X. Jiang and J. Yang, "Asymmetric Fano resonance in eye-like microring system," *Applied physics letter*, vol. 101, no. 021110, 2012.

[39] P. Yu, T. Hu, H. Qiu, F. Ge, H. Yu, X. Jiang and J. Yang, "Fano resonances in

ultracompact waveguide Fabry-Perot resonator side-coupled lossy nanobeam cavities," *Applied physics letter*, vol. 103, no. 091104, 2013.

[40] F. Wang, X. Wang, H. Zhou, Q. Zhou, Y. Hao, X. Jiang, M. Wang, J. Yang, "Fano-resonance-based Mach-Zehnder optical switch employing dual-bus coupled ring resonator as two-beam interferometer," *Optical Express*, vol. 17, no. 9, pp. 7708–7716, 2009.

[41] T. Hu, P. Yu, C. Qiu, H. Qiu, F. Wang, M. Yang, X. Jiang, H. Yu and J. Yang, "Tunable Fano resonance based on two-beam interference in micro-ring resonator," *Applied physics letter*, vol. 102, no. 011112, 2013.

[42] A. C. Ruege，R. M. Reano, "Sharp Fano Resonances From a Two-Mode Waveguide Coupled to a Single-Mode Ring Resonator," *Journal of Lightwave Technology*, vol. 28, issue. 20, pp. 2964-2968, Sep. 2009.

[43] Q. Huang, K. Ma, S. He, "Experimental Demonstration of Single ModeSplitting in Microring With Bragg Gratings," *Photonics Technology Letters*, vol. 27, issue. 13, pp. 1402-1405, Apr. 2015.

[44] Q. Huang, Z. Shu, G. Song, J. Chen, J. Xia, and J. Yu, "Electromagnetically induced transparency-like effect in a two-bus waveguides coupled microdisk resonator," *Optical Express*, vol. 22, issue. 3, pp. 3219–3227, 2014.

[45] X. Piao, S. Yu, and N. Park, "Control of Fano asymmetry in plasmon inducedtransparency and its application to plasmonic waveguide modulator," *Optical Express*, vol. 20, issue 17, pp. 18994-18999, 2012.

[46] F. De Leonardis, C. E. Campanella, B. Troia, A. G. Perri and V. M. N. Passaro, "Performance of SOI Bragg Grating Ring Resonator for Nonlinear Sensing Applications," *Sensors*, vol. 14, no. 9, pp. 16017–16034, 2014.

[47] J. Zhang, Z. Liu, Y. Zhang, "Ring resonator coupled Mach-Zehnder interferometer for sensing application," *Proc. SPIE*, vol. 9233, 2014.

[48] L. Y. Mario, S. Darmawan, and M. K. Chin, "Asymmetric Fano resonance and bistability for high extinction ratio, large modulation depth, and low power switching," *Optical Express*, vol. 14, no. 26, pp. 12770-12781, 2006.

[49] K. Wang, X. Liu, C. Yu, and Y. Zhang, "Tunable Fano resonance in a single-ring-resonator-based add/drop interferometer," *Applied Optics*, vol. 52, issue. 20, pp. 4884–4889, 2013.

[50] K. Totsuka, N. Kobayashi, and M. Tomita, "Slow Light in Coupled-Resonator-Induced Transparency," *Phys. Rev. Lett.*, vol. 98, no. 21, pp. 213904, May, 2007.

[51] Novikova, R. L. Walsworth, and Y. Xiao, "Electromagnetically induced transparency-based slow and stored light in warm atoms," *Laser Photon. Rev.*, vol. 6, no. 3, pp. 333–353, 2012.

[52] S. Emelett and R. Soref, "Synthesis of dual-microring-resonator cross-connect filters," *Opt. Express*, vol. 13, no. 12, pp. 4439-4456, 2005.

[53] Q. Li, Z. Zhang, F. Liu, M. Qiu, and Y. Su, "Dense wavelength conversion and multicasting in a resonance-split silicon microring," *Appl. Phys. Lett.*, vol. 93, no. 8, pp. 081113, 2008.

[54] R. G. Beausoleil, W. J. Munro, D. A. Rodrigues, and T. P. Spiller, “Applications of electromagnetically induced transparency to quantum information processing,” *J. Mod. Opt.*, vol. 51, no. 16–18, pp. 2441–2448, 2004.

[55] Y. F. Xiao, V. Gaddam, and L. Yang, “Coupled optical microcavities: an enhanced refractometric sensing configuration,” *Opt. Express*, vol. 16, no. 17, pp. 12538, 2008.

[56] Q. Xu, S. Sandhu, M. L. Povinelli, J. Shakya, S. Fan, and M. Lipson, “Experimental Realization of an On-Chip All-Optical Analogue to Electromagnetically Induced Transparency,” *Phys. Rev. Lett.*, vol. 96, no. 12, pp. 123901, 2006.

[57] Q. Xu, P. Dong, and M. Lipson, “Breaking the delay-bandwidth limit in a photonic structure,” *Nat. Phys.*, vol. 3, no. 6, pp. 406–410, 2007.

[58] Y. Zhang, S. Darmawan, L. Y. M. Tobing, T. Mei, and D. H. Zhang, “Coupled resonator-induced transparency in ring-bus-ring Mach–Zehnder interferometer,” J. *Opt. Soc. Am. B*, vol. 28, no. 1, pp. 28-36, 2011.

[59] S. Darmawan, L. Y. M. Tobing, and D. H. Zhang, “Experimental demonstration of coupled-resonator-induced transparency in silicon-on-insulator based ring-bus-ring geometry,” *Opt. Express*, vol. 19, no. 18, pp. 17813–17819, 2011.

Chapter 2
Design, Fabrication and Characterization of Silicon Photonic Devices

2.1 Device Design and Simulation Method

2.1.1 FDTD Simulation

Finite-difference time-domain (FDTD) method is a widely used numerical analysis simulation method for calculating the approximate solutions of an electrodynamic system. This technique is particularly useful for analyzing the interaction of light with complicated structures employing sub-wavelength-scale features. FDTD is an "exact" numerical calculation of Maxwell's equations, where the accuracy converges to the exact solution as the spatial discretization of the volume is reduced [1-5]. Besides, FDTD simulation is based on time-domain, hence the calculation for a large frequency range can be conducted in a single simulation run. In a typical simulation, the materials, the structures and the simulation boundaries are defined first. Then a pulse of light with a broad spectrum of wavelength components is generated from the source. With the help of the monitors, the information of light field can be obtained. The detailed modeling process is as follows:

(1) The types of materials and the respective parameters are defined. Lumerical FDTD solution offers a database of typical materials, such as silicon, SiO_2, air, and H_2O. In this database, the dispersion of refractive

index has been taken into account.

(2) The structures are drawn or generated with scripts, including thickness, width, radius and other geometries of different devices. Besides, the light sources and monitors are added. As shown in Fig. 2.1, an add-drop microring resonator is drawn. One input light source, four port-monitors and one lateral mode field monitor are added.

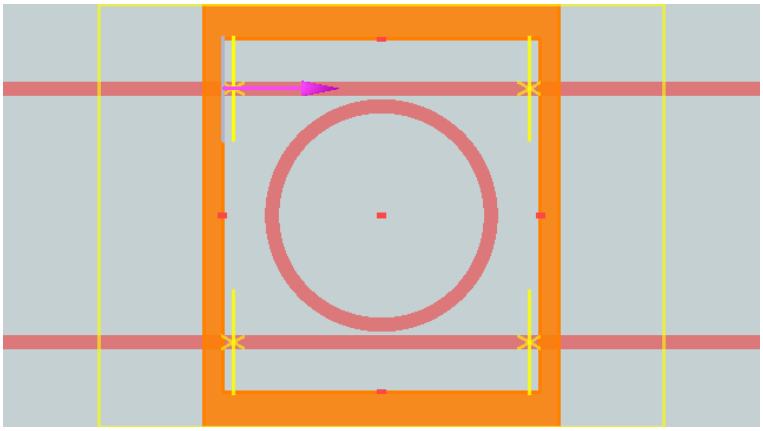

Fig.2.1 The top view of a simulated add-drop microring resonator.

(3) The simulation boundaries are defined. At first, 2D or 3D simulation needs to be decided and the type of boundaries needs to be set. The mesh order is chosen according to the accuracy requirement. 3D simulation and higher mesh order can offer better accuracy but also consume much more time. As shown in Fig. 2.2, the orange frame is the boundary of 3D simulation volume. Only the light field in this frame will be simulated. Usually all the simulation boundaries are set as perfectly matched layer (PML), which means the outgoing waves will be completely absorbed and no reflection occurs.

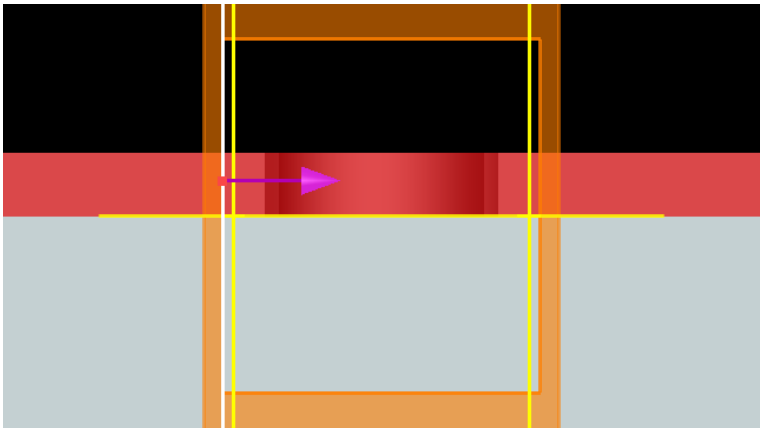

Fig.2.2 The side view of a simulated add-drop microring resonator.

(4) A pulse of light with a broad spectrum of wavelength components is generated from the source. Then after the transmission through all simulated structures, at the output port, the monitors can capture all the information of light field. A typical transmission spectrum of an add-drop microring resonator is shown in Fig. 2.3, where y-axis is transmission and x-axis is wavelength.

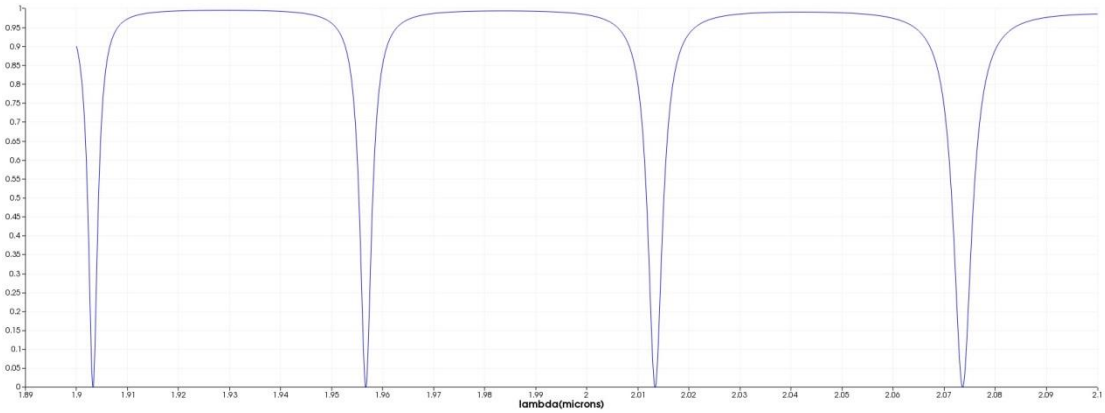

Fig.2.3 A typical transmission spectrum of an add-drop microring resonator.

2.1.2 Matlab Numerical Model and Rsoft Software

In this project, most of the complex structures are calculated based on transfer matrix method (TMM). TMM is a technique used in optics and acoustics to analyze the propagation of electromagnetic or acoustic waves through a stratified medium [6]. Furthermore, it is also a convenient and efficient technique for calculating the transmission of a light path through series of structure with various profiles. TMM is based on Maxwell's equations. While the continuity conditions of the electromagnetic field at the boundaries and the input light at the beginning of one section of structures are given, the output light at the end of this section can be calculated with a matrix equation. The matrix is extracted from the feature of this section. By repeating this step, a cascade of different sections can then be represented by the product of these extracted matrices. Next, the light field at the output port of the whole system can be calculated by multiplying the matrix of the input light and the product of extracted matrices.

For example, an all-pass microring resonator can be written as shown in equation (2.1):

$$T_{in} = T_{wg} \cdot T_{ring} \cdot T_{wg} \cdot T_{out} \tag{2.1}$$

where $T_{ring} = \begin{pmatrix} 1/t_{ring\_thru} & 0 \\ 0 & t_{ring\_thru\_inv} \end{pmatrix}$ is the matrix of microring resonator, in which $t_{ring\_thru} = \frac{-\alpha + te^{-i\varphi}}{-\alpha t^* + e^{-i\varphi}}$ and $t_{ring\_thru\_inv} = \frac{-\alpha + t^* e^{i\varphi}}{-\alpha t + e^{i\varphi}}$; $\varphi = \frac{2\pi n_{eff} L_r}{\lambda}$ is the round-trip phase; $t = \sqrt{1 - |k|^2}$ is the transmission coefficient and k is the coupling coefficient; t^* is the

conjugation of t; $\alpha^2 = e^{-\delta_r L_r}$ is the round-trip-power-attenuation in which the δ_r is the propagation loss of microring waveguide per unit length; $L_r = 2\pi R$ is the cavity length of the microring in which the R is the radius; λ is the wavelength; n_{eff} is the effective refractive index of the microring waveguide; $T_{wg} = \begin{pmatrix} e^{-i\beta\frac{L}{2}} & 0 \\ 0 & e^{i\beta\frac{L}{2}} \end{pmatrix}$ is the matrix of bus waveguide, in which $\beta = \frac{2\pi n_{eff}}{\lambda} - i\frac{\delta}{2}$; δ is the propagation loss of the waveguide per unit length; L is the length.

According to equation 2.1, the parameter n_{eff} is very crucial, which is extracted based on the dimension of waveguide and the cladding layer. In this project, we utilize the BeamPROP module of Rsoft software to calculate the effective indices, which takes the dispersion into account. And then substitute n_{eff} to the equation 2.1 coded by Matlab, the transmission spectrum can be calculated. The simulation procedure based on Matlab numerical model and Rsoft software is as follows:

(1) As shown in Fig. 2.4, a straight waveguide is drawn with BeamPROP module of Rsoft software. The height and the width of the waveguide are defined. The refractive indices of cladding layer and substrate layer are defined. By sweeping the wavelength of the input light, the effective refractive indices under different wavelengths can be obtained.

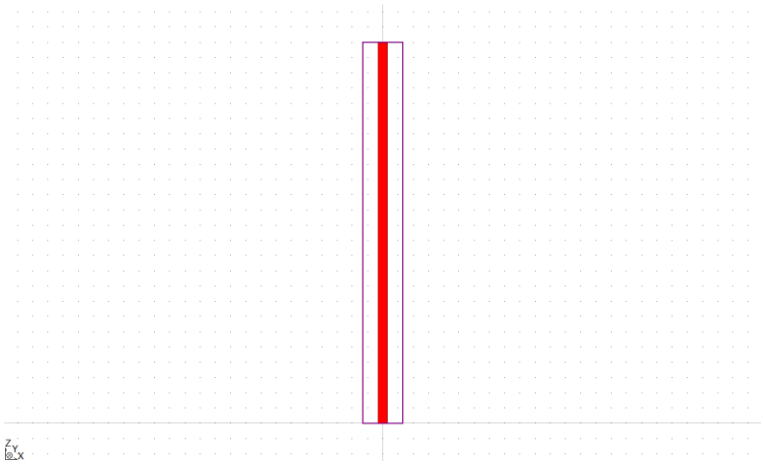

Fig.2.4 The simulation with BeamPROP module of Rsoft software.

(2) As shown in Fig. 2.5, by fitting the calculated effective indices, a function of effective indices versus wavelength can be obtained.

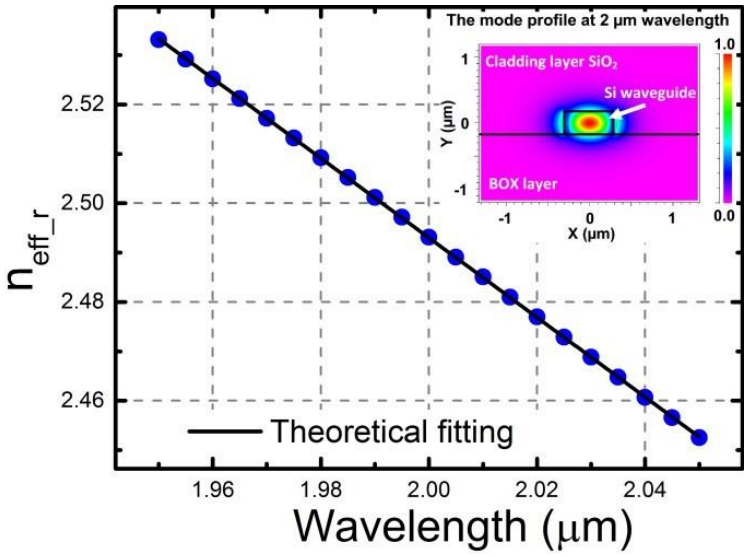

Fig.2.5 The fitting of the calculated effective indices.

(3) By substituting the function of effective index into the TMM numerical model coded with Matlab, the transmission spectrum can be calculated. As shown in Fig. 2.6, a typical transmission spectrum of an all-pass microring resonator can be obtained.

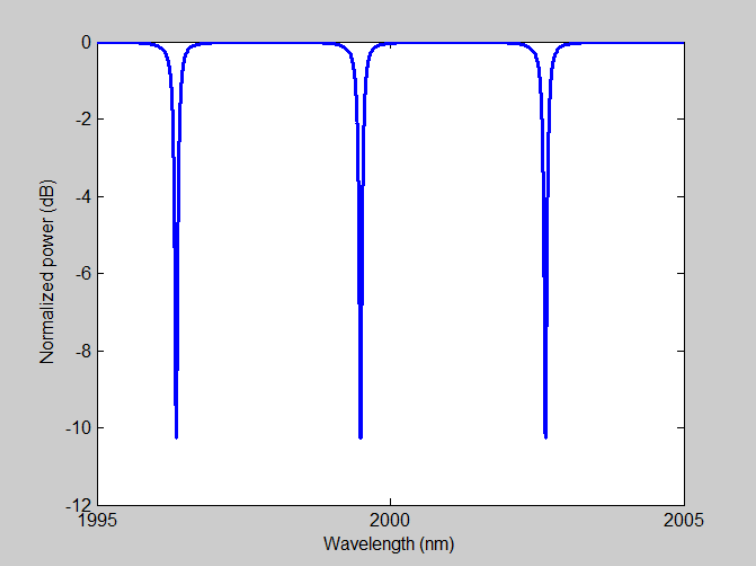

Fig.2.6 A typical transmission spectrum of an all-pass microring resonator based on TMM.

Compared with the simulation based on Matlab numerical model and Rsoft software, the advantages of FDTD simulation includes: 1. the 3-D FDTD simulation is the simulation method that is the most closest to the experimental results in NIR communication band; 2. Lumerical FDTD software is much easier than coding with Matlab as the structures can be designed and defined directly with the simple tools; 3. loop systems and feedback systems can be simulated more conveniently. The disadvantages of FDTD simulation includes: 1. the time consumption of FDTD simulation is much higher than the numerical model method especially when simulating large size systems and resonant structures; 2. convergence problems sometime occur, which needs careful definition of the boundary properties; 3. the simulation results may have a slight error comparing with the experimental results in MIR band due to the lack of complete refractive index data for MIR band.

2.2 Fabrication of Devices

2.2.1 Fabrication Process Flow

Fig. 2.7 shows the SOI wafer used for fabricating devices operating at 2 μm in this project, of which the top-Si layer is 340 nm and the buried oxide (BOX) layer is 2 μm. For the fabrication of conventional devices working at 1.55 μm wavelength, the thickness of the top-Si layer is usually 220 nm. Since the wavelength increases to 2 μm, the size of waveguides needs to be larger to offer a better confinement of light.

Fig.2.7 The SOI wafer with a 340 nm top-Si layer and a 2 μm BOX layer [8].

As shown in Fig. 2.8, from top to bottom, the fabrication process of modulators consists of 23 steps, including grating lithography, grating etching, low dose P+ lithography, low dose P+ doping, hard mask deposition, waveguide lithography, hard mask etching, rib etching, complete etching lithography, Si complete etching, thermal oxidation, lose dose N+ lithography, low dose N+ doping, high dose P++ lithography, high dose P++ doping , high dose N++ lithography, high dose N++ doping, cladding deposition, via lithography, via etching, metal deposition, electrode lithography, electrode etching. Fig. 2.9 shows the process flow. The fabrication of passive device is similar with the fabrication process of modulator but without the doping steps and the

electrodes fabrication steps.

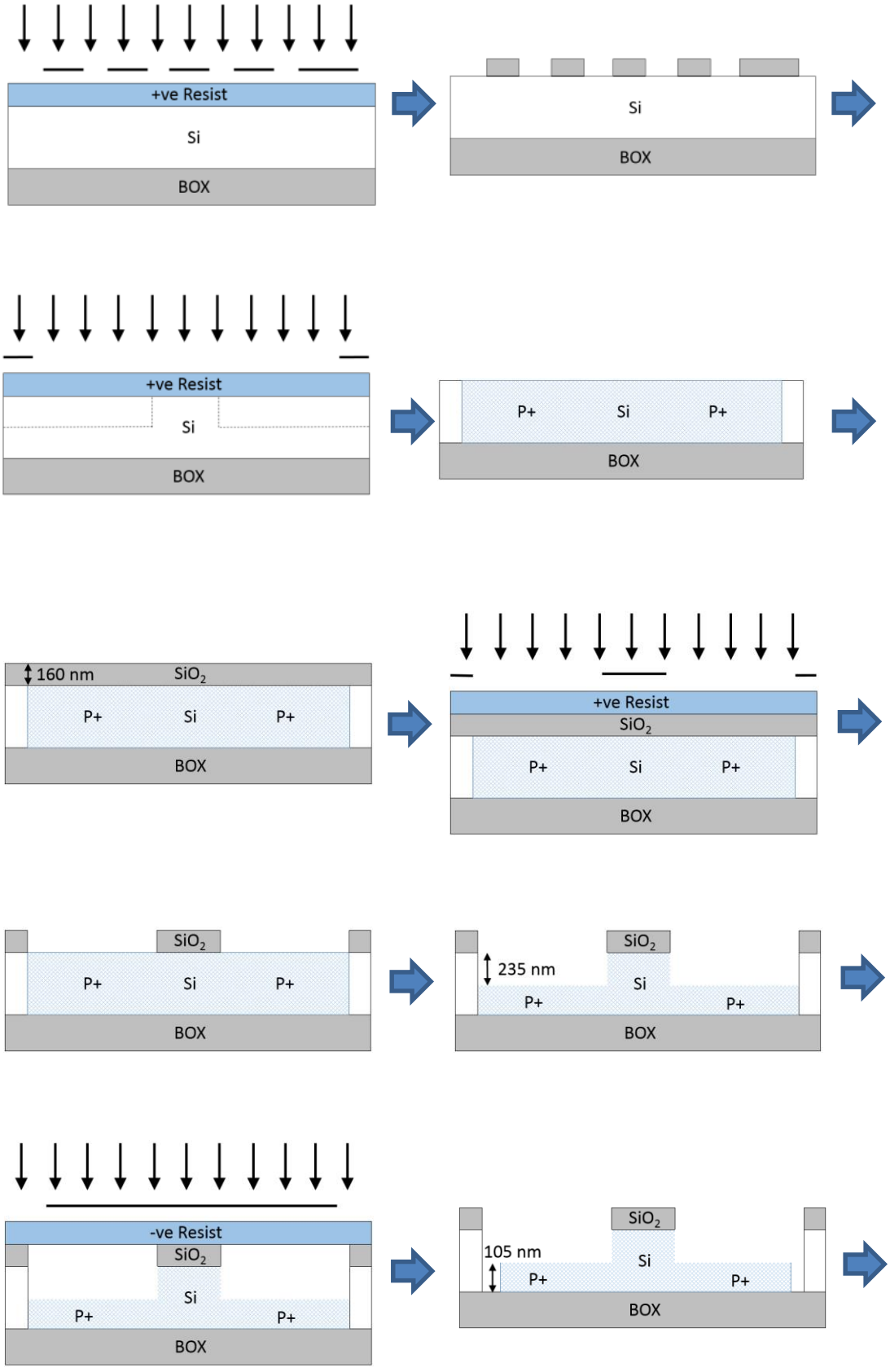

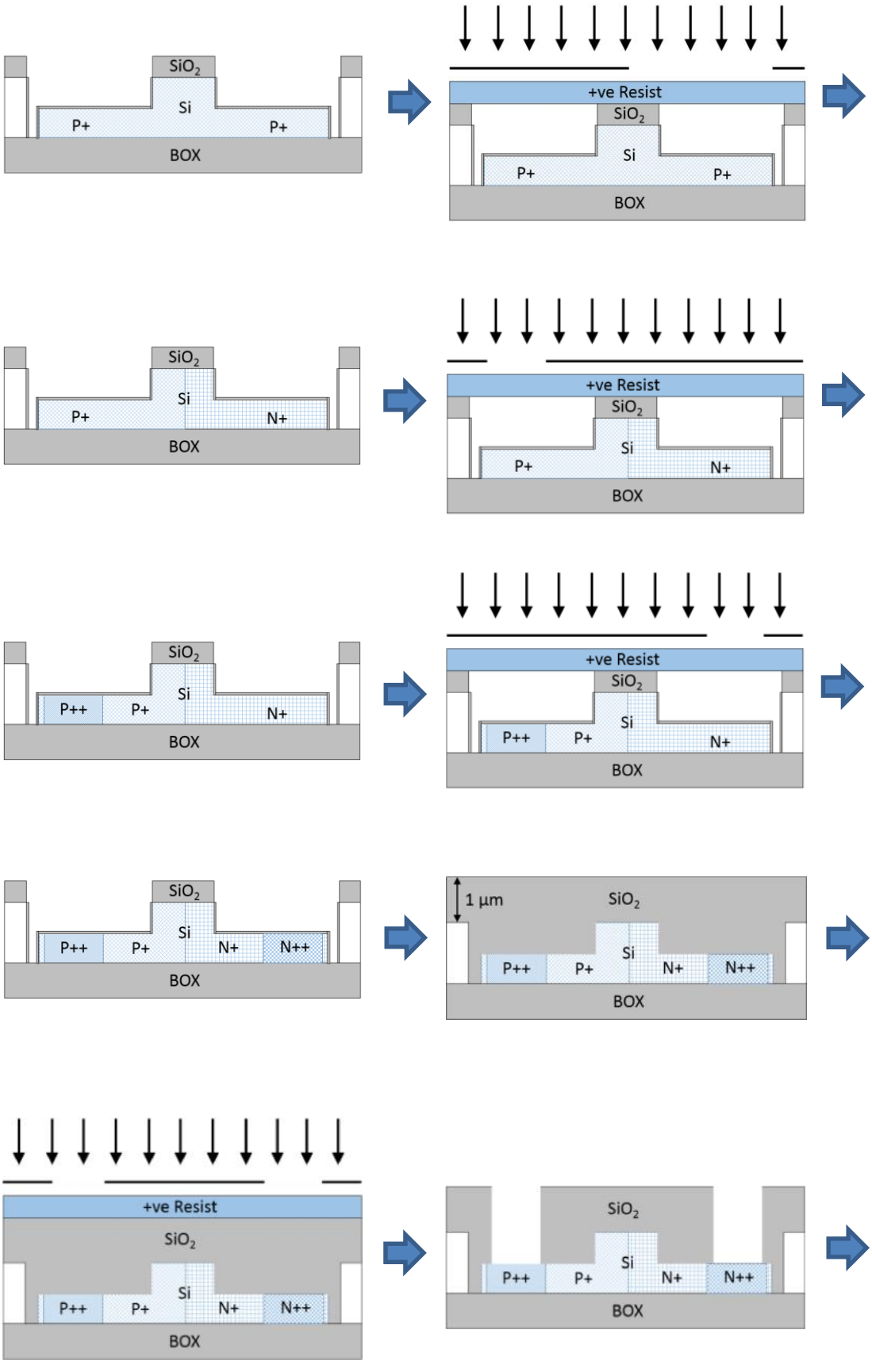
SiO2
Si
P+
P+
BOX
+ve Resist
SiO2
Si
P+
P+
BOX
SiO2
Si
P+
N+
BOX
+ve Resist
SiO2
Si
P+
N+
BOX
SiO2
Si
P++
P+
N+
BOX
+ve Resist
SiO2
Si
P++
P+
N+
BOX
SiO2
Si
P++
P+
N+
N++
BOX
1 µm
SiO2
Si
P++
P+
N+
N++
BOX
+ve Resist
SiO2
Si
P++
P+
N+
N++
BOX
SiO2
Si
P++
P+
N+
N++
BOX

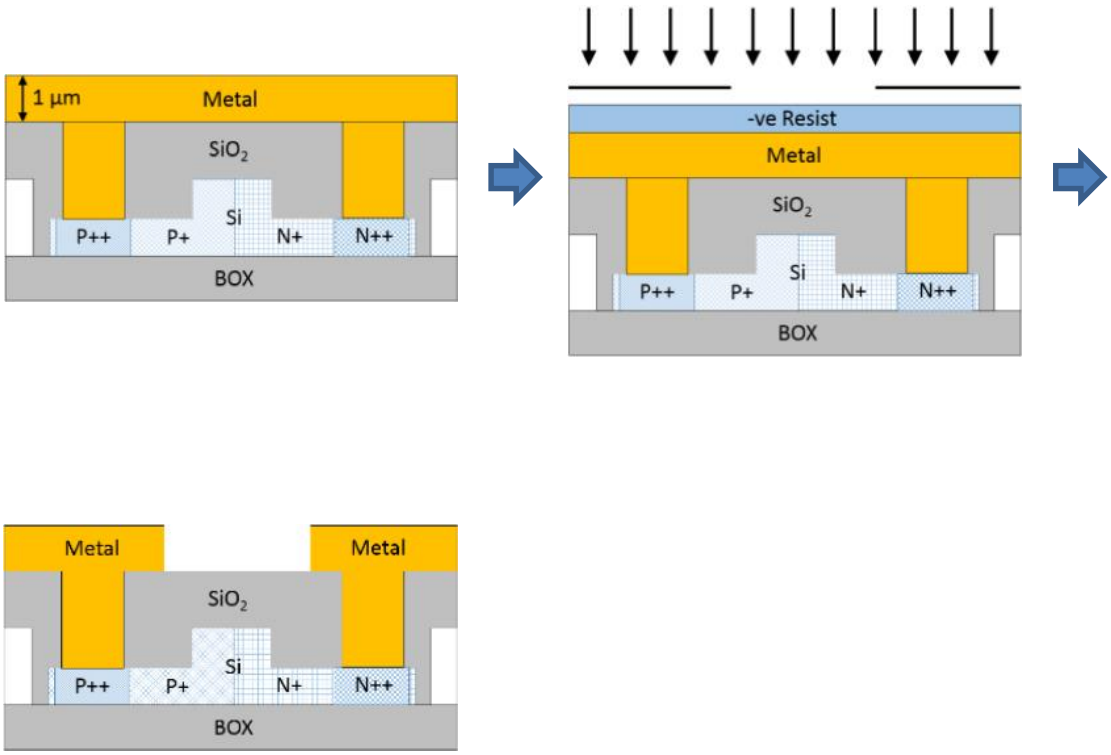

Fig.2.8 Fabrication process of a conventional modulator.

The upper cladding layer does not have to be SiO2 and it can be replaced by other similar isolation material. The light P+ doping is also called background doping concentration. The purpose of light doping is to form a P-N junction in the waveguide region. By injecting carriers into or depleting carriers from the waveguide, according to the free plasma effect, the refractive index of the waveguide will be changed, as well as the phase or the amplitude of the output light. Then the modulation of light can be achieved. Besides, the light doping can also improve the conductivity of slab region between electrode metal contact and waveguide, which can increase the modulating efficiency. The goal of high dose doping is to form ohmic contact region and reduce the resistance between silicon and electrodes.

2.2.2 Optical Lithography and Electron Beam Lithography

For the alignment of electron beam lithography (EBL), “etching markers” are adopted. The shape of the alignment markers is a square of $20\ \mu m * 20\ \mu m$. Using EBL to write those large markers would be very time consuming and the cost is high. So in order to save time, optical lithography is utilized. The wafers are diced into small pieces of 1.5 cm * 2 cm at first. Details of the optical lithography processes are as follows:

(1) Clean wafer and spin-coat AZ5214 photoresist at 4000 rpm. Set the spin-coating time at 30 s. Normally, the thickness of AZ5214 would be around 1.4 μm.

(2) After spin-coating, soft baked the sample at 105 ℃ for 2 mins.

(3) Then align the mask and wafer. Set exposure time for the first exposure.

(4) After first exposure, hard bake the sample at 120 ℃ for 2 mins to harden the photoresist.

(5) Set the exposure time of flood exposure and expose the sample.

(6) At last, develop the sample with CD-26 developer. The photoresist of the area covered by mask will be removed and waiting for etching.

For nearly all structures working at 2 μm wavelength, the size is sub-micro and our optical lithography cannot achieve such small feature size. So after the alignment markers are prepared, the subsequent patterns are all written with EBL lithography.

For our EBL system, positive photoresist ZEP-520A is used. The detailed EBL patterning process is as below:

(1) Clean the wafer.

(2) Spin-coat ZEP-520A at 6000 rpm for 90 s and the thickness is ~300 nm.

(3) Then bake the sample at 180 ℃ for 3 mins.

(4) Transfer the pattern to photoresist with EBL. (For different platform and different thickness of ZEP-520A, the dose needs to be checked at first. For our SOI platform, when the thickness of ZEP-520A is ~300 nm, the dose is about 250 μC/cm^2.)

(5) Develop the sample with ZED-N50 for 60 s. The exposed ZEP-520A will be removed and waiting for etching.

As shown in Fig. 2.9, the profile patterned by EBL is much sharper than optical lithography. Besides, very small feature size (< 50 nm) can be achieved.

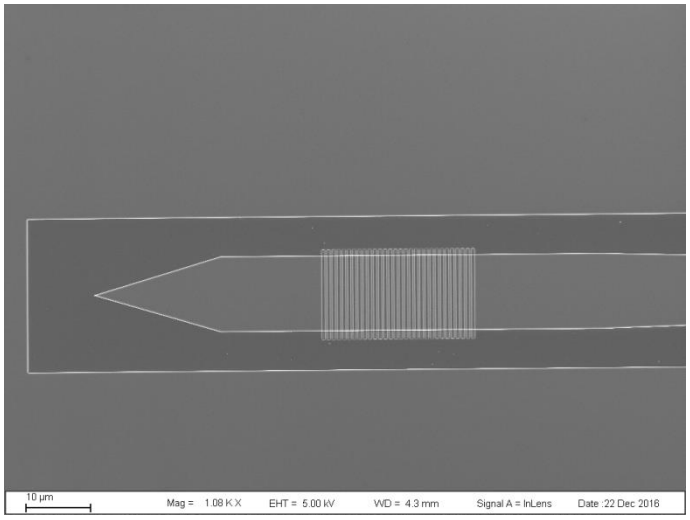

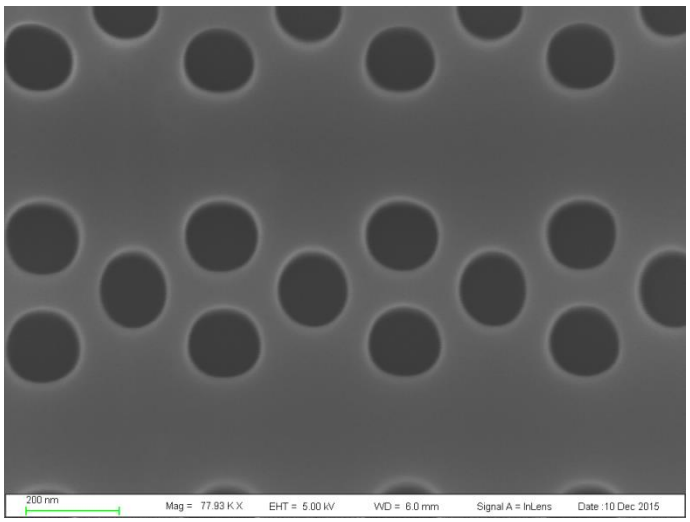

Fig.2.9 The examples of EBL lithography.

2.2.3 Etching Process

In this project, reactive-ion etching (RIE) and deep-reactive-ion etching (DRIE) are utilized. RIE is utilized in etching the alignment marker and grating couplers. The corner of sidewall for RIE is about 85 degree, which is good enough for the alignment markers and grating couplers. Considering the contrast requirement of EBL system, the depth of the alignment marker needs to be 800 nm or more. But the thickness of top-Si layer is only 220 nm or 340 nm. So after etching all top-Si layer away, etching BOX layer is inevitable. The etching recipes are as follows:

(1) The recipe of etching Si with RIE is SF_6 : O_2 : CHF_3 = 30 sccm : 18 sccm : 4 sccm at pressure of 100 Torr and forward power of 125 W. The etching speed of Si is about 4 nm/s. Both the selectivity of Si:AZ5214 and Si:ZEP-520A are 2:1 respectively.

(2) The recipe of etching Si with DRIE is SF_6 : C_4F_8 = 54 sccm : 44 sccm at RF plasma power of 38 W, ICP power of 1650 W, temperature of -8℃

and pressure of 15 Torr. The etching speed of Si is about 50 nm/s. The selectivity of Si:AZ5214 and Si:ZEP-520A are 3: 1 and 7: 1 respectively.

(3) The recipe of etching SiO_2 with RIE is CF_4 : CHF_3 = 30 sccm : 30 sccm at pressure of 150 Torr and forward power of 200 W. The etching speed of SiO_2 is about 33nm/min. The selectivity of SiO_2: AZ5214 is 2:1.

Through some process optimization, it is found that 1.4 μm of AZ5214 is enough for etching 220 nm Si and 580 nm SiO_2 or 340 nm Si and 460 nm SiO_2 to get the "etching markers" of 800 nm depth. For etching strip waveguides, it is only needed to etch away partial or all top-Si layer. With quite high selectivity between Si and ZEP with DRIE (7:1), there would be no problem. Besides, DRIE can offer smoother and more vertical sidewall profile as shown in Fig. 2.10.

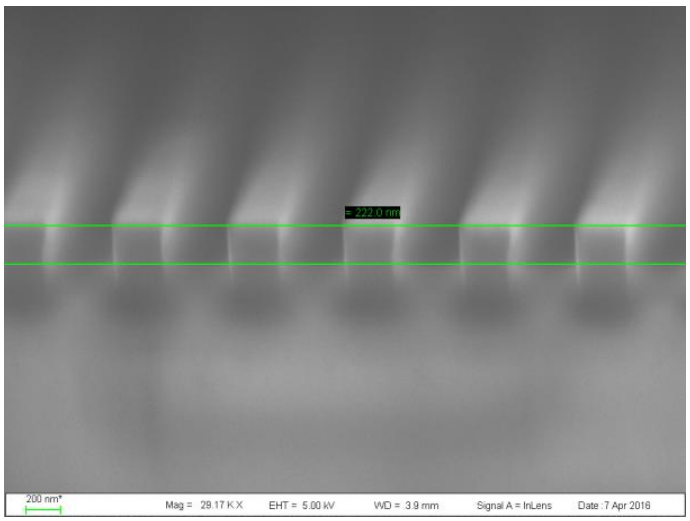

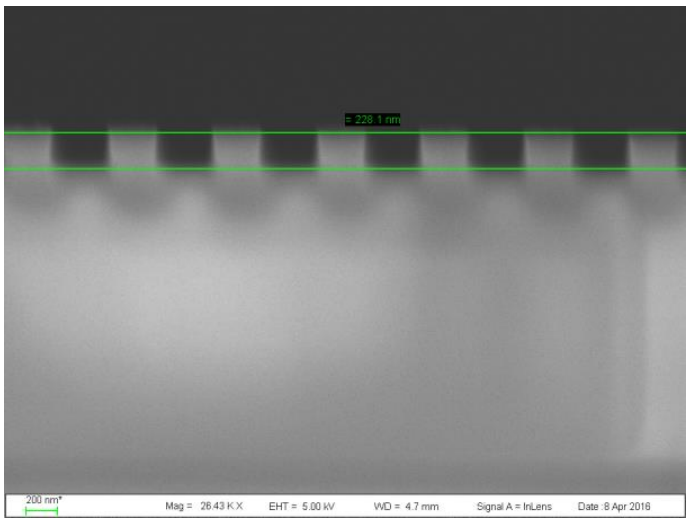

Fig.2.10 The etching profile of DRIE on a 220nm SOI sample.

As confirmed with experiments, the depth of 800 nm is enough for the alignment requirement of our EBL system. The alignment error can be controlled within 50 nm.

2.2.4 Implantation and Electrode Fabrication

In order to protect the undoped region, 700 nm ZEP-520A is used. For higher dose and deeper implantation, thicker hard mask is preferred for protection. Normally, the implantation depth is controlled by the energy applied to accelerate ions. And the dopant concentration is controlled by the product of ion current and implantation time. The heavy implantation is located near the surface of the contact region and aiming at reducing the contact resistance. By conducting the Hall Effect measurement, the doping concentration of heavy implantation and the corresponding contact resistance can be obtained.

In this work, the target concentration of N++ and P++ both are 1E20 ions/cm^3. The

doping sources are arsenic and boron. For the doping of arsenic, the dose is 3E15 ions/cm^2 and the energy is 20 keV. For the doping of boron, the dose is 2E15 ions/cm^2 and the energy is 10 keV. The tilt angle is 7 degree. The rotation angle is 22 degree. Between ZEP-520A and Silicon, a 20 nm thick layer of SiO_2 is applied as a stopping layer to slow down the heavy implantation to stop at the surface of Silicon. This SiO_2 will be removed with buffered oxide etching (BOE) after implantation. After the heavy implantation of Arsenic, an annealing at 950 ℃ for 60 s is applied. As shown in Fig. 2.11, the bulk concentration achieves 1.689E20 ions/cm^3. After the heavy implantation of boron, an annealing at 950 ℃ for 30 s is applied. As shown in Fig. 2.12, the bulk concentration achieves 2.432E19 ions/cm^3. Besides, in order to verify whether 700 nm-thick ZEP-520A can fully isolate the implantations, a set of comparison experiments are conducted. The Hall Effect measurement result of the SOI sample protected by 700 nm-thick ZEP-520A after arsenic implantation is shown in Fig. 2.13. Compared with the Hall Effect measurement result of an original SOI sample as shown in Fig. 2.14, it can be seen that the bulk concentrations are in the same order (1E16 ions/cm^3). So it can be confirmed that 700 nm-thick ZEP-520A is able to fully isolate the heavy implantation.

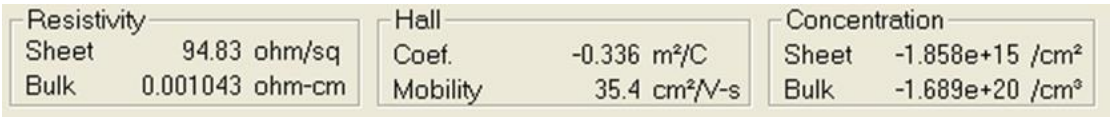

Fig.2.11 The Hall Effect measurement results of arsenic heavy implantation.

Resistivity			Hall			Concentration		
Sheet	701.9	ohm/sq	Coef.	+2.14	m²/C	Sheet	+2.918e+14	/cm²
Bulk	0.008422	ohm-cm	Mobility	30.5	cm²/V-s	Bulk	+2.432e+19	/cm³

Fig.2.12 The Hall Effect measurement results of boron heavy implantation.

Resistivity			Hall			Concentration		
Sheet	1.264e+05	ohm/sq	Coef.	-2.78e+03	m²/C	Sheet	-2.246e+11	/cm²
Bulk	1.391	ohm-cm	Mobility	220	cm²/V-s	Bulk	-2.042e+16	/cm³

Fig.2.13 The Hall Effect measurement results of the sample protected by 700 nm ZEP-520A while arsenic heavy implantation.

Resistivity			Hall			Concentration		
Sheet	1.422e+04	ohm/sq	Coef.	-535	m²/C	Sheet	-1.168e+12	/cm²
Bulk	0.4834	ohm-cm	Mobility	376	cm²/V-s	Bulk	-3.434e+16	/cm³

Fig.2.14 The Hall Effect measurement results of an original sample.

2.3 Characterization Platform

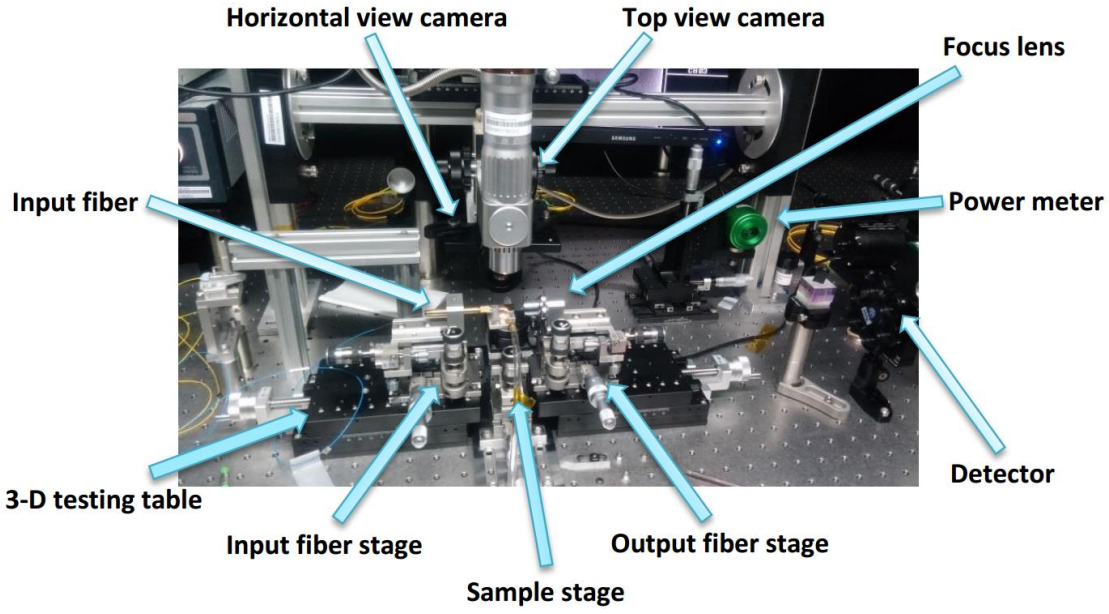

Fig.2.15 The 3D characterization stage.

For the characterization of optical devices, 3-dimension testing stage is used, which is shown in Fig. 2.15. With the top view and horizontal view camera, the position of the fiber tips can be observed on the screen with the help of corresponding software. For butt coupling, the alignment is slightly complex and time consuming. Detailed testing process flow is presented below:

(1) First of all, turned on the laser and connect it with the input fiber. Test the input fiber directly to record the source total output power P_t.

(2) Place the sample onto the sample stage. Adjust the focus of the top view camera to have a clear view of the output butt coupler of waveguide. Use a marker to record the position on the screen. Fixed the cameras.

(3) Lower the sample stage and spare room for the input fiber.

(4) Load the input lens fiber on the input fiber stage and the focus lens on the output fiber stage. Adjust the lens fiber to let the fiber tip overlap with the marker made on screen in step 2. The input lens fiber will act as an equivalent output of the butt coupler in order to adjust the position of the focus lens.

(5) Connect the red light generator to input fiber and turn on. Adjust focus lens to obtain a focused red dot at the center of the laser detector which is placed at the right side.

(6) Replace the red light source with laser source. Turn on the laser detector. With fine tuning, a clear and strong dot can be captured by the laser detector. The goal of all the above steps is to make sure the output light from the

waveguide, which is equivalent by the input lens fiber in step 4, can be focused by the focus lens and captured by the detector.

(7) By replacing the focus lens with the output fiber, the light is transmitted directly from the input fiber to the output fiber. Align these two fibers to get the highest output power P_{ftf}. Then the system loss can be calculated as $P_t - P_{ftf}$.

(8) Load the focus lens to replace the output fiber and adjust it to the correct position.

(9) Withdraw the input fiber and spare space for the sample stage. Lift up the sample stage to the original height. So far the output side is well tuned and should be fixed.

(10) Align the input fiber with the input butt coupler as shown in Fig. 2.16. With the help of two cameras and keeping laser source on, fine tune the position and the vertical/horizontal angle. Once a clear and strong mode is shown on the screen, it means the light transmits through the devices and can be focused by the focus lens and captured by the detector.

(11) After the transmission and the mode profile is confirmed, next is to measure the specific output power. Replace the focus lens with the output fiber. The output fiber is connected with the power meter. Align the output fiber to get the highest output power $\mathrm{P_o}$.

(12) Finally, the total loss of the device can be obtained, which is equal to $\mathrm{P_{ftf}} - \mathrm{P_o}$

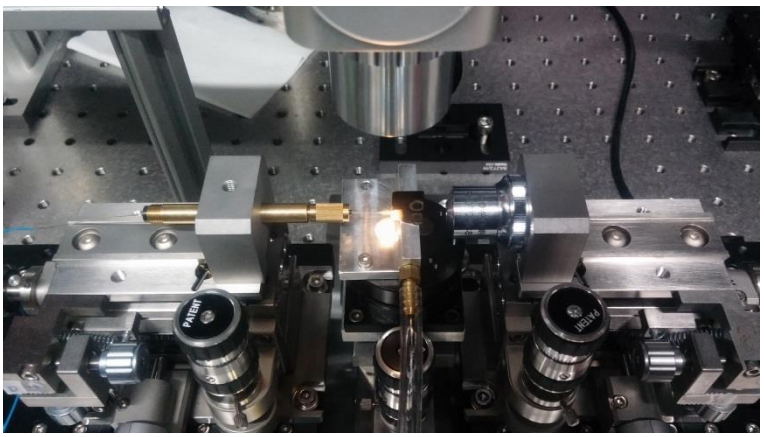

Fig.2.16 The alignment between the input fiber and the butt coupler of waveguide.

However, only knowing the total loss of one device is not enough. A group of devices, such as straight waveguides of different lengths with same couplers, are needed to measure the propagation loss of the waveguide. Fitting the results in line can help to find the coupling loss and propagation loss. The intercept of the fitted line is the coupling loss and the slope is the propagation loss per unit length. The same idea can be applied for testing bending loss.

The testing with grating couplers is easier. As shown in Fig. 2.17, with grating coupling, the waveguides do not need to extend to the edge of wafer (for the purpose of polishing). Besides, grating coupling does not need lens fibers but only need ordinary single mode fibers. Furthermore, testing with grating coupler can avoid the tuning of tilt angle, which saves a lot of time. By directly testing the output power from the input fiber, the total input power for the on-chip device can be obtained. Then similarly, by measuring the transmission loss of straight waveguides of different lengths and fitting the results, the slope will be the propagation loss per unit length of the waveguide. And the intercept is the total coupling loss of the grating coupler. Here

we neglect the system loss of the output fiber, which is usually very small (< 0.1 dB). The detailed testing flow of grating coupling is presented as below:

(1) Load the sample, the input and output fibers.

(2) The input and output angle are adjusted, which depend on the design of grating.

(3) With the help of the top-view camera, adjust the positions of fiber tips to cover the grating coupler.

(4) Fine tune the position of fiber tips to get the highest output power.

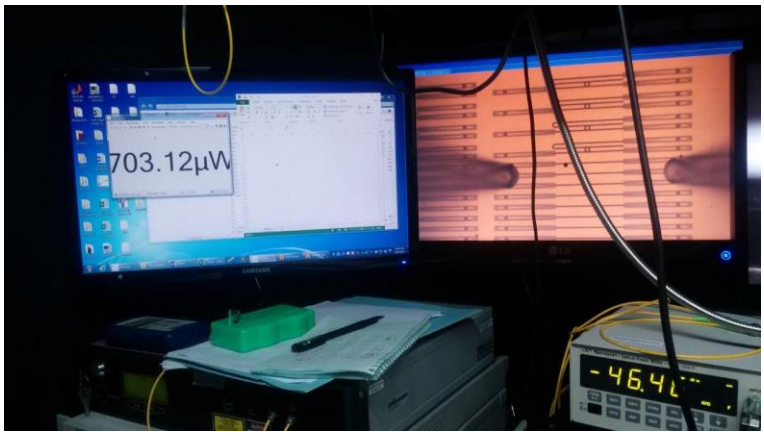

Fig.2.17 The alignment of the input fiber and the waveguide with grating coupler.

For testing of a modulator, in order to measure the wavelength shift efficiency, a DC signal is needed to apply on electrodes. Scan the transmission spectra under different bias with tunable laser source. A higher efficiency means a lower power is needed for the same wavelength shift. In order to measure the modulation speed, a RF signal is needed to apply on electrodes. Before this, the resonance wavelength, such as the resonance dips of microring resonators, needs to be located by scanning the spectrum with tunable laser source. Then replace the tunable laser source with a fixed

wavelength laser source, of which the wavelength is set and fixed at the resonance wavelength. With the sweeping of the RF signal, the resonance dip will shift and the transmission intensity at the wavelength of the resonance dip will change. Then the output optical power is modulated. The detailed characterization procedures of thermal-optic modulators and electro-optic modulators will be demonstrated in chapter 9 of this thesis.

References

[1] A. Taflove, *Computational Electrodynamics: The Finite-Difference Time-Domain Method. Third.* Artech House; 3rd edition, 2005.

[2] D. M. Sullivan, *Electromagnetic Simulation Using the FDTD method*. IEEE, 2000.

[3] K. S. Kunz and R. J. Luebbers, *The Finite Difference Time Domain Method for Electromagnetics*. CRC, 1993.

[4] S. D. Gedney, "Introduction to the Finite-difference Time-domain (FDTD) method for electromagnetics". *Synthesis Lectures on Computational Electromagnetics 6.1* pp. 1–250, 2011.

[5] L. Chrostowski and V. M. Hochberg, *Silicon Photonics Design From Devices to Systems*, Cambridge University Press (2015).

[6] M. Born and E. Wolf, *Principles of optics: electromagnetic theory of*

propagation, interference and diffraction of light. Oxford, Pergamon Press, 1964.

[7] Z. Zhang, G. I. Ng, H. Qiu, W. Wang, X. Guo, M. S. Rouifed, C. Liu, and H. Wang, "Compact microring resonators integrated with grating couplers working at 2 μm wavelength on silicon-on-insulator platform," *Appl. Opt.*, vol. 56, pp. 5444-5449, 2017.

[8] F. Wang, X. Wang, H. Zhou, Q. Zhou, Y. Hao, X. Jiang, M. Wang, J. Yang, "Fano-resonance-based Mach-Zehnder optical switch employing dual-bus coupled ring resonator as two-beam interferometer," *Optical Express*, vol. 17, no. 9, pp. 7708–7716, 2009.

Chapter 3
Fundamental Building Blocks

3.1 Introduction

Silicon photonics based on silicon-on-insulator (SOI) platform has attracted a lot of attention in the last decades. Most of the works focused mainly on the near-infrared (NIR), typically around 1.3-1.6 μm, for data- and telecommunication [1-4]. However, many applications of the mid-infrared (MIR) wavelengths ranging from 2 to 20 μm [5-7], such as chemical and biological sensing, environmental monitoring, industrial process control [8] and nonlinear optics [9], are not sufficiently researched. Besides, the 2 μm wavelength is a promising solution to extend the operating wavelength of communication system to short MIR wavelengths [10]. With the low loss of silicon and SiO_2 at 2 μm wavelength [11,12], SOI platform can be a potential candidate for the integration of photonic devices with mature CMOS compatible fabrication process.

In chapter 1, the basic waveguide theory and the applications based on SOI platform have been demonstrated. In this chapter, fundamental building blocks, such as waveguides, grating couplers, microring resonators operating at 2μm wavelength, are studied in detail. These fundamental building blocks will be utilized to realize other more complicated photonic systems which will be discussed in the subsequent chapters. Coupling light into and out from the on-chip devices is the first problem that

needs to be solved. Two methods are widely used: butt coupling and grating coupling. For SOI platform, due to the lack of natural cleavage plane of Si, polishing process is needed to reduce the coupling loss of butt coupling, which is time consuming and has the risk of contaminations. So grating coupling is more reliable. Grating couplers offer the advantages of more straightforward back-end process, convenience for coupling light in and out from any location on the chip and potentially low coupling loss [13]. Furthermore, grating couplers with an uncomplicated design and fabrication process can reduce the production time and cost. Microrings integrated with grating couplers which act as the basic resonant elements with acceptable extinction ratio (ER), quality factor (Q factor) and compactness are being widely used in various applications in telecommunication band, including filters [14], modulators [15] and sensors [16]. However, only few works of microring resonators integrated with grating couplers working at short Mid-infrared (MIR) wavelengths have been reported. In 2012, Z. Z. Cheng and C. Y. Wong reported a microracetrack integrated with grating couplers based on silicon-on-sapphire (SOS) platform working at 2.75 μm wavelength [13,17]. But typical SOS wafers have more defects, complicated fabrication processes, and are more expensive than the commercial SOI. In the same year, N. Hattasan and F. Leo claimed a microracetrack integrated with grating couplers based on SOI platform [18,19]. However, the fabrication process of their grating couplers is very complex as it needs two times of additional depositions of 10 nm SiO_2 and 160 nm poly-silicon on 220 nm-thick-top-silicon SOI wafer. Besides, in

these two works, the radius of the microracetrack is as large as 150 μm and 50 μm respectively, which is not compact for high density integration. In this chapter, we have designed, fabricated and characterized compact microring resonators (radius = 10 μm, the footprint is only 1/267 of [17] and 1/29 of [19]) operating at 2 μm wavelength integrated with grating couplers using uncomplicated fabrication process on a commercial 340 nm-thick-top-silicon SOI platform. The fabrication is compatible with standard CMOS process and much simpler as there is no need for any additional deposition step. We designed and experimentally demonstrated the low loss grating couplers, with the lowest simulated and measured coupling loss of 4.5 and 6.5 dB respectively, to couple light in and out from the microring resonators. The measurement results of the microring resonators show that the ER can reach 12 dB while the Q factor can achieve 11200, which is suitable for compact on-chip applications operating at 2 μm wavelength.

3.2 Optical I/O Grating Coupler, Waveguides, and Resonators

The compact microring resonators and grating couplers are designed on a SOI wafer with 340 nm-thick-top-silicon and 2 μm-thick buried SiO_2 (BOX) layer. A 1 μm SiO_2 cladding layer is applied. In order to input and output the light efficiently and avoid the outranging of the detector's limitation (- 35 dBm), the first step is to design a

high-efficiency grating coupler. Fig. 3.1(a) represents the schematic of the grating coupler structure. The central wavelength of transmission spectrum can be calculated using the following formula [20]

$$\lambda=\Lambda(n_{eff}(\lambda)-n_c\cdot\sin\theta) \tag{3.1}$$

where Λ is the pitch of grating; $n_{eff}=DC\cdot n_{eff1}+(1-DC)\cdot n_{eff2}$ is the effective index of the grating region in which DC is the duty-cycle, n_{eff1} is the effective index of the grating teeth and n_{eff2} is the effective index of grating slots; n_c is the refractive index of cladding layer material; θ is the input and output angle from vertical of fibers.

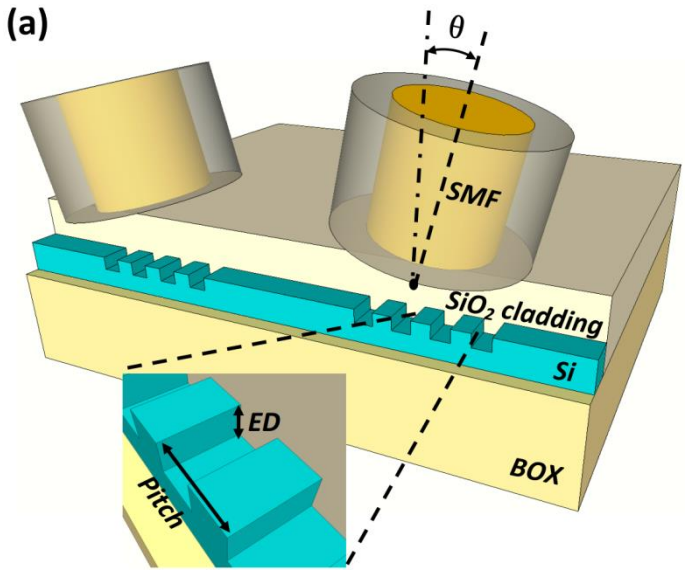

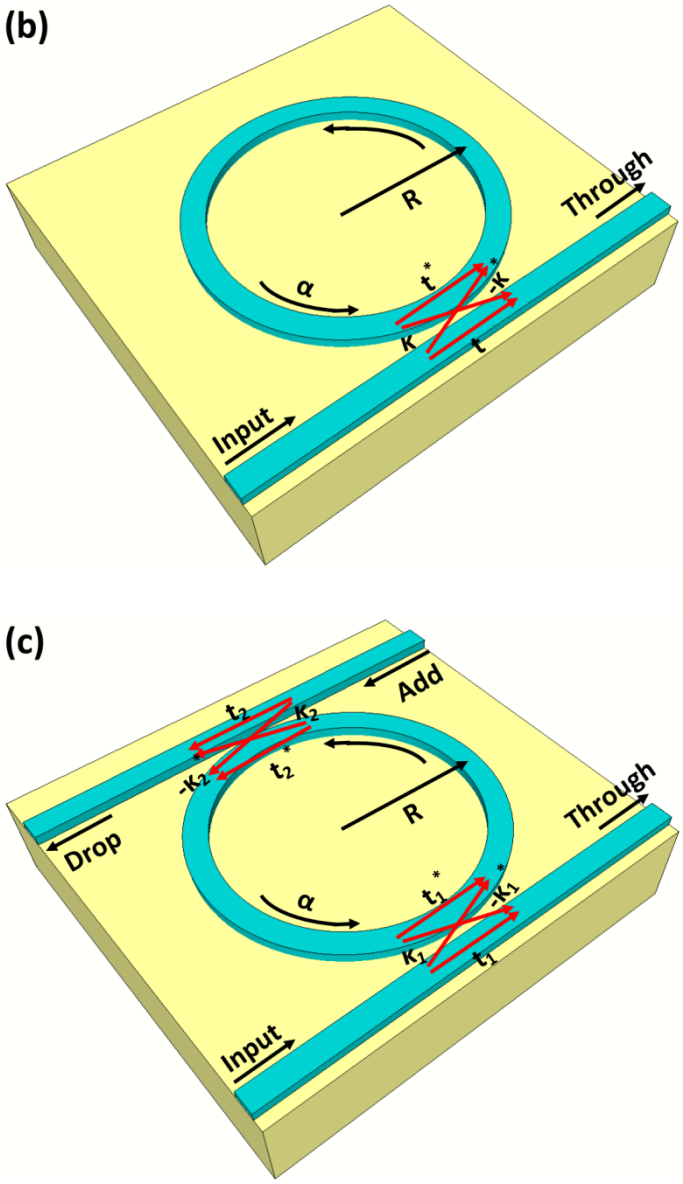

Fig.3.1 (a) The schematic of grating couplers. (b) The schematic of all-pass microring resonator. (c) The schematic of add-drop microring resonator.

Since we use the standard commercial 340 nm-thick-top-silicon SOI sample, the thickness of top silicon and BOX layer are fixed and will not influence the performance. There are mainly four parameters affecting the performance of grating coupler namely: pitch, duty-cycle (DC), etching depth (ED) and input/output angle (θ). Our goal is to achieve the highest coupling efficiency at 2 μm. Base on Equation

(1), we try to find a group of parameters that can set the central wavelength of transmission peak at 2 μm. The effective indices for the grating teeth and slots are calculated with the BeamPROP module of Rsoft software by taking the dispersion into account. By using Equation (1), when pitch = 810 nm, DC = 0.5, ED = 100 nm, θ =13°, the coupling efficiency peak appears at 2 μm wavelength and hence we have chosen these parameters for the initial design. A 13° tilt from vertical is presumed to avoid the second order Bragg reflection back into the waveguide when coupling to the fiber. The width of gratings is set as 12 μm to fully overlap the Gaussian beam from the 9-μm-diameter single-mode fiber (SMF). The width of strip waveguide is 600 nm. 2D Finite-Difference-Time-Domain (FDTD) simulations are carried out with Lumerical FDTD software. According to [21], the refractive indices of silicon (the material of the waveguides) and SiO_2 (the material of the cladding layer and buried layer) at 2 μm wavelength are set as 3.449 and 1.438 respectively. All the input light power has been normalized to 0 dB. Fig. 3.2(a) shows the influence of pitch on the grating coupling efficiency. While sweeping the pitch, the other parameters are fixed: DC = 0.5, ED = 100 nm, θ =13°. It can be seen that, with the increase of pitch from 770 nm to 850 nm, the central wavelength shifts to longer wavelength and the coupling efficiency increases about 2.5 dB. But in order to obtain the highest coupling efficiency at 2 μm (marked by black dashed line), the pitch of 810 nm is selected. In addition, DC also influences the central wavelength and the coupling efficiency. As shown in Fig. 3.2(b), DC increases from 0.1 to 0.9 while maintaining the other

parameter as constant: pitch = 810 nm, ED = 100 nm, θ =13°, the coupling spectrum shifts to longer wavelength. In the meantime, the coupling efficiency reaches the highest value at 2 μm wavelength when DC = 0.5 (marked by black dashed line). So the DC is optimized as 0.5.

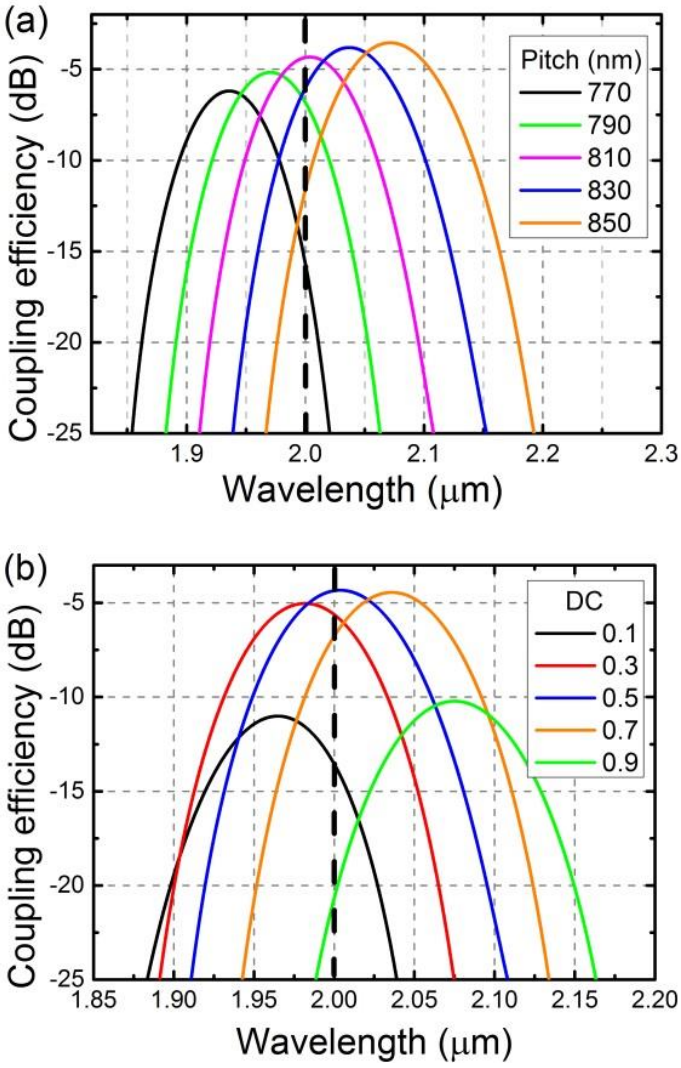

Fig.3.2 (a) The normalized grating coupling efficiency of different pitches under DC = 0.5, ED = 100 nm and θ =13°. (b) The normalized grating coupling efficiency of different DCs under pitch = 810 nm, ED = 100 nm and θ =13°.

Another influencing factor is the etching depth (ED). In Fig. 3.3(a), the pitch of 810

nm, the DC of 0.5 and the input/output angle of 13° are selected and the ED is varied from 60 nm to 200 nm. As can be seen, when ED increases from 60 nm to 200 nm, the central wavelength of the coupling spectrum shifts to shorter wavelength and the coupling efficiency raises firstly then drops when ED > 100 nm. It is noteworthy that the highest coupling efficiency at 2 μm wavelength occurs when ED = 100 nm (marked by black dashed line). Besides, as a part of the testing system, the input/output angle of fiber θ also slightly influences the performance of grating couplers. As illustrated in Fig. 3.3(b), while increasing the angle and keeping other parameters constant (pitch = 810 nm, DC = 0.5, ED = 100 nm), the central wavelength of spectrum moves to the shorter wavelength and the coupling efficiency slightly decreases. When θ = 13°, the central wavelength is located at 2 μm wavelength. So both of the input and output angles of fibers are optimized at 13°. In conclusion, the optimal parameters of grating couplers have been found to be: pitch = 810 nm, DC = 0.5, ED = 100 nm, θ = 13°.

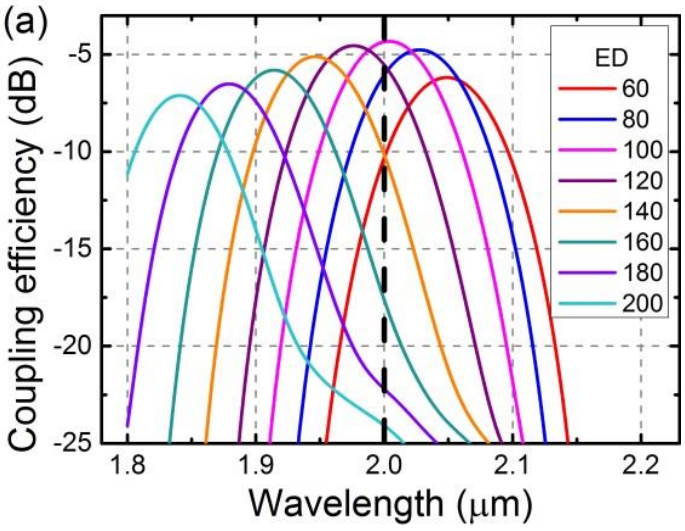

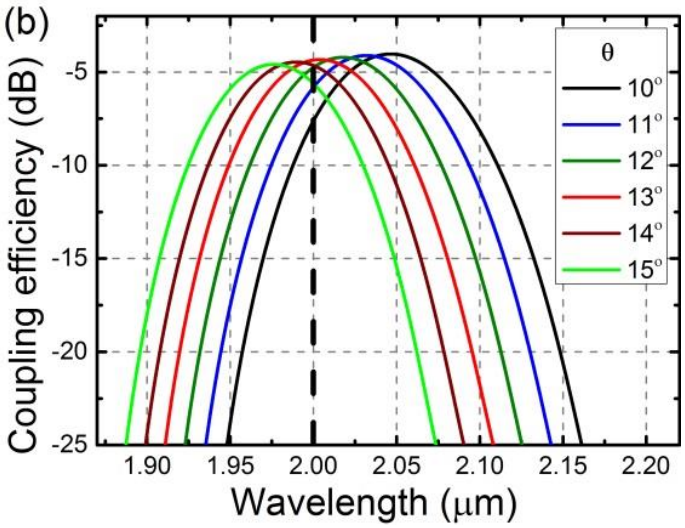

Fig.3.3 (a). The normalized grating coupling efficiency of different ED under pitch = 810 nm, DC = 0.5 and θ =13°. (b). The normalized grating coupling efficiency of different θ under pitch = 810 nm, DC = 0.5 and ED = 100 nm.

After the optimization of grating couplers, we need to calculate and simulate the performance of microring resonators. The schematic of all-pass and add-drop microring resonators are shown in Fig. 3.1(b) and Fig. 3.1(c). Based on the transfer matrix method (TMM), the transmission expression of all-pass microrings and add-drop microrings can be found in [22] as well as the detailed definitions of the relative parameters. α^2 is the round-trip power attenuation of the microring. $t = \sqrt{1-|\kappa|^2}$ is the transmission coefficient and κ is the coupling coefficient of the coupling region between the bus waveguides and the microring. t_1 , κ_1 , t_2 and κ_2 are the corresponding parameters of the two coupling regions of the add-drop microring resonator respectively as marked in Fig. 3.1(c). The effective indices of the strip waveguides (cross-section: 600 nm × 340 nm) under different wavelengths are

calculated with the BeamPROP module of Rsoft software by taking the dispersion into account. The calculation results have been plotted and fitted in Fig. 3.4. The fitted effective refractive index of the microring waveguides can be expressed as $n_{eff\_r} = -0.80642 \cdot \lambda + 4.10585$.

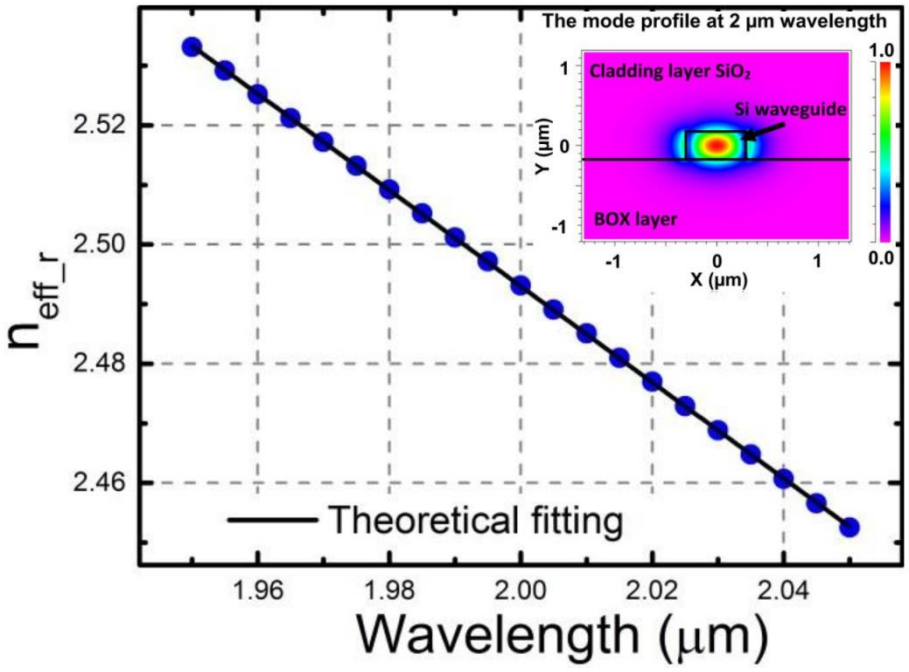

Fig.3.4 The effective refractive indices of the microring waveguide under different wavelengths.

Next, the transmissions spectra based on different parameters including t, κ and α are simulated with Matlab in order to find a group of optimized parameters. When $\alpha < |t|$, $\alpha = |t|$ and $\alpha > |t|$, the all-pass microring resonators are able to work at all coupling states namely under-coupling, critical-coupling and over-coupling respectively. For the symmetric-coupling ($t_1 = t_2$) add-drop microring resonators, since $\alpha < 1$ and $\alpha \cdot |t_2| < |t_1|$ in practice, they always operate at the under-coupling state. The round-trip amplitude attenuation α is mainly determined by the radiation loss and the roughness

scattering loss. In Ref [23], it was concluded that the radiation loss is decreased to the point where it is equal the waveguide propagation loss at a radius of approximately 10 μm at the communication band of 1.55 μm. For the wavelength of 2 μm, a larger radiation loss is expected with the same bending radius as compared to the wavelength of 1.55 μm. In this work, a trade-off between the size and the radiation loss had been made and hence we chose the radius of 10 μm. The radiation loss of R = 10 μm has been experimentally measured to be 0.015 dB/90° at 2 μm wavelength, which is negligible. So the round-trip amplitude attenuation is more influenced by the roughness scattering loss in this work, which is also dependent on the fabrication process. This is because in this work, the device is based on the strip waveguides without any post-surface-smoothen process, thus may result in a higher propagation loss and a smaller round-trip amplitude attenuation. As an initial design, we assume α = 0.98. As plotted in Fig. 3.5(a), the transmission spectra for the all-pass microring resonators of different t have been calculated. It can be clearly seen that while t increases, the resonance peak becomes narrower. When t < 0.98, the depth of resonance peak increases with the increment of t. But when t > 0.98, the resonance peak becomes shallower. As shown in Fig. 3.5(c), there is a very sharp peak of ER at t = 0.98, which corresponds to the critical-coupling state. When t is close to 0.98, though the difference is small, ER drops dramatically. And while t increases, the increasing rate of Q factor speeds up. In order to achieve a high ER with an acceptable Q factor, it is needed to carefully tune the value of t to realize the critical-

coupling condition $\alpha = |t|$. Besides, the transmission spectra for the add-drop microring resonators of different t are calculated and shown in Fig. 3.5(b). While t increases, the resonance peak becomes narrower and shallower. For the symmetric-coupling ($t_1 = t_2$) add-drop microring resonators, because they always operate at the under-coupling state, the changing of ER and Q factor while t increases are monotonous. As seen in Fig. 3.5(d), with the increase of t, ER decreases and Q factor increases. In the meantime, the increasing rate of Q factor also speeds up. So there is a trade-off between Q factor and ER depending on the value of t. In conclusion, the relationship between t and α decides the resonance state and the performance of the microring resonators. In reality, α is usually determined by the fabrication process and the relationship between t and α is normally dependent on the value of t. The transmission coefficient t and the coupling coefficient κ are mainly determined by the material of cladding layer and the gap width between the bus waveguide and the microring resonator. Here because SiO_2 is already selected and fixed as the material of cladding layer, the influence of the cladding layer material can be ignored. In order to find the relationship between the gap width and the transmission coefficient, a 3D FDTD simulation is carried out with Lumerical FDTD software. Here we also set the refractive indices of Si and SiO_2 as 3.449 and 1.438 respectively at 2 μm wavelength. As plotted in Fig. 3.5(e), while the width of the gap becomes larger, the coupling between the bus waveguides and the microring becomes weaker, which leads to the decrease of κ and the increase of t. It is noteworthy that when the gap width is about

165 nm (marked by black dashed line), the value of t is 0.98, which meets the critical-coupling condition $\alpha = |t|$. As a result, for the all-pass microring resonator, the gap width is optimized as 165 nm. The curve shown in Fig. 3.5(e) is also suitable for finding the corresponding value of t of the add-drop microring resonators.

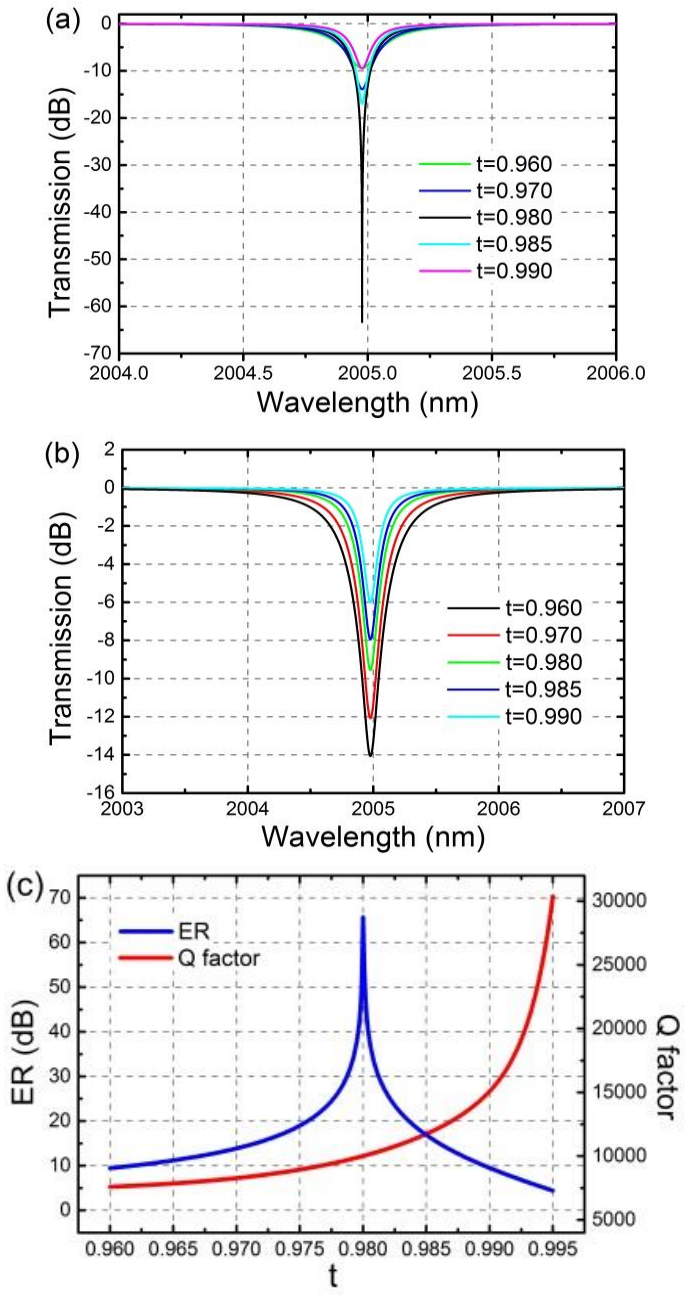

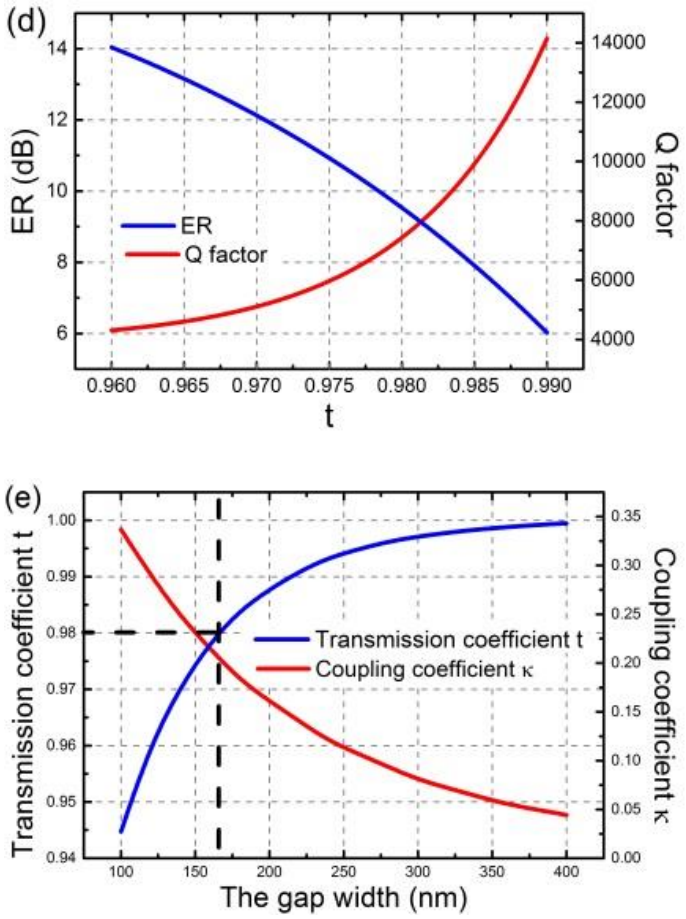

Fig.3.5 (a) The transmission spectra for the all-pass microring resonators of different t when α = 0.98. (b) The transmission spectra for the add-drop microring resonators of different t when α = 0.98. (c) The ER and Q factor of the all-pass microring resonators as the function of the transmission coefficient t. (d) The ER and Q factor of the add-drop microring resonators as the function of the transmission coefficient t. (e) The transmission coefficient t and coupling coefficient as the function of the gap width.

3.3 Fabrication and Characterization

The all-pass and add-drop microring resonators integrated with grating couplers are

fabricated on a SOI wafer with a 340 nm-thick top silicon layer and a 2 μm-thick buried oxide (BOX) layer. Both the grating layer and the waveguide layer are defined with electron beam lithography (EBL). The grating layer is partially etched to the depth of 100 nm with reactive ion etching (RIE). The waveguide layer is fully etched to the BOX layer with deep reactive ion etching (DRIE) in order to have a straight and smooth sidewall. Then the sample is coated with a cladding layer of 1 μm SiO_2 with plasma-enhanced chemical vapor deposition (PECVD). Various pitches and DCs are fabricated to measure and analyze the grating couplers' performance. For the microring resonators, the radii of the microrings are set as 10 μm. The all-pass microring resonator with the gap width of 165 nm and the symmetric-coupling add-drop microring resonator with the gap width of 200 nm are fabricated. The scanning-electron-microscope (SEM) images are shown in Fig. 3.6. As shown in Fig. 3.6(a), the pyramid-shaped end facets are designed to avoid the Fabry–Pérot resonance formed by the two flat end surfaces. The width of grating coupler is 12 μm. The width of strip waveguide is 600 nm. The length of the taper connecting the grating coupler and the strip waveguide is 200 μm.

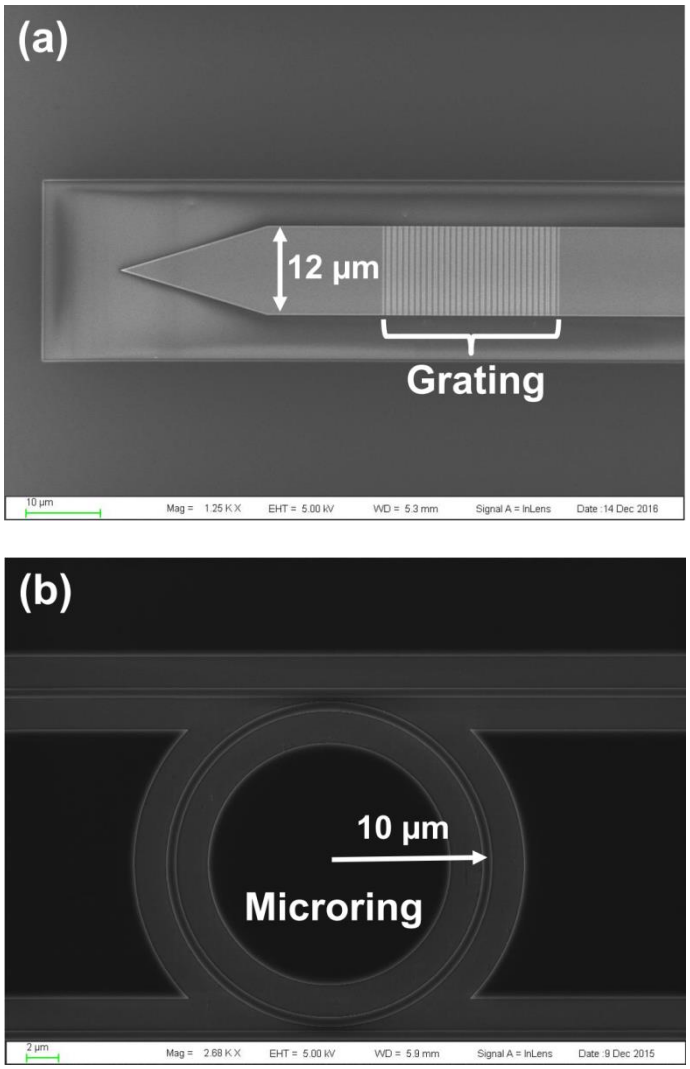

Fig.3.6 (a) The SEM image of the grating coupler. (b) The SEM image of the microring resonator.

The characterizations of grating couplers and microring resonators are carried out at room temperature. The light generated by a Thorlabs FP laser diode is coupled into a single-mode optical fiber. With the in-line polarization controllers, the polarization of light is tuned to be fundamental TE mode. With two symmetric fiber holders on the input and output 5 axis stages, the angle of fibers can be tuned between 10° and 15° from vertical. At the output side, an Artifex extended InGaAs photodetector is utilized

to measure the output power.

The grating couplers of different dimensions are tested with the fixed 2 μm wavelength laser. Fig. 3.7(a) shows the coupling efficiency at 2 μm wavelength as a function of pitch while DC = 0.5 and θ =13°. It can be seen that the highest coupling efficiency occurs when pitch = 800 nm, which is smaller than the optimized simulation results (810 nm). This is due to the shallower etching depth (~94nm) than the expected 100 nm. A smaller pitch is needed to compensate the influence of the under-etched depth. Moreover, as shown in Fig. 3.7(b), the highest coupling efficiency at 2 μm wavelength happens when DC = 0.35. The reason is also due to the under-etched depth. In order to obtain the highest coupling efficiency at 2 μm wavelength, a smaller DC is needed to balance the effect of the under-etching depth. As plotted in Fig. 3.7(c), the optimized input/output angle is 13°, which fits the simulation results well. Besides, the transmission spectrums of different grating pitches under DC = 0.5 and θ = 13° can be found in Fig. 3.7(d). Due to the limitation of testing system, the scanning range can be only 1880 nm ~ 2010 nm wavelength. The noise of the spectra at the longer wavelength in Fig. 3.7(d) is due to the unstable power of the input laser source. It can be clearly seen that while the pitch increases, the central wavelength moves to longer wavelength. When the pitch = 800 nm (purple curve), the central wavelength is 2 μm (marked by black dashed line), which fits well with the experimental results shown in Fig. 3.7(a). The lowest coupling loss at 2 μm wavelength obtained experimentally is 6.5 dB. The difference between the simulation

and experimental results may come from the fiber loss and mode mismatch between the silicon waveguide mode and that of the single mode fiber. By increasing the width of grating, the coupling efficiency of grating coupler can be further improved [15]. Compared with the reported grating couplers operating in NIR bands, such as the coupling efficiency of -1 dB in [24], -0.77 dB in [25], -0.9 dB in [26], and -1.8 dB in [27], the coupling efficiency of our grating coupler still has rooms to improve. Various methods can be utilized to improve the coupling efficiency, for instance, by using the 1-D/2-D sub-wavelength-grating structure in the grating coupler, by setting the backside metal mirror between the grating layer and the BOX layer, and with the simultaneous apodization of two structural parameters (the grating period and the fill-factor) along with the optimization of the grating coupler etching depth.

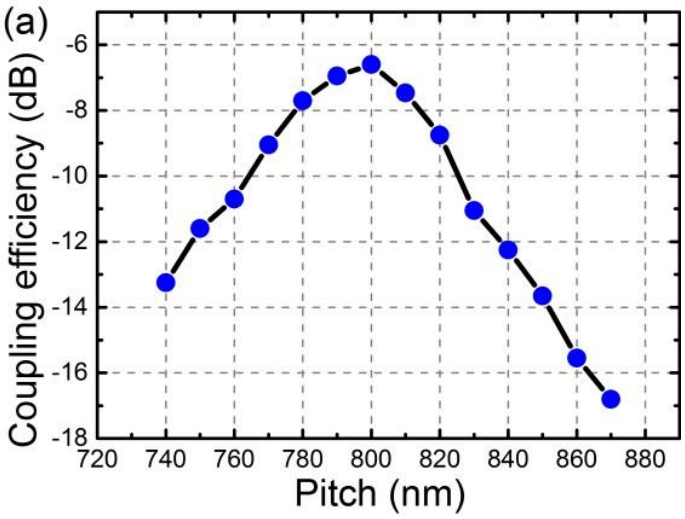

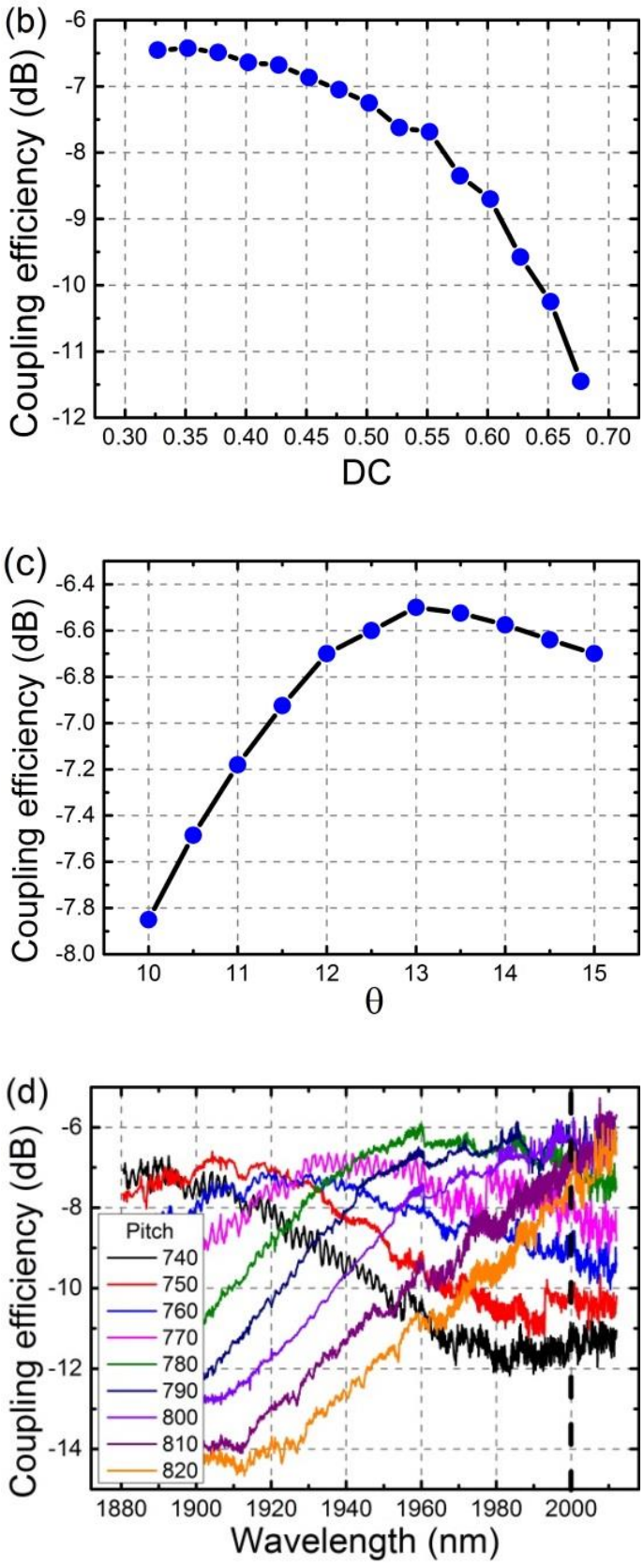

Fig.3.7 (a) The normalized grating coupling efficiency of different grating pitches

under DC = 0.5 and θ =13°. (b) The normalized grating coupling efficiency of different DC under pitch = 810 nm and θ =13°. (c) The normalized grating coupling efficiency of different θ under pitch = 810 nm and DC = 0.5. (d) The normalized transmission spectra of different grating pitches under DC = 0.5 and θ =13°.

Fig. 3.8(a) and Fig. 3.8(b) show the transmission spectra of the all-pass and add-drop microring resonators respectively. As it can be seen in Fig. 3.8(a), when the gap width of the all-pass microring resonator is 165 nm, the extinction ratio (ER) of the all-pass microring resonator can reach 12 dB and the full-width-at-half-maximum (FWHM) is 0.28 nm, which corresponds to the Q factor of 7120. According to the fitted numerical model, the fitted parameters can be found as t = 0.9669, α = 0.9790 and R = 10.0325 μm. Besides, as shown in Fig. 3.8(b), when the gap width of the add-drop microring resonator is 200 nm, the ER is 8 dB and the FWHM is 0.179 nm, which corresponds to a Q factor of 11200. The fitted parameters can be found as t_1 = t_2 = 0.9863 (symmetric-coupling design is utilized in this experiment), α = 0.9820 and R = 9.994 μm. There are two possible reasons for the slight difference of the value of t between the 3D FDTD simulations and the experimental fitted results. One reason is that because the fitted numerical model is calculated based on the effective refractive indices simulated with BeamPROP software, there is probably a difference of the adopted refractive indices at different wavelengths around 2 μm between Lumerical FDTD and BeamPROP software. The second reason is that since the cladding layer SiO_2 is deposited with PECVD, the quality and the refractive index may not be the

same as the BOX layer or the theoretical value. Moreover, in this experiment, due to the utilization of the wide waveguides (600 nm), the confinement of light is better but in consequence the coupling between the microring and the bus waveguide is weaker. By using racetracks to increase the coupling length and coupling efficiency, the ER and Q factor can be improved [19]. In addition, with a larger radius, the radiation loss can be further reduced. However, there will be a trade-off between compactness and performance. Besides, by utilizing the post fabrication microelectronic treatments namely Piranha etch/HF cycling and annealing, the surface roughness can be further reduced as well as the round-trip power loss. We expect that the Q factor and the ER can be further improved.

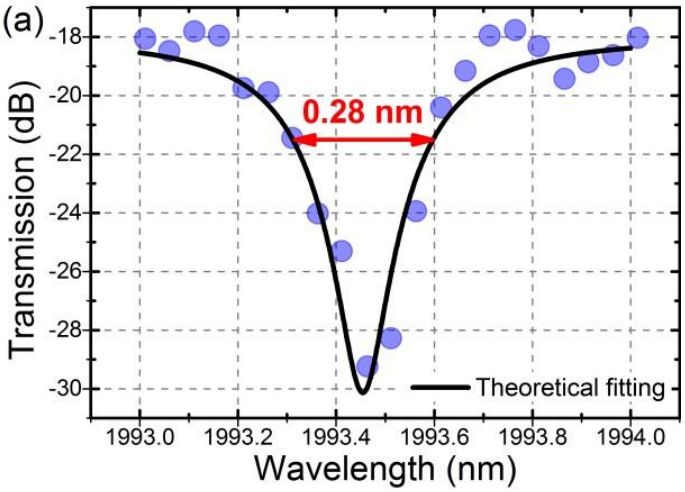

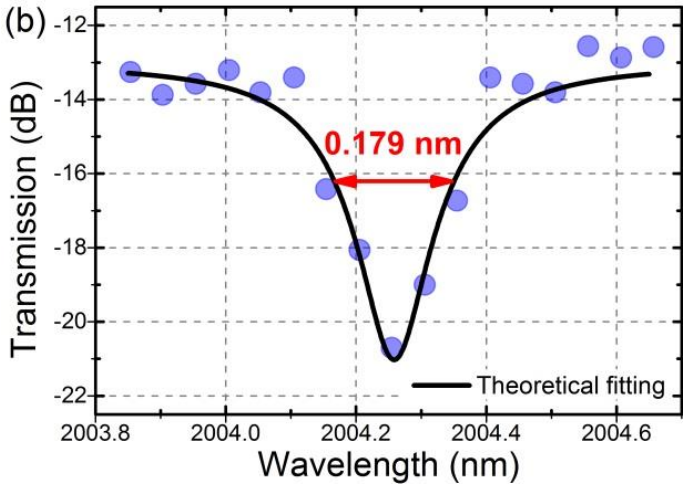

Fig.3.8 (a) The transmission spectrum of the all-pass microring resonator when the gap width is 160 nm. (b) The transmission spectrum of the add-drop microring resonator when the gap width is 200 nm.

3.4 Conclusion and Discussions

In this chapter, we report on the design, fabrication and characterization of some fundamental building blocks of SOI-based photonics integrated circuits on 340 nm-thick-top-silicon SOI platform operating at 2 μm wavelength, which include the waveguides, grating couplers, and microring resonators. The lowest simulated and experimental coupling loss of the grating couplers are 4.5 dB and 6.5 dB respectively. The ER and Q factor of the microring resonators can achieve 12 dB and 11200 respectively. The ease of fabrication of the grating coupler makes it more convenient to be utilized for on-chip integration application. The compact microring resonator shows good potential in applications such as integrated sensors, modulators and nonlinear optics at 2 μm wavelength.

References

[1] Z. Xiao, F. Luan, T. Liow, J. Zhang, and P. Shum, “Design for broadband high-efficiency grating couplers,” *Opt. Lett.*, vol. 37, no. 4, pp. 530–532, 2012.

[2] Y. Tang, Z. Wang, L. Wosinski, U. Westergren, and S. He, “Highly efficient nonuniform grating coupler for silicon-on-insulator nanophotonic circuits,” *Opt. Lett.*, vol. 35, no. 8, pp. 1290–1292, 2010.

[3] J. H. Song, F. E. Doany, A. K. Medhin, N. Dupuis, B. G. Lee, and F. R. Libsch, “Polarization-independent nonuniform grating couplers on silicon-on-insulator,” *Opt. Lett.*, vol. 40, no. 17, pp. 3941–3944, 2015.

[4] J. Zhang, J. Yanga, H. Lu, W. Wu, J. Huang, and S. Chang, “Subwavelength TE/TM grating coupler based on silicon-on-insulator,” *Infrared Physics & Technology*, vol. 71, pp. 542–546, 2015.

[5] A. Spott, Y. Liu, T. Baehr-Jones, R. Ilic, and M. Hochberg, “Silicon waveguides and ring resonators at 5.5 m,” *Appl. Phys. Lett.*, vol. 97, no. 21, pp. 213501(1)–213501(3), 2010.

[6] D. E Hagan and A. P Knights, “Mechanisms for optical loss in SOI waveguides for mid-infrared wavelengths around 2 μm,” *J. Opt.*, vol. 19, pp. 025801, 2017.

[7] M. M. Milosevic, M. Nedeljkovic, T. M. Ben Masaud, E. Jaberansary, H. M. H. Chong, N. G. Emerson, G. T. Reed, and G. Z. Mashanovich, “Silicon waveguides and devices for the mid-infrared,” *Appl. Phys. Lett.*, vol. 101, pp. 121105, 2012.

[8] R. Soref, “Mid-infrared photonics in silicon and germanium,” *Nature Photon.*, vol. 4, pp. 495–497, 2010.

[9] B. Kuyken et al., “Mid-infrared to telecom-band supercontinuum generation in highly nonlinear silicon-on-insulator wire waveguides,” *Opt. Exp.*, vol. 19, no. 22, pp. 4401–4403, 2011.

[10] R. Soref, “Mid-Infrared Photonics,” *Opt. Fiber Comm. Conf.*, Mar. 2015.

[11] M. Nedeljkovic, R. Soref, and G. Z. Mashanovich, “Free-carrier electroabsorption and electro-refraction modulation in group IV materials at mid-infrared wavelengths,” *Proc. of SPIE.*, vol. 8266, pp. 82660Y(1) – 82660Y(7), 2012.

[12] G. Roelkens, U. Dave, A. Gassenq, N. Hattasan, C. Hu, B. Kuyken, F. Leo, A. Malik, M. Muneeb, E. Ryckeboer, S. Uvin, Z. Hens, R. Baets, Y. Shimura, F. Gencarelli, B. Vincent, R. Loo, J. V. Campenhout, L. Cerutti, J. Rodriguez, E. Tournié, X. Chen, M. Nedeljkovic, G. Mashanovich, L. Shen, N. Healy, A. C. Peacock, X. Liu, R. Osgood, and W. Green, “Silicon-based heterogeneous photonic integrated circuits for the mid-infrared,” *Optical Material Express*, vol. 3, no. 9, pp. 1523-1536, 2013.

[13] Z. Cheng, X. Chen, C. Y. Wong, K. Xu, C. K. Y. Fung, Y. M. Chen, and H. K. Tsang, “Mid-Infrared Grating Couplers for Silicon-on-Sapphire Waveguides,” *IEEE Photon. J.*, vol. 4, no. 1, pp. 104-113, 2012.

[14] T. Hu, W. J. Wang, C. Qiu, P. Yu, H. Y. Qiu, Y. Zhao, X. Q. Jiang, and J. Y. Yang,

"Thermally tunable filters based on third-order microring resonators for WDM applications," *IEEE Photonics Technol. Lett.*, vol. 24, no. 6, pp. 524-526, 2012.

[15] F. Y. Gardes, A. Brimont, P. Sanchis, G. Rasigade, D. Marris-Morini, L. O'Faolain, F. Dong, J. M. Fedeli, P. Dumon, L. Vivien, T. F. Krauss, G. T. Reed, and J. Martí, "High-speed modulation of a compact silicon ring resonator based on a reverse-biased pn diode," *Opt. Express*, vol. 17, no. 24, pp. 21986–21991, 2009.

[16] C. Ciminelli, F. Dell' Olio, D. Conteduca, C. M. Campanella, and M. N. Armenise, "High performance SOI microring resonator for biochemical sensing," *Opt. Laser Tech.*, vol. 59, pp. 60-67, 2014.

[17] C. Y. Wong, Z. Cheng, X. Chen, K. Xu, C. K. Y. Fung, Y. M. Chen, and H. K. Tsang, "Characterization of Mid-Infrared Silicon-on-Sapphire Microring Resonators with Thermal Tuning," *IEEE Photon. J.*, vol. 4, no. 4, pp. 1095–1102, 2012.

[18] N. Hattasan, B. Kuyken, F. Leo, E. M. P. Ryckeboer, D. Vermeulen, and G. Roelkens, "High-Efficiency SOI Fiber-to-Chip Grating Couplers and Low-Loss Waveguides for the Short-Wave Infrared," *IEEE Photon. Tech. Lett.*, vol. 24, no. 17, pp. 1536–1538, 2012.

[19] F. Leo, B. Kuyken, N. Hattasan, R. Baets, and G. Roelkens, "Passive SOI devices for the Short-wave-infrared," *16th European Conference on Integrated Optics*, 2012.

[20] L. Chrostowski and V. M. Hochberg, *Silicon Photonics Design from Devices to Systems*, Cambridge Univ. Press (2015).

[21] Edward D. Palik, *Handbook of Optical Constants of Solids (Book 3)*, Academic Press. Nov. (1997).

[22] D. G. Rabus, *Integrated microring resonators*, Springer., 127, (2007).

[23] W. Bogaerts, P. Dumon, D. Tailaert, P. Jaenen, J. Wouters, S. Beckx, V. Wiaux, and R. G. Baets, "Compact wavelength-selective functions in siliconon-insulator photonic wires," *IEEE Journal of Selected Topics in Quantum Electronics*, vol. 12, no. 6, 2006.

[24] J. Zhang, J. Yang, H. Lu, W. Wu, J. Huang, S. Chang, "Subwavelength TE/TM grating coupler based on silicon-on-insulator," *Infrared Physics & Technology*, vol. 71, pp. 542-546, 2015.

[25] S. Nambiar and S. K. Selvaraja, "High-efficiency broad-bandwidth subwavelength grating-based fiber-chip coupler in silicon-on-insulator" *Optical Engineering*, vol. 57, no. 1, pp. 1, 2018.

[26] R. Marchetti, C. Lacava, A. Khokhar, X. Chen, I. Cristiani, D. J. Richardson, G. T. Reed, P. Petropoulos, and P. Minzioni, "High-efficiency grating-couplers: demonstration of a new design strategy," *Scientific Reports*, vol. 7, pp. 16670, 2017.

[27] Y. Luo, Z. Nong, S. Gao, H. Huang, Y. Zhu, L. Liu, L. Zhou, J. Xu, L. Liu, S. Yu, and X. Cai, "Low-loss two-dimensional silicon photonic grating coupler with a

backside metal mirror," *Opt. Lett.*, vol. 43, pp. 474-477, 2018.

Chapter 4
Tunable and Convertible Electromagnetically Induced Transparency (EIT)/Fano System

4.1 Introduction

In the past decades, the electromagnetically induced transparency (EIT) [1] in photonics, which possesses a narrow optical transparency peak residing in a broader absorption valley [2], has attracted considerable research interests for its wide applications in slow and fast light [3], modulation [4,5], optical signal processing [6] and sensing [7]. Similar to the quantum interference in a multi-level atomic system, the EIT originates from the coupling between two resonators such as microring resonators. Microring resonators which act as the basic resonant elements with acceptable extinction ratio (ER), bandwidth and compactness are being used for various applications, including filters [8-10], modulators [11], and sensors [12]. In addition, microring resonators have also been widely employed to construct the EIT systems. In 2006, Q. Xu first observed experimentally the EIT-like spectrum in an integrated two micro-size silicon microring resonators based system with a quality factor (Q factor) of 17000 [13,14]. In 2011, S. Darmawan and Y. Zhang observed a EIT-like spectrum in a ring-bus-ring geometry synergistically integrated with Mach-Zehnder interferometer with a Q factor of 18000 [15,16]. For these two systems, one of the drawbacks is that they required a very tight perimeter difference (< 10 nm) between these two microrings which is not easy to control in fabrication. Another

drawback is its large footprint due to the use of two microrings. Besides microring resonators, there are also some EIT systems based on other types of resonators being reported. For example, C. Zhang obtained a EIT-like spectrum in a system consisting of two coupled microtoroids with diameters of 60.4 μm and 67.5 μm which makes it non-compact [17]. K. Totsuka proposed a microsphere based coupled system to realize the EIT-like spectrum [18]. However, the microsphere structure is not compatible with the standard complementary-metal-oxide-semiconductor (CMOS) fabrication process and cannot be fabricated by the planar lightwave technology. Furthermore, in 2011, B. Li reported a series of research on the Fano transmission in a single whispering-gallery microresonator and indirectly coupled whispering-gallery microresonators [19,20]. In 2013, P. Yu obtained a Fano transmission in a waveguide F-P resonator side-coupled lossy nanobeam cavity [21]. Y. Xiao utilized a single polydimethylsiloxane-coated silica microtoroid to realize an EIT-like transmission [22]. In 2014, Q. Huang observed an EIT-like transmission in a two-bus waveguide coupled microdisk resonator [9,23].

However, the conversion between the EIT and Fano transmission, which is very interesting, was rarely reported. In 2006, W. Liang experimentally claimed the conversion between the Fano-like transmission and the multi-peaks transmission by changing the coupling strength in a Fabry–Perot etalon-microtoroid resonator coupled system [24], but, the existence of EIT transmission was not confirmed and the mechanism behind the conversion is not thoroughly discussed. In 2009, C. –H. Dong

experimentally demonstrated modified transmission spectrums, including EIT-like and Fano-like lineshapes, based on the two-mode interference in a single silica microsphere by tuning the relative position of the fiber taper [25]. However, the common drawback of these two devices is based on fiber technique, which leads to a much larger footprint and is incompatible with planar waveguide fabrication process. Besides, if Fano and EIT resonances can be tuned and converted in one on-chip system, the versatility, flexibility and compatibility can be much improved. Large volume integration on a single monolithic wafer then becomes possible.

In the first part of this chapter, an all-pass microring-Bragg gratings (APMR-BG) based coupling resonant system is theoretically and experimentally demonstrated to generate the EIT-like spectrum. In this system, the EIT-like spectrum originates from the light coupling between two resonators. It consists of a Fabry–Pérot (F-P) resonator formed by two sections of Bragg gratings and a microring resonator. Different from the reported structures, this resonant coupling system has only one microring resonator thus making it very compact. Besides, due to the large bandwidth of the F-P resonance spectrum, it is easier to overlap the resonance wavelengths of the microring resonator and the F-P resonator to obtain the EIT-like spectrum. As a result, the fabrication tolerance can be improved. A numerical model based on the transfer matrix method is developed to investigate the working principle and the influence of the physical dimensional parameters on the device performance. The fabrication of the APMR-BG based coupling resonant system is realized on a SOI platform. The

EIT-like spectrum with an ER of 12 dB and a Q factor of 20200 was obtained experimentally. Based on our numerical model, a slow light with a group delay of 38 ps is obtained.

In the second part of this chapter, based on the APMR-BG system, we demonstrate the conversion between the EIT and Fano transmission and reveal the mechanism behind the conversion. The EIT and Fano transmission both originate from the coupling between the light paths of the two resonators (a microring resonator and a Fabry–Perot (F-P) resonator), which is similar to the quantum interference in a multi-level atomic system. By tuning the coupling strength between the microring resonator and the F-P resonator formed by two Bragg gratings, an abrupt phase shift of the light in the microring resonator occurs, leading to the transformation from constructive interference to destructive interference between the two resonators. Consequently, it triggers the transformation of the transmission from the EIT lineshape to the Fano lineshape. We theoretically analyzed the conversion of the transmission by using the transfer matrix method. The conversion between the EIT and Fano transmission was also experimentally demonstrated using the coupled-resonator system designed and fabricated on a SOI platform and the measured results show good agreement with the theoretical prediction. This system also has the advantage of a small footprint consisting of only one microring resonator and one bus waveguide with Bragg gratings, and the fabrication process is compatible with the planar waveguide fabrication process. The capability to have different transmission

lineshapes can pave the way for the future active tuning applications, such as optical switching, modulation, sensing, and on-chip time delay lines.

In the last part of this chapter, thermally tunable Fano and EIT resonances are theoretically and experimentally demonstrated based on a Mach–Zehnder interferometer (MZI)-assisted Bragg grating-microring coupled resonant system on SOI platform. By changing the optical path length of the MZI arm, the effective round-trip power attenuation of the MZI-assisted microring can be tuned, which leads to the change of the coupling status between the two resonators. When the coupling changes between destructive and constructive status, the resonance lineshape is converted between Fano and EIT lineshape. We theoretically calculated and analyzed the performance of the system with a specially developed numerical model based on the transfer matrix method. The system was designed, fabricated and characterized on a commercial 220 nm-top-silicon-layer silicon-on-insulator (SOI) platform. The tuning and conversion between Fano and EIT resonances by thermo-optical effect have been experimentally observed and verified with good agreement between the experimental data and the simulations.

4.2 Simulation, Fabrication and Characterization of APMR-BG System

The schematic of the APMR-BG based coupling resonant system is shown in Fig. 4.1. Two sections of Bragg gratings are located in the bus waveguide at the two sides of

the microring. They perform as partially reflective elements to form an F-P resonator. The coupling between the micro-ring resonator and the F-P resonator gives rise to the EIT-like spectrum. For the all-pass microring resonator, the transmission can be expressed as [26]:

$$t_{ring\_thru} = \frac{-\alpha + te^{-i\varphi}}{-\alpha t^{*} + e^{-i\varphi}} \tag{4.1}$$

where $\varphi = \frac{2\pi n_{eff} L_r}{\lambda}$ is the round-trip phase; $t = \sqrt{1-|k|^2}$ is the transmission coefficient and k is the coupling coefficient; t^{*} is the conjugation of t; $\alpha^2 = e^{-\delta_r L_r}$ is the round-trip-power-attenuation in which the δ_r is the propagation loss of microring waveguide per unit length; $L_r = 2\pi R$ is the cavity length of the microring in which the R is the radius; λ is the wavelength; n_{eff} is the effective refractive index of the microring waveguide.

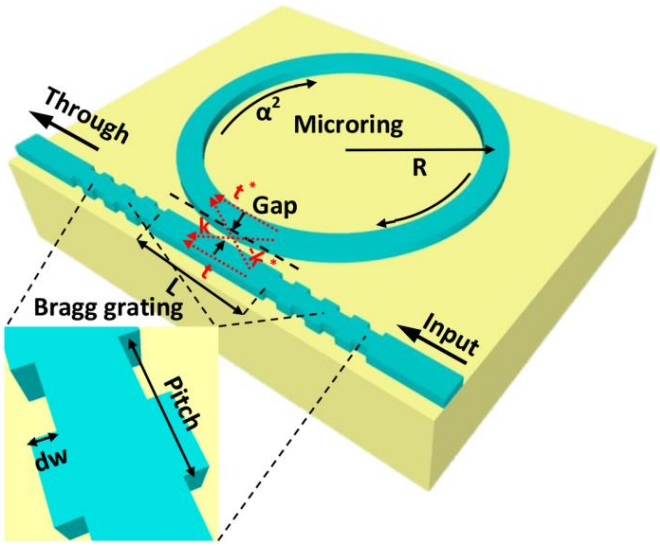

Fig.4.1 The schematic of the APMR-BG based coupling resonant system.

Because the Bragg gratings act as partially reflective elements, a part of the light in

the bus waveguide is reflected and then transmits inversely. The transfer matrix of the microring should take this part of light into account. Hence, it can be written as:

$$T_{ring} = \begin{pmatrix} 1/t_{ring\_thru} & 0 \\ 0 & t_{ring\_thru\_inv} \end{pmatrix} \tag{4.2}$$

where $t_{ring\_thru\_inv} = \dfrac{-\alpha + t^* e^{i\varphi}}{-\alpha t + e^{i\varphi}}$ is the inverse transmission of the microring resonator. For the Bragg grating, it can be regarded as a periodic structure consisting of wide waveguide segments, narrow waveguide segments and reflective interfaces. The transfer matrix of the Bragg grating can be written as [26]:

$$T_{Bg} = (T_{w\_wg\_sgmt} \cdot T_{w\_to\_n} \cdot T_{n\_wg\_sgmt} \cdot T_{n\_to\_w})^N \tag{4.3}$$

where $T_{w\_wg\_sgmt} = \begin{pmatrix} e^{-i\beta_w l_w} & 0 \\ 0 & e^{i\beta_w l_w} \end{pmatrix}$ and $T_{n\_wg\_sgmt} = \begin{pmatrix} e^{-i\beta_n l_n} & 0 \\ 0 & e^{i\beta_n l_n} \end{pmatrix}$ are the transfer matrices of the wide and the narrow waveguide segments, respectively; the $\beta_w = \dfrac{2\pi n_{eff\_w}}{\lambda} - i\dfrac{\delta_w}{2}$ is the complex propagation constant of the wide waveguide segments and l_w is the length; $\beta_n = \dfrac{2\pi n_{eff\_n}}{\lambda} - i\dfrac{\delta_n}{2}$ is the complex propagation constant of the narrow waveguide segments and l_n is the length; n_{eff_w} and n_{eff_n} are the effective refractive indices of the wide and narrow waveguide segments; δ_w and δ_n are the propagation loss of the wide and narrow waveguides per unit length; $T_{w\_to\_n} = \begin{pmatrix} \dfrac{n_1+n_2}{2\sqrt{n_1 n_2}} & \dfrac{n_1-n_2}{2\sqrt{n_1 n_2}} \\ \dfrac{n_1-n_2}{2\sqrt{n_1 n_2}} & \dfrac{n_1+n_2}{2\sqrt{n_1 n_2}} \end{pmatrix}$ and $T_{n\_to\_w} = \begin{pmatrix} \dfrac{n_2+n_1}{2\sqrt{n_1 n_2}} & \dfrac{n_2-n_1}{2\sqrt{n_1 n_2}} \\ \dfrac{n_2-n_1}{2\sqrt{n_1 n_2}} & \dfrac{n_2+n_1}{2\sqrt{n_1 n_2}} \end{pmatrix}$ are the transfer matrices of the 'wide-to-narrow' and the 'narrow-to-wide' reflective interfaces

respectively; n_1 and n_2 are the effective refractive indices of the wide and narrow waveguide segments respectively. The whole section of Bragg grating is periodic and the exponent N is the number of Bragg grating periods. With all the basic components defined, the equation for the APMR-BG based coupling resonant system can be expressed by combining these transfer matrices as:

$$T_{in} = T_{Bg} \cdot T_{wg} \cdot T_{ring} \cdot T_{wg} \cdot T_{Bg} \cdot T_{out} \tag{4.4}$$

where $T_{wg} = \begin{pmatrix} e^{-i\beta_w \frac{L}{2}} & 0 \\ 0 & e^{i\beta_w \frac{L}{2}} \end{pmatrix}$ is the matrix of the waveguide of the F-P cavity, in which L is the cavity length. In this work, the inverse transfer matrix expression for the structures is adopted. The effective indices for the waveguides of the different widths and wavelengths are calculated with the BeamPROP module of Rsoft software by taking the dispersion into account.

When only the F-P resonator is present and L is an integral multiple of Bragg grating pitch, a 'U'-like spectrum can be observed as shown in Fig. 4.2(a). The Bragg resonance wavelength (λ_B) is the center wavelength of the 'U' lineshape. When the resonance peaks of the microring overlap with the 'U' lineshape, the resonances are formed in both the F-P resonator and the microring resonator. Consequently, at the wavelengths of the microring peaks, the coupling between them occurs and generates the EIT-like spectra (circled by red dashed lines) as shown in Fig. 4.2(b). It is noteworthy that, because the EIT-like spectra happens at the slope region of the 'U'

lineshape, the two dips beside the EIT peak are not completely symmetrical. As shown in the inset of Fig. 4.2(b), here we define the ER as the transmission difference between the EIT peak and the dip closer to the λ_B.

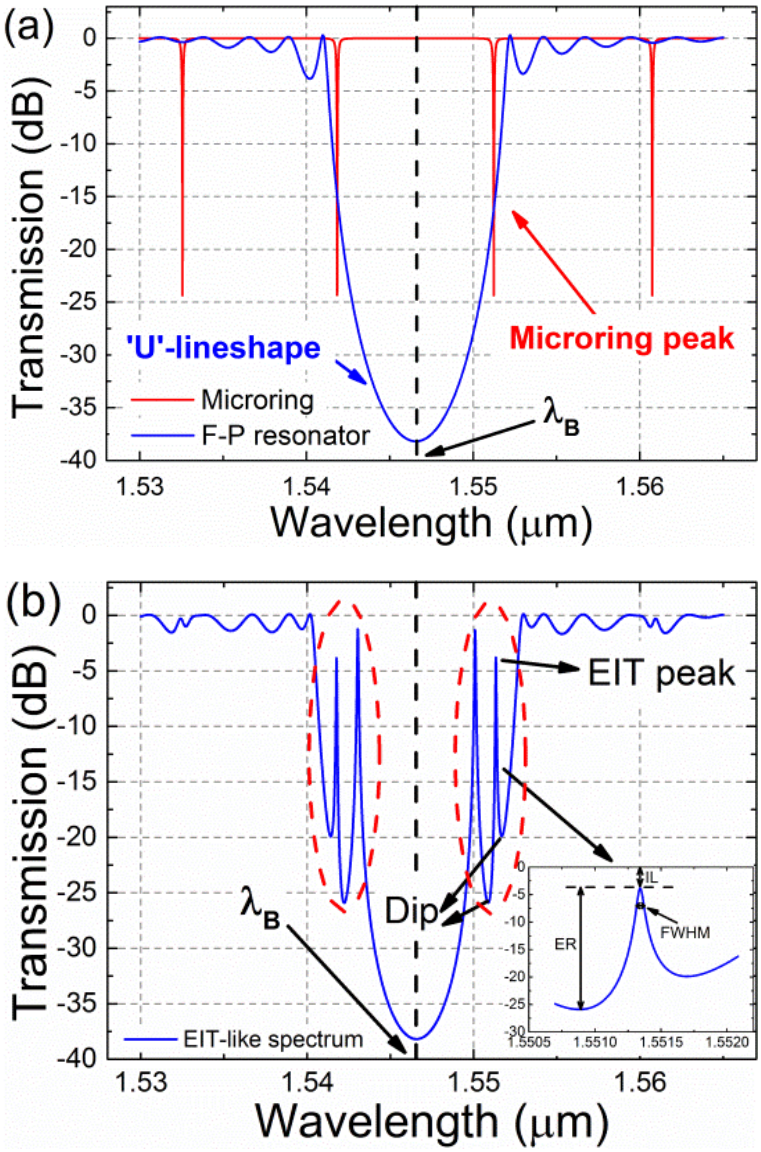

Fig.4.2 (a) The normalized transmission spectra of the microring and the F-P resonator. (b) The normalized EIT-like spectrum of the APMR-BG based coupling resonant system.

For the Bragg gratings, there are three main parameters influencing the device

performance. They are the pitch, the number of Bragg grating periods (N) and the width of Bragg grating corrugation (dw). For the microring resonator, there are two main influencing parameters, the coupling coefficient (k) and the round-trip-power-attenuation (α^2). In this work, the influence of the above five parameters on two most important properties of the EIT-like spectrum namely the insertion loss (IL) and the full-width-at-half-maximum (FWHM) are discussed. A low IL is a guarantee of good transmission transparency at the wavelength of the EIT peak. A small FWHM represents a high Q factor which gives rise to a sharp EIT lineshape. In this work, we aim at building highly sensitive sensors and low switching power modulators based on this APMR-BG system. Hence, our focus is to optimize the system for a high Q factor and a sharp EIT lineshape. Besides, as shown in Fig. 4.2(b), the overlap between two microring resonance peaks and the 'U' lineshape generates two EIT-like spectra (circled by red dashed lines). The generation and working principles of these two EIT-like spectra are the identical. The EIT-like spectra occur at the left side can be analyzed with the same approach as the ones occur at the right side. In the following theoretical analysis, we only discuss the right EIT-like spectrum to avoid repetition. Furthermore, two different group delays in one device could be realized with appropriate designs.

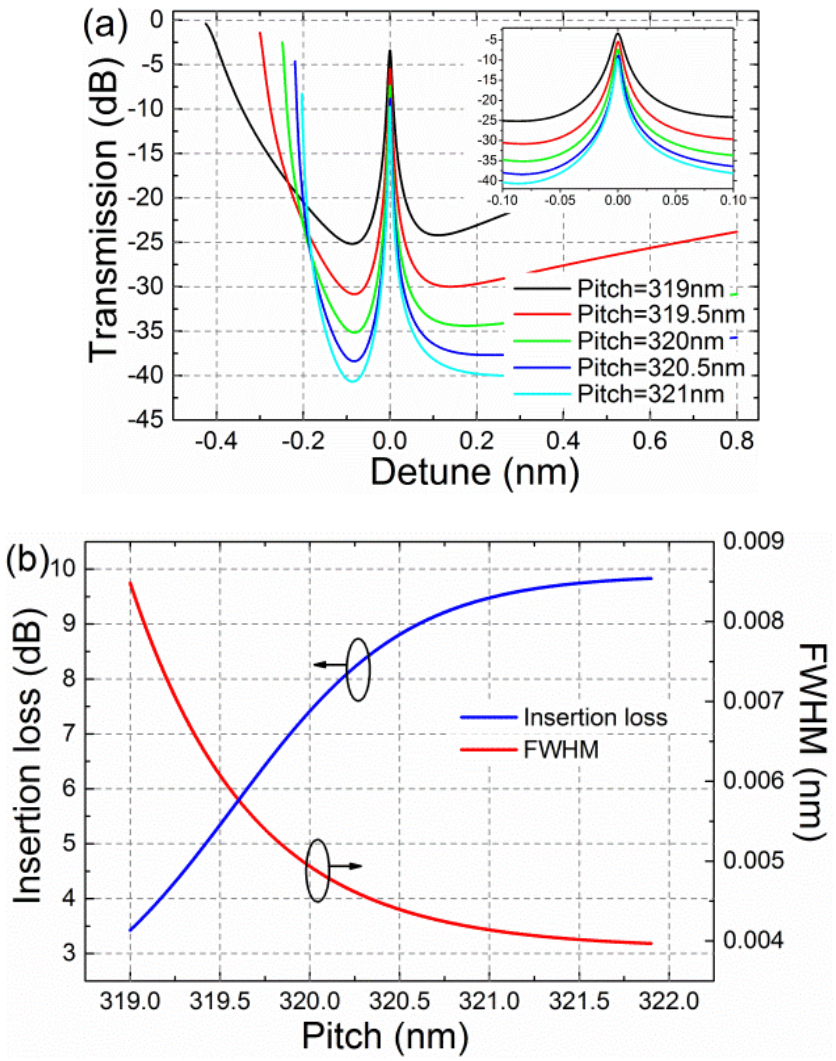

Fig.4.3 (a) The normalized EIT-like spectra of different pitches under N = 90, dw = 20 nm, k = 0.35i, α^2 = 0.9981. (b) The relation between the pitch, IL and FWHM under N = 90, dw = 20 nm, k = 0.35i, α^2 = 0.9981.

Firstly, in order to investigate the influence of the pitch, we set the other parameters as: N = 90, dw = 20 nm, k = 0.35i, α^2 = 0.9981. Fig. 3.3(a) illustrates the normalized EIT-like spectra at several different pitches. When the pitch increases, the 'U' lineshape moves to the longer wavelength but the resonance peak of the microring resonator stays at the original wavelength, which means the resonance peak of the

microring resonator is closer to the λ_B. At the same time, the FWHM is improved but the transmission is degraded. As shown in Fig. 4.3(b), when the pitch < 319.6 nm, the FWHM decreases rapidly and the IL increases rapidly with the increase of the pitch. Although the IL is low in this region, the FWHM is too wide for realizing highly sensitive sensors and low switching power modulators. When the pitch > 320.3 nm, the rates of change of the FWHM and the IL both drop significantly and their values become saturated. However, the IL is too high in this region. So in order to achieve a small FWHM and a low IL at the same time, it is necessary to keep the pitch size between 319.6 nm and 320.3 nm.

The influence of N is also examined. By controlling the N, the depth of the 'U' lineshape can be manipulated. A larger N leads to a deeper 'U' lineshape. As a result of the above discussion, we set the pitch = 320 nm and maintain the rest of parameters. As shown in Fig. 4.4(a), the FWHM becomes smaller with the increasing value of N, which results in a higher Q factor and a sharper curve but at expense of a higher IL. Although the FWHM at N = 130 is only one-sixth of the value at N = 50, the IL at N = 130 is 16 times higher than that at N = 50. So there is a trade-off between FWHM and IL. As plotted in Fig. 4.4(b), the IL rises with the increase of N. It is noteworthy that the rate of change of the IL slightly increases when N > 100 and the rate of change of FWHM slows down significantly when the N > 80. Besides, when N < 70 the FWHM is too large and when N > 100 the IL is too high. So in order to achieve a balance between the FWHM and the IL, setting the N between 70 and

100 is a reasonable choice.

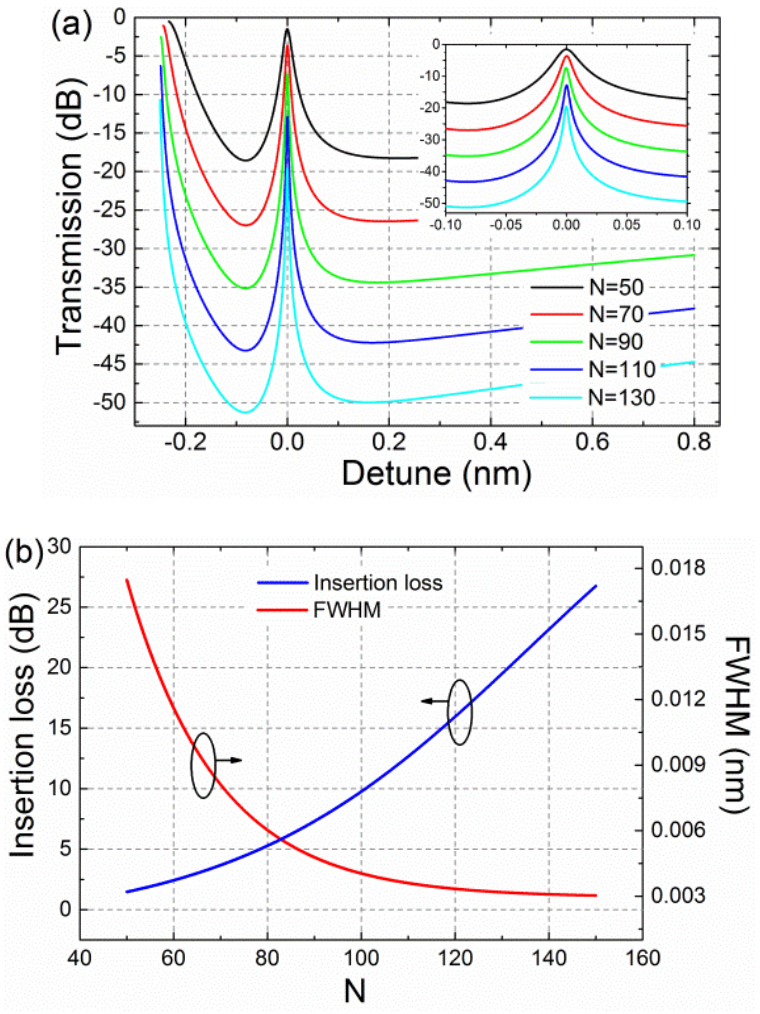

Fig.4.4 (a) The normalized EIT-like transmission spectra at different N under pitch = 320 nm, dw = 20 nm, k = 0.35i, α^2 = 0.9981. (b) The relation between the N, IL and FWHM under pitch = 320 nm, dw = 20 nm, k = 0.35i, α^2 = 0.9981.

The width of the Bragg grating corrugation is also a very important parameter controlling the width and the depth of the 'U' lineshape. Fig. 4.5(a) shows the influence of different dw on the EIT-like spectrum. As discussed above, the pitch and the N are set as 320 nm and 90 respectively. The rest of the parameters are set as the same as dw = 20 nm, k = 0.35i, α^2 = 0.9981. The increase of dw gives rise to a blue-

shift and the deepening of the 'U' lineshape, which results in the increase of the IL and the decrease of the FWHM. As depicted in Fig. 4.5(b), the rate of change of the FWHM drops when dw > 17 nm and the increasing of IL slows down when dw > 21nm. Besides, the IL is too high when dw > 21 nm and the FWHM is also too large when dw < 17nm. Therefore, in order to have a small FWHM with a low IL, the dw is chosen to be between 17 nm and 21 nm.

Next, the influence of the microring resonator related parameters, the coupling coefficient k and the round-trip-power-attenuation α^2, will be discussed. Several spectra of different k are presented in Fig. 4.6(a). The pitch, N and dw are chosen as 320 nm, 90 and 20 nm respectively from the optimal ranges as discussed above. α^2 is kept the same as 0.9981. It is observed that while k value is increasing, IL decreases along with a broadening of the EIT peak. Besides, with the increase of k, the ER of the microring resonance peak decreases and the bandwidth increases. The broader overlap region between the microring resonance peak and the 'U' lineshape gives rise to the simultaneous broadening of the two dips and a more symmetrical EIT peak. The value of k can be manipulated by controlling the width of the waveguides and the gap width between the microring and the bus waveguide. A smaller gap width gives rise to a larger k. As shown in Fig. 4.6(b), when $k_{\text{real part}} > 0.3$, the rate of increase of the FWHM rises. The rate of change of the IL slightly decreases when $k_{\text{real part}} < 0.25$ and $k_{\text{real part}} > 0.5$. The regions $k_{\text{real part}} < 0.3$ and $k_{\text{real part}} > 0.5$ should be avoided due to the high IL and the large FWHM respectively. In order to balance the IL and FWHM,

setting the k in between 0.3i and 0.5i is preferred.

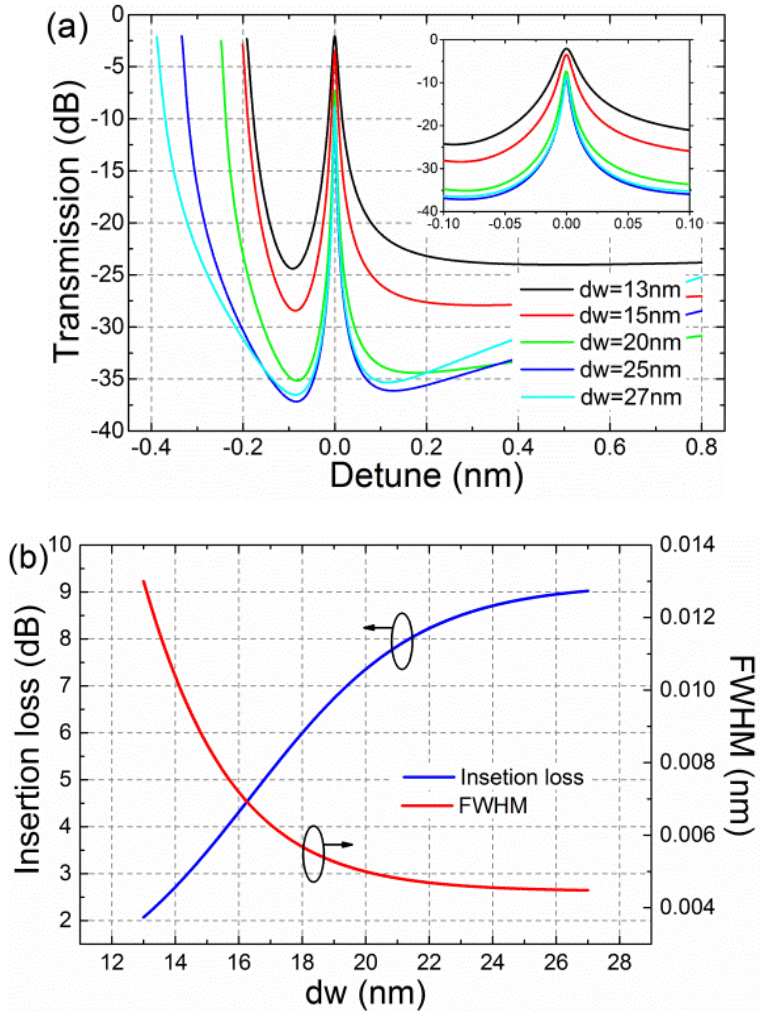

Fig.4.5 (a) The normalized EIT-like transmission spectra at different dw under pitch = 320 nm, N = 90, k = 0.35i, α^2 = 0.9981. (b) The relation between the dw, IL and FWHM under pitch = 320 nm, N = 90, k = 0.35i, α^2 = 0.9981.

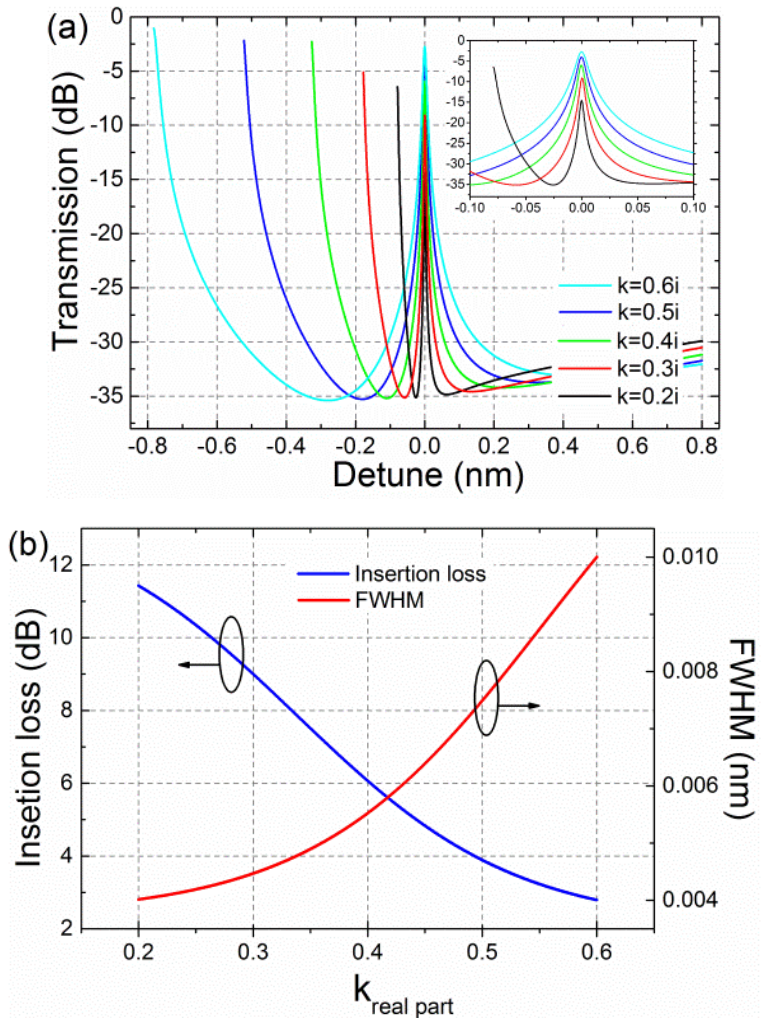

Fig.4.6 (a) The normalized EIT-like transmission spectra at different k under pitch = 320 nm, N = 90, dw = 20 nm, α^2 = 0.9981. (b) The relation between the k, IL and FWHM under pitch = 320 nm, N = 90, dw = 20 nm, α^2 = 0.9981.

The round-trip-power-attenuation α^2 acts as another crucial parameter indicating the intrinsic Q factor of the microring. As shown in Fig. 4.7(a), it can be noticed that the sharper lineshape and the higher transmission can be achieved by reducing the round trip loss. So a higher α^2 is preferred. Fig. 4.7(b) shows the IL and the FWHM as functions of α^2. It can be observed that both the IL and the FWHM decrease with the increase of α^2. This is because the light propagation in a low-loss microring resonator

brings about a high optical transparency and intrinsic Q factor. In order to achieve a high α^2, the fabrication process needs to be improved to smoothen the surface of the microring waveguide. Besides, the radius of microring (R) needs to be large enough to avoid the radiation loss. From simulation results, the radiation loss can be neglected when R > 10 μm at the wavelength of 1.55 μm.

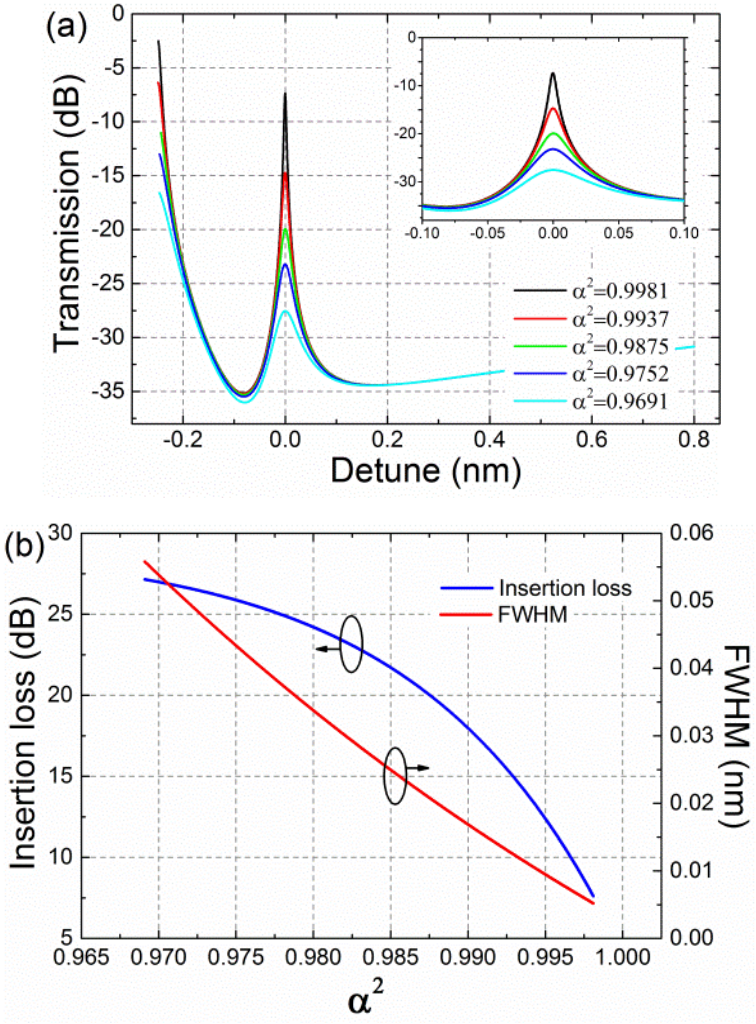

Fig.4.7 (a) The normalized EIT-like transmission spectra at different α^2 under pitch = 320 nm, N = 90, dw = 20 nm, k = 0.35i. (b) The relation between the α^2, IL and FWHM under pitch = 320 nm, N = 90, dw = 20 nm, k = 0.35i.

An APMR-BG based coupling resonant system was fabricated on a SOI wafer with a

220-nm-thick top silicon layer and a 2 μm-thick buried oxide (BOX) layer. Both the grating layer and the waveguide layer are defined with electron beam lithography (EBL). The grating layer is partially etched to the depth of 70 nm with reactive ion etching (RIE). The waveguide layer is fully etched to BOX layer with deep reactive ion etching (DRIE). Then the sample is coated with a cladding layer of 1 μm SiO_2 with plasma-enhanced chemical vapor deposition (PECVD). The radius of the APMR is designed to be 10 μm and the width of waveguides is designed to be 500 nm. The width of the gap between the bus waveguide and the microring is set to be 130 nm. The pitch of Bragg gratings and the depth of corrugations are designed to be 320 nm and 20 nm respectively. The number of periods is 100 for each Bragg grating. The duty cycle is 50%. The cavity length of the F-P resonator between two Bragg gratings is 3.2 μm which equals to 10 times of the pitch.

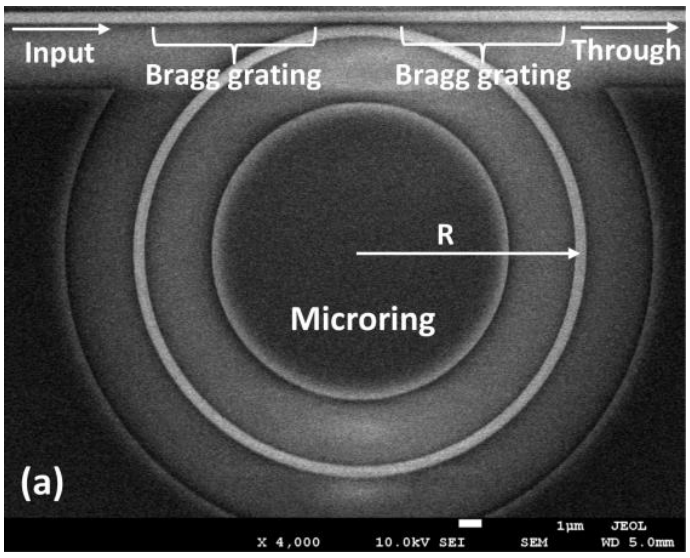

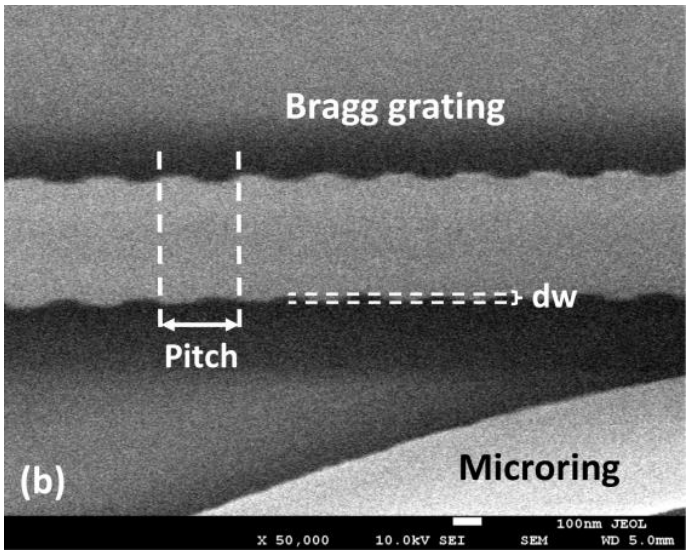

Fig.4.8 (a) The SEM image of the APMR-BG based coupling resonant system. (b) The zoomed-in SEM image of the Bragg grating.

Fig. 4.8(a) and Fig. 4.8(b) show the SEM images of the APMR-BG based coupling resonant system and the Bragg grating respectively. As presented in Fig. 4.9(a), by using the proposed numerical model, the theoretical calculation result agrees well with the experimental result. The input light power is +5 dBm. The grating couplers are utilized to couple light into and out from the waveguide. The coupling loss is about 4.5 dB for each grating coupler. The imbalance of the transmission curve at the two sides of the 'U' lineshape is due to the uneven coupling efficiency of the grating couplers at different wavelengths. Due to some roughness of the Bragg gratings, the bottom of the 'U' lineshape is not as smooth as the fitting curve but this will not influence the EIT-like spectra in this device. As shown, the bandwidth of the 'U' lineshape is slightly larger than the free spectrum range (FSR) of the microring resonator, which results in the dual EIT-like spectra. The measured ILs of these two

EIT-like spectra are 7 dB and 7.5 dB. The FWHMs are 0.124 nm and 0.077 nm which correspond to the Q factors of 12500 and 20200 respectively. The ERs are 11.5 dB and 12 dB. The fitting parameters are obtained as follows: P = 321.6 nm, N = 100, dw = 11.4 nm, R = 10.2 μm, k = 0.53i, $\alpha^2 = 0.9778$.

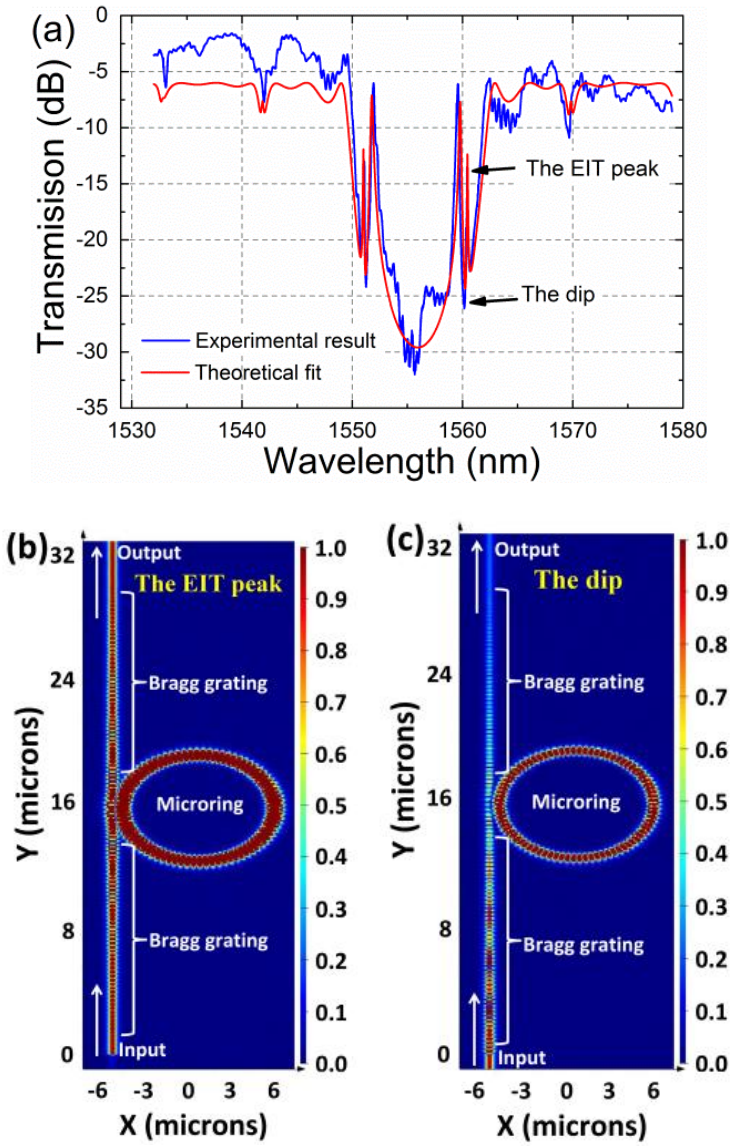

Fig.4.9 (a) The fitting between the experimental result and the theoretical calculation result. (b) The light propagation of the EIT-like spectrum peak at the wavelength of 1560.432 nm. (c) The light propagation of the EIT-like spectrum dip at the

wavelength of 1560.252 nm.

As shown in Fig. 4.8(b), the Bragg grating corrugations are not in the desired rectangular shape, thus the actual dw (11.4 nm) is smaller than the designed value of 20 nm. So more periods (N = 100) are needed to increase the reflectivity to compensate the effects of the actual smaller value of dw. Besides, due to the fabrication roughness, the relatively high propagation loss of the microring waveguide results in the low round-trip-power-attenuation α^2 (0.9778), which suppresses the Q factor and results in the high IL (7.5 dB). The high coupling coefficient k = 0.53i, caused by the narrow gap (130 nm) between the bus waveguide and the microring, also influences the Q factor. Further improvements can be achieved through further process optimization, for example, to improve the sharpness of the corrugation of the Bragg gratings and to smoothen the surface of waveguides through thermal oxidation followed by buffer oxide etching [27]. Increasing the gap width to have a smaller k will also improve the Q factor.

By using the Lumerical FDTD software, the light propagations at the peak and the dip of the EIT-like spectrum in the right part of the 'U' lineshape can be obtained as shown in Fig. 4.9(b) and Fig. 4.9(c) with normalized power. It can be clearly seen that the microring is in resonance at both of these two wavelengths. Due to the phase shift, constructive coupling and destructive coupling are formed at the wavelengths of the peak and the dip respectively. A measured ER value of 12 dB was obtained experimentally.

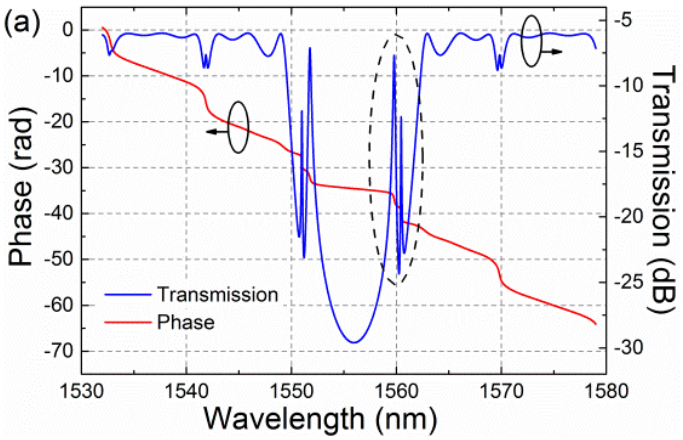
(a)
Phase (rad)
Transmission (dB)
Wavelength (nm)
Transmission
Phase

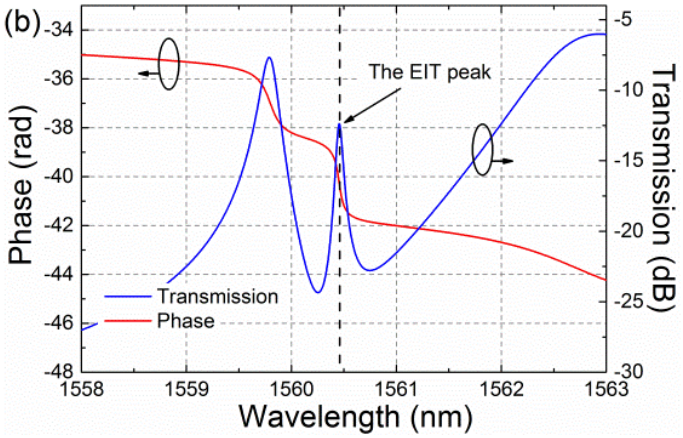
(b)
Phase (rad)
Transmission (dB)
Wavelength (nm)
The EIT peak
Transmission
Phase

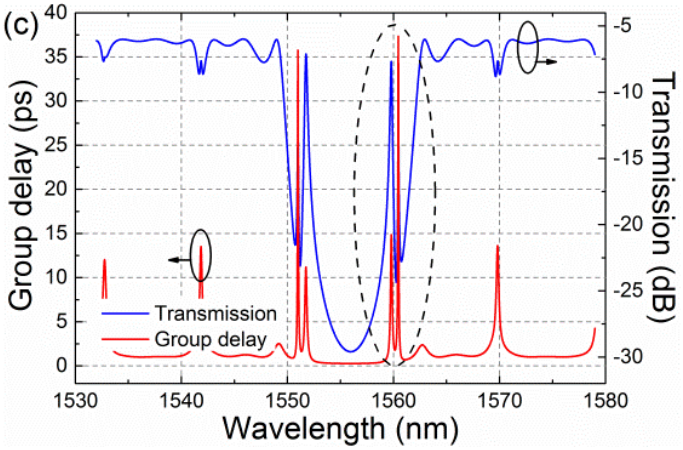
(c)
Group delay (ps)
Transmission (dB)
Wavelength (nm)
Transmission
Group delay

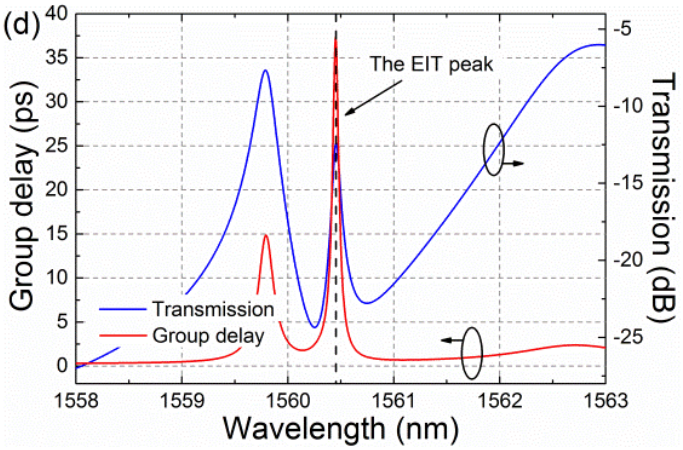
(d)
Group delay (ps)
Transmission (dB)
Wavelength (nm)
The EIT peak
Transmission
Group delay

Fig.4.10 (a) The phase curve and the EIT-like transmission spectrum. (b) The zoomed-in curves of the phase and EIT-like transmission circled by the dashed line. (c) The group delay curve and the EIT-like transmission spectrum. (d) The zoomed-in curves of the group delay curve and the EIT-like transmission circled by the dashed line.

For the EIT system, one of the important properties is the ability to produce slow light. The microring resonator has already been known to be able to generate slow light at the wavelengths of resonance peaks. However, the transmission at these resonance peaks is too low for practical applications. By contrast, the EIT system can generate slow light with a high transmission at the wavelength of the EIT peak. In order to study the properties of slow light, the phase of the transmission can be utilized to calculate the group delay between the input and the output light. In this work, the initial phase of the input light is normalized to 0. In Fig. 4.10(a), the phase of the output light is extracted from the fitted transmission spectrum. The EIT peak region (the dashed circle line) is zoomed in as shown in Fig. 4.10(b). At the wavelength of the EIT peak (the dashed line), there is an abrupt slope change of the phase curve indicating a sudden and drastic change of the phase. With the phase curve, the group delay can be calculated by

$$\tau = \frac{d\varphi}{d\omega} \tag{4.5}$$

where φ is the phase; $\omega = \frac{2\pi c}{\lambda}$ is the angular frequency, in which c is the speed of

light in vacuum and λ is the wavelength. The group delay curve and the transmission spectrum have been plotted in Fig. 4.10(c). The EIT peak region (the dashed circle line) is magnified in Fig. 4.10(d). It can be seen that the group delay peak and the EIT transmission peak match exactly at the same wavelength (the dashed line), which verifies the characteristic of the EIT effect. The EIT effect can offer a group delay with a high transmission transparency. Calculation shows that a slow light with a group delay of 38 ps is obtained. Since the theoretical fitted transmission spectrum is optimized in terms of the measured data, we believe the calculated group delay is able to provide a good prediction on the actual performance. According to the simulation results, if we increase the reflectivity of the Bragg gratings by increasing dw and N, the group delay can be much higher but at the cost of higher IL as discussed above. In addition, by smoothening the surface of waveguides and reducing the round trip loss of the microring to achieve a higher α^2, not only the IL can be reduced but also the group delay can be further improved.

4.3 The Working Principle of Tunable and Convertible EIT/Fano Resonances in APMR-BG System

Fig. 4.11(a) shows the schematic of the APMR-BG coupled-resonator system. Two Bragg gratings are located in the bus waveguide at the two sides of the microring coupling region, which perform as two partially reflective elements to form an F-P resonator. As shown, dw is the depth of the Bragg grating corrugations; R is the radius of the microring; L is the cavity length of the F-P resonator; N is the number

of periods of each Bragg grating; k is the coupling coefficient and k^* is the conjugation; $t = \sqrt{1-|k|^2}$ is the transmission coefficient and t^* is the conjugation; $\alpha^2 = e^{-\delta_r L_r}$ is the round-trip-power-attenuation in which the δ_r is the propagation loss of microring waveguide per unit length and $L_r = 2\pi \times R$ is the cavity length of the microring. Based on the transfer matrix method, this system can be expressed as

$$T_{in} = T_{Bg} \times T_{wg} \times T_{ring} \times T_{wg} \times T_{Bg} \times T_{out} \tag{4.6}$$

where T_{in} and T_{out} are the matrices of the light at the input port and the through port respectively; T_{wg} is the matrix of the waveguide; T_{ring} is the matrix of the microring with taking the reflected light into account; T_{Bg} is the transfer matrix of the Bragg grating. Similarly we regard the Bragg grating as a periodic structure consisting of wide waveguide segments, narrow segments and reflective interfaces [26]. The detailed definitions of relative parameters can be found in chapter 4 or in [28]. The effective indices for the waveguides of different widths and wavelengths are calculated with the BeamPROP module of Rsoft software by taking the dispersion into account.

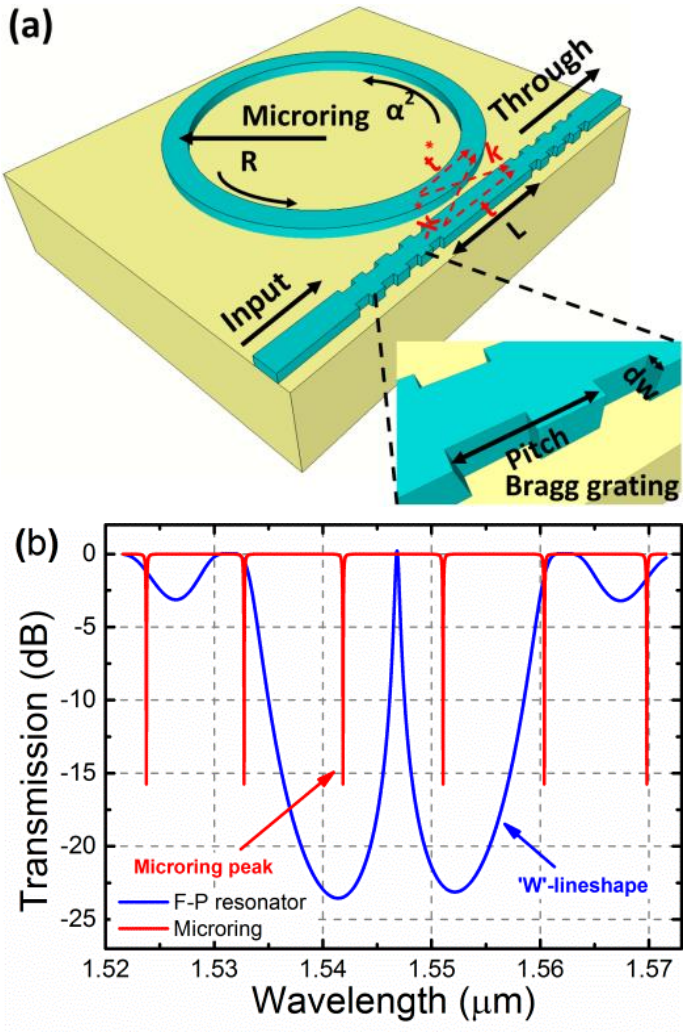

Fig.4.11 The schematic of the APMR-BG coupled-resonator system. (b) The normalized transmission spectra of the F-P resonator and the microring resonator.

As shown in Fig. 4.11(b), when $L=\left(m+\frac{1}{2}\right)\times pitch$ (m is a natural number, $pitch$ is the pitch of Bragg grating), the transmission spectrum of the F-P resonator is in a 'W' lineshape. While the resonance dips of the microring overlap with the 'W' lineshape of the F-P resonator, the resonances are formed in both resonators simultaneously. The coupling between them gives rise to the EIT and Fano transmission as shown in Fig. 4.12(a). In order to set the resonance wavelengths of the F-P resonator at 1.55 μm, we

chose these parameters as an initial design: $pitch$ = 320.5 nm, N = 70, dw = 20 nm, α = 0.9803.

While increasing the gap width between the bus waveguide and the microring resonator, the coupling strength between the F-P resonator and the microring resonator becomes weaker. In consequence, the coupling coefficient k decreases and the transmission coefficient t increases. The region circled by the black dashed line is zoomed-in as shown in Fig. 4.12(b). It can be clearly seen that when $t = 0.7141 < \alpha$, an EIT transmission is generated. With increasing t to 0.8660, the extinction ratio (ER) of the EIT peak drops from 17 dB to 10 dB and the insertion loss (IR) increases from 13 dB to 20 dB. Meanwhile, the dip at the right side of the EIT peak becomes narrower. By increasing the value of t to $t = 0.9803 = \alpha$, the transmission spectrum transforms to a sharp Fano lineshape, and it is noteworthy that the Fano transmission has the largest ER ~ 43 dB at this point. With further increase of t to $t = 0.9950 > \alpha$, the transmission spectrum keeps the Fano lineshape, but the extinction ratio (ER) of Fano transmission dramatically decreases from 43 dB to 7 dB and the required wavelength shift $\Delta\lambda$ between the dip and the peak decreases from 0.15 nm to 0.11 nm.

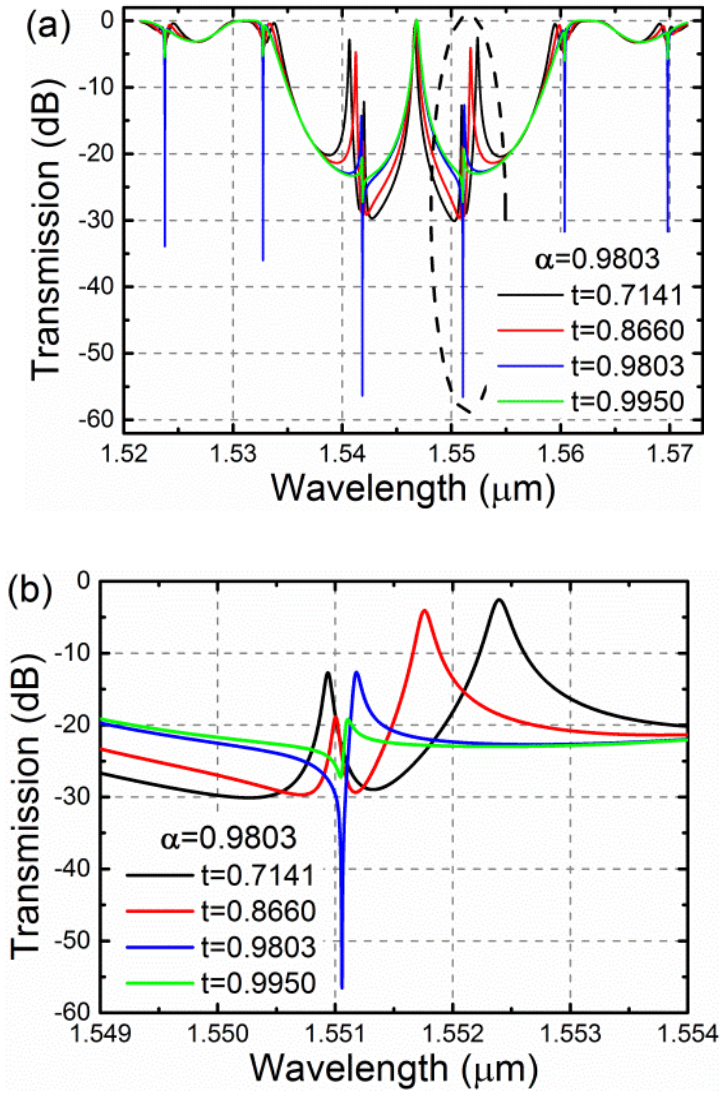

Fig.4.12 (a) The EIT and Fano transmission spectra of different t under pitch = 320.5 nm, N = 70, dw = 20 nm, α = 0.9803. (b) The zoomed-in spectra of the EIT and Fano transmission spectra circled by the black dashed line.

We consider that it is the abrupt π phase shift of the transmission of the microring resonator under the critical coupling condition ($t = \alpha$) [29] which leads to the transformation of the lineshape. The transmission of the APMR-BG coupled-resonator system (blue solid line) and the corresponding phase of the microring resonator (red dashed line) have been plotted in Fig. 4.13. As shown in Fig. 4.13(a), when

$t = 0.7141$, the phase curve of the microring resonator becomes steeper at the wavelength of the EIT peak (marked with black dashed line). When we increased the gap width until $t = 0.8660$, as it can be seen in Fig. 4.13(b), the gradient of the phase at the wavelength of the EIT peak becomes larger than $t = 0.7141$. For these two scenarios, no abrupt phase shift happens, which means the coupling between two resonators keeps constructive and the transmission maintains as the EIT lineshape. When $t = 0.9803 = \alpha$ (critical coupling), it is noteworthy that an abrupt π phase shift of the light in the microring resonator occurs at the same wavelength of the Fano lineshape as plotted in Fig. 4.13(c). This abrupt π phase shift contributes to the transformation from constructive interference (EIT transmission) to destructive interference (Fano transmission). The opposite phases of these two light paths lead to the completely destructive interference and gives rise to the extremely low transmission at the dip of Fano lineshape as well as the largest ER. In addition, as shown in Fig. 4.13(d), if t is further increased to 0.9950, the phase shift maintains but the shifting value is smaller than π. This smaller phase shift results in a partially counteraction of the light between the microring resonator and the F-P resonator, corresponding to the smaller ER (~7 dB) of the Fano lineshape. In summary, for the over-coupling ($t < \alpha$) and the under-coupling ($t > \alpha$) regime of the microring resonator, the phase shift is continuous but in opposite direction [30], which leads to the continuous change of the EIT and Fano transmissions respectively. The critical coupling regime ($t = \alpha$) is the threshold point for the conversion between the EIT and

Fano transmissions.

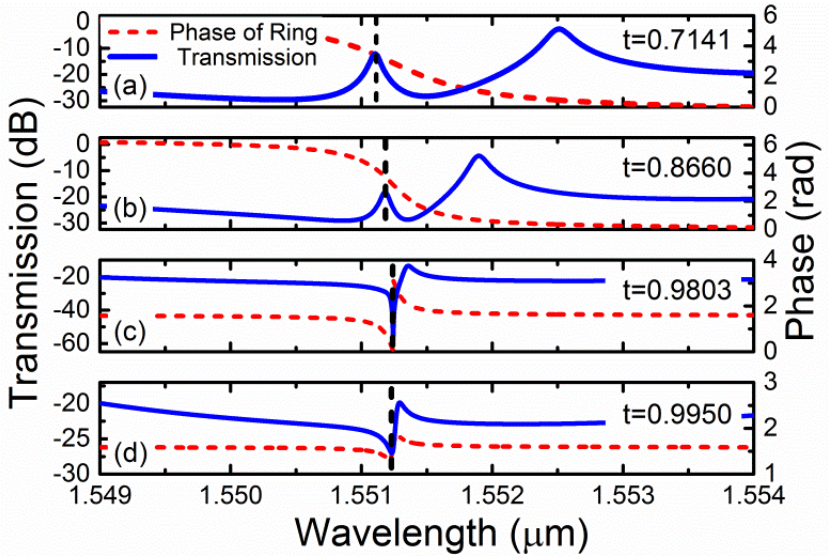

Fig.4.13 (a) The normalized transmission spectra and the phase of microring when t = 0.7141. (b) The normalized transmission spectra and the phase of microring when t = 0.8660. (c) The normalized transmission spectra and the phase of microring when t = 0.9803. (d) The normalized transmission spectra and the phase of microring when t = 0.9950. (Fig. (a) – (d) are under conditions: pitch = 320.5 nm, N = 70, dw = 20 nm, α = 0.9803.)

The APMR-BG coupled-resonator systems of different gap widths were fabricated on a SOI wafer with a 220 nm-thick top silicon layer and a 2 μm-thick buried oxide (BOX) layer. Both the grating layer and waveguide layer were patterned with electron beam lithography (EBL). The grating layer was etched to the depth of 70 nm with reactive ion etching (RIE). The waveguide layer was etched down to the BOX layer with deep reactive ion etching (DRIE) in order to have straight and smooth sidewalls. After removing the photoresist, the sample was coated with a cladding layer of 1 μm

SiO2 using plasma enhanced chemical vapor deposition (PECVD) system. The radius of the microring and the width of the strip waveguides are designed to be 10 μm and 500 nm respectively. The $pitch$ and dw are fixed at 320 nm and 20 nm respectively. The duty cycle is 50%. The N of each Bragg grating is 100. The L of 3.36 μm is chosen which was equal to 10.5 times of the pitch. The gap width between the bus waveguide and the microring is swept from 60 nm to 300 nm. Fig. 4.14(a) and Fig. 4.14(b) show the SEM images of the fabricated APMG-BG system. As shown in Fig. 4.15(a), when the width of the gap is 110 nm ($t < \alpha$), the coupling between the two resonators is strong and the EIT transmission is generated. For the EIT transmission circled by the black dashed lines, the full-width-at-half-maximum (FWHM) is measured as 0.155 nm, which corresponds to the quality factor (Q factor) of 10020. Based on the theoretical fitting data, the Q factor of the fabricated loaded microring is 2160. The Q factor of the F-P resonator formed by Bragg gratings is 1100. The ER is about 8.5 dB. The fitting parameters are: $pitch$ = 318.85 nm, N = 100, dw = 8.5 nm, R = 10.4 μm, k = 0.6i, t = 0.8, α = 0.9799. With the fitting parameters, the corresponding phase of the microring resonator has been plotted with the zoomed-in EIT transmission spectrum in Fig. 4.15(c), which is consistent with the scenarios in Fig. 4.13(a) and Fig. 4.13(b). As shown in Fig. 4.15(b), when the width of the gap is 170 nm ($t \geq \alpha$), a sharp asymmetric Fano transmission is generated. It is noteworthy that the ER of the Fano transmission is as large as 26 dB. The fitting parameters are: $pitch$ = 320.35 nm, N = 100, dw = 8 nm, R = 10.199 μm, k = 0.208i, t = 0.9781,

α = 0.9745. As seen, in this device, t is very close to α, which means the coupling status is close to the critical coupling status. So a large ER of 26 dB can be obtained, which agrees well with the simulation result shown in Fig. 4.13(c). As shown in Fig. 4.15(d), the corresponding phase of the microring resonator has an abrupt shift at the wavelength of the Fano lineshape (marked with blacked dashed line), which is consistent with the simulation results shown in Fig. 4.13(c) and Fig. 4.13(d). It can be clearly seen that the experimental results and the simulation results are in a good agreement. The difference between the designed (20 nm) and the fitted dw (8 and 8.5 nm) is because the fabricated Bragg grating corrugations are not in the desired rectangular shape. The actual fabricated Bragg gratings are comparable with an ideal rectangular Bragg grating with $dw = 8$ nm and 8.5 nm. So we utilize more periods (N = 100) of Bragg grating to increase the reflectivity and compensate the influence of the smaller actual corrugation depth. The small ripples are due to the weak optical reflection at the input and output facets. The active tuning of the coupling coefficient k can be realized by utilizing MEMS method to change the gap between the bus waveguide and the microring (need to remove the oxide cladding layer) [31-33]. Besides, tuning the round-trip-power-attenuation α^2 can be achieved by adding an MZI-assisted structure with a thermal heater [34,35].

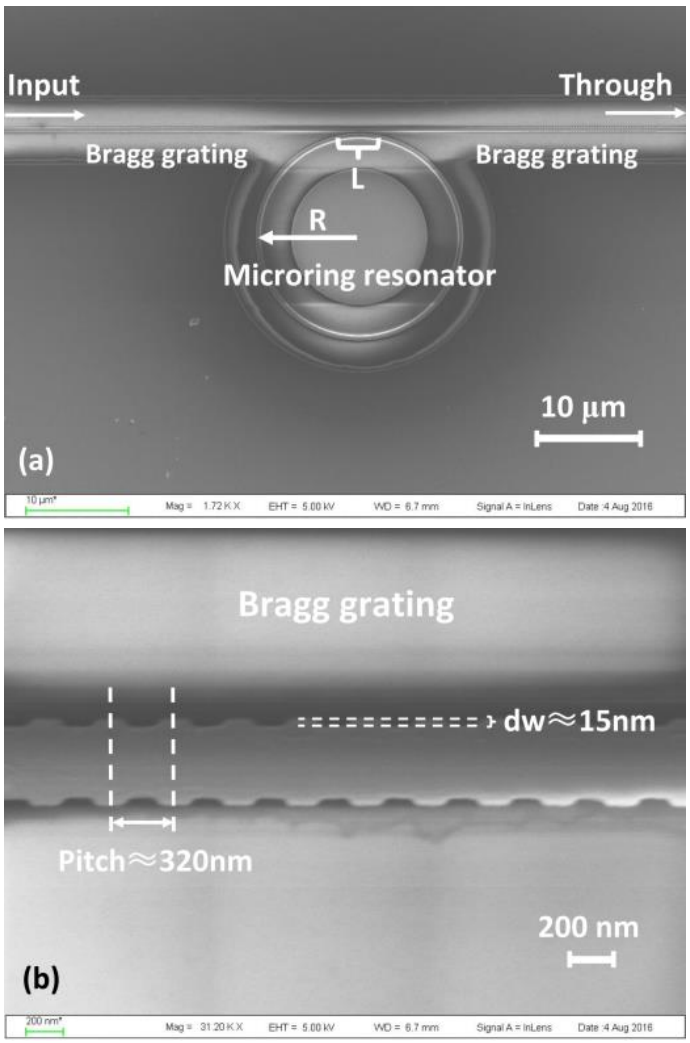

Fig.4.14 (a) The SEM image of the APMR-BG coupled-resonator system. (b) The zoomed-in SEM image of the Bragg grating.

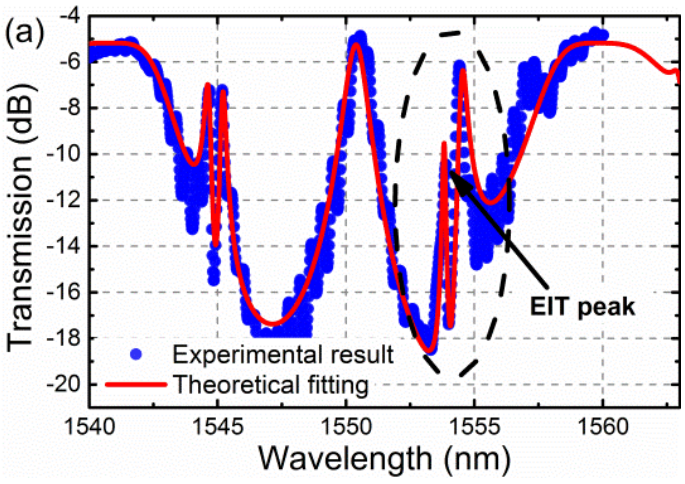

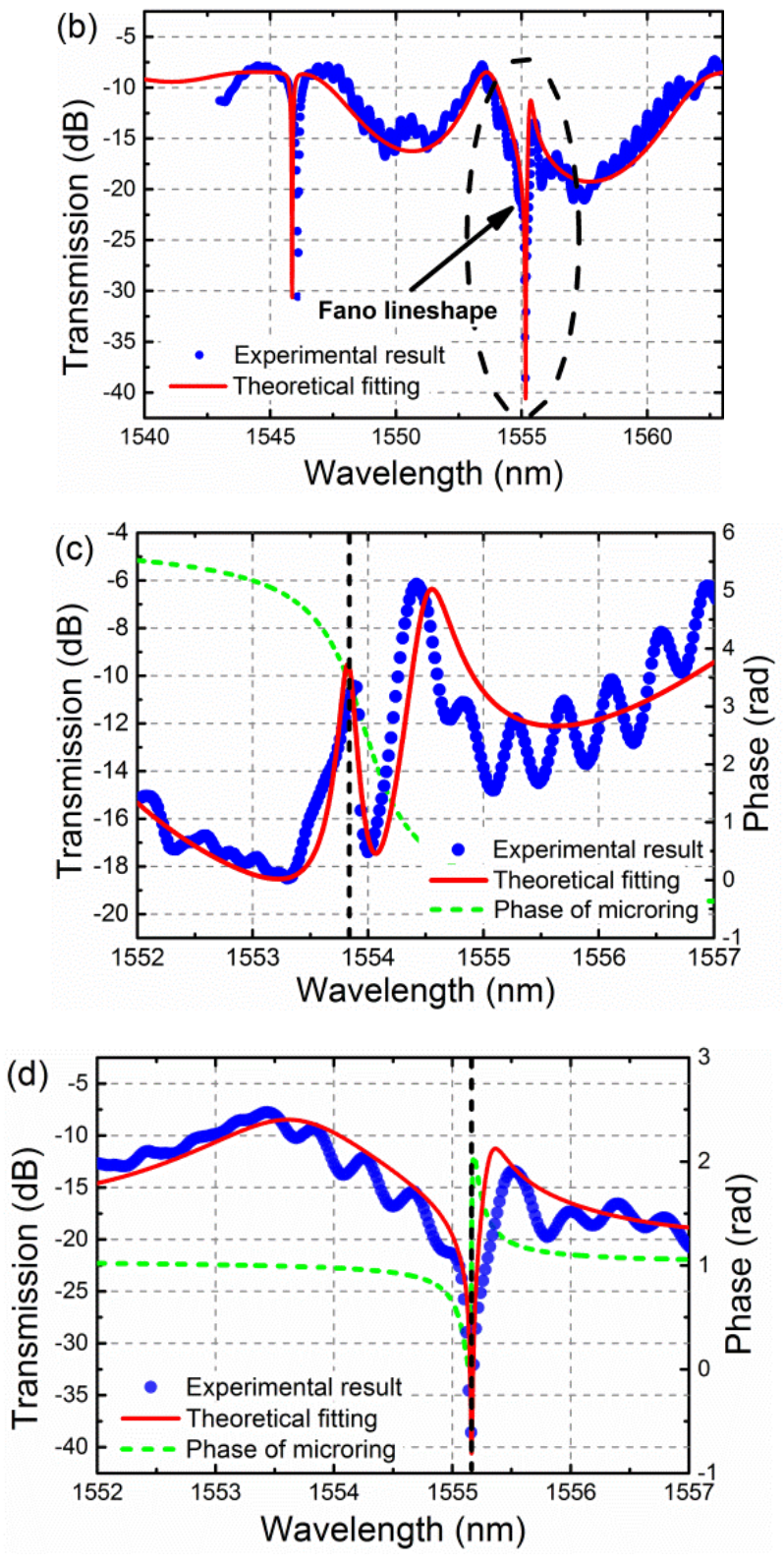

Fig.4.15 (a) The measured EIT transmission spectrum when the gap width is 110 nm. (b) The measured Fano transmission spectrum when the gap width is 170 nm. (c) The zoomed-in EIT transmission spectrum and the corresponding phase of the microring

resonator. (d) The zoomed-in Fano transmission spectrum and the corresponding phase of the microring resonator.

4.4 Thermally tunable Fano and EIT resonances in MZI-assisted Microring-Bragg Grating Based Coupling Resonant System

The schematic of the MZI-assisted Bragg grating-microring coupled resonant system is shown in Fig. 4.16(a). Two Bragg gratings are located in the input-through bus waveguide at the two sides of the coupling region acting as two partially reflective elements to form a Fabry-Perot (F-P) resonator. In this work, the coupling between the resonances of the microring and the F-P resonator gives rise to the various EIT and Fano resonances. The two coupling points between the MZI arm and the microring are set at the two sides of the microring as shown in Fig. 4.16(a). L_{MZI_s} and R_{MZI} are the length of the straight section and the bending radius of the MZI arm respectively. The length of the MZI arm is defined as the total length between these two coupling points, which can be expressed as $L_{MZI} = 2 \cdot L_{MZI\_s} + \pi \cdot R_{MZI}$. The power attenuation coefficient and the phase shift of the MZI arm are $\alpha_{MZI}{}^2$ and θ_{MZI} respectively. Correspondingly, $\alpha_{hr}{}^2$ and θ_{hr} are the power attenuation coefficient and the phase shift of the half microring between the two coupling points. α^2 and R are the round-trip power attenuation coefficient and the radius of the microring resonator respectively. $t = \sqrt{1-|k|^2}$ is the transmission coefficient of the coupling region between the input-through bus waveguide and the microring, and t^* is the conjugation. k is

the coupling coefficient of the coupling region between the input-through bus waveguide and the microring, and k^* is the conjugation. k' is the coupling coefficient of the two coupling points between the MZI arm and the microring. $pitch$ is the pitch of the Bragg gratings. dw is the depth of the corrugation. L_{cv} is the length of the F-P cavity, and N is the number of the periods of the Bragg gratings.

Based on the transfer matrix method, the transmission of the whole system can be expressed as [26]:

$$T_{input} = T_{Brag} \times T_{WG} \times T_{R\_eqv} \times T_{WG} \times T_{Brag} \times T_{output} \tag{4.7}$$

where the inverse expression is adopted; T_{Brag} is the matrix of the Bragg gratings; T_{WG} is the matrix of the straight waveguide; and T_{R_eqv} is the matrix of the equivalent microring resonator, which will be explained later. More detailed information can be found in [28].

In order to simplify the discussion, an add-drop bus waveguide with an effective coupling coefficient k_{eff} can be utilized to equivalently replace the MZI arm, where k_{eff} can be calculated by [34, 35]:

$$k_{eff}{}^2 = k'^2(1-k'^2)\cdot(\alpha_{MZI}{}^2 + \alpha_{hr}{}^2 - 2\alpha_{MZI}\alpha_{hr}\cos(\theta_{MZI} - \theta_{hr})) \tag{4.8}$$

while the relative phase $\Delta\theta = \theta_{MZI} - \theta_{hr}$ is changed from 0 to π, $k_{eff}{}^2$ can be tuned from 0 to $4k'^2(1-k'^2)$. Furthermore, as shown in Fig. 4.16(b), by considering the equivalent add-drop bus waveguide and the microring as a single microring, the system can be further simplified as an all-pass microring coupled with an F-P resonator. The

effective round-trip power attenuation of this equivalent single microring can be expressed as $\alpha_{\text{eff}}{}^2 = \alpha^2 - k_{eff}{}^2$. So, $\alpha_{\text{eff}}{}^2$ can be tuned by changing $\Delta\theta$, which can be realized by changing the optical path length of the MZI arm by means of thermo-optical, electro-optical, or all-optical effects. In this experiment, the changing of the optical path length of the MZI arm is achieved by thermo-optical effect. Via tuning $\alpha_{\text{eff}}{}^2$, the coupling status between the microring and the F-P resonator can be changed as well as the resonance lineshape. When $\alpha_{\text{eff}} > t$, the microring resonator operates in the over-coupling regime. The phase curve of the microring resonator is continuous and the coupling between the microring resonator and the F-P resonator is constructive, which results in the EIT peak. However, when $\alpha_{\text{eff}} = t$, the microring resonator operates at the critical-coupling point. An abrupt π shift of the microring phase curve occurs [29], and the coupling between the two resonators turns to completely destructive, which generates a sharp Fano lineshape with the highest extinction ratio (ER). When $\alpha_{\text{eff}} < t$, the microring resonator operates in the under-coupling regime. The phase shifting is maintained but with smaller values. The two light paths of the two resonators undergo partially destructive interference, which results in Fano lineshapes with smaller ERs. More detailed discussions can be referred in [36].

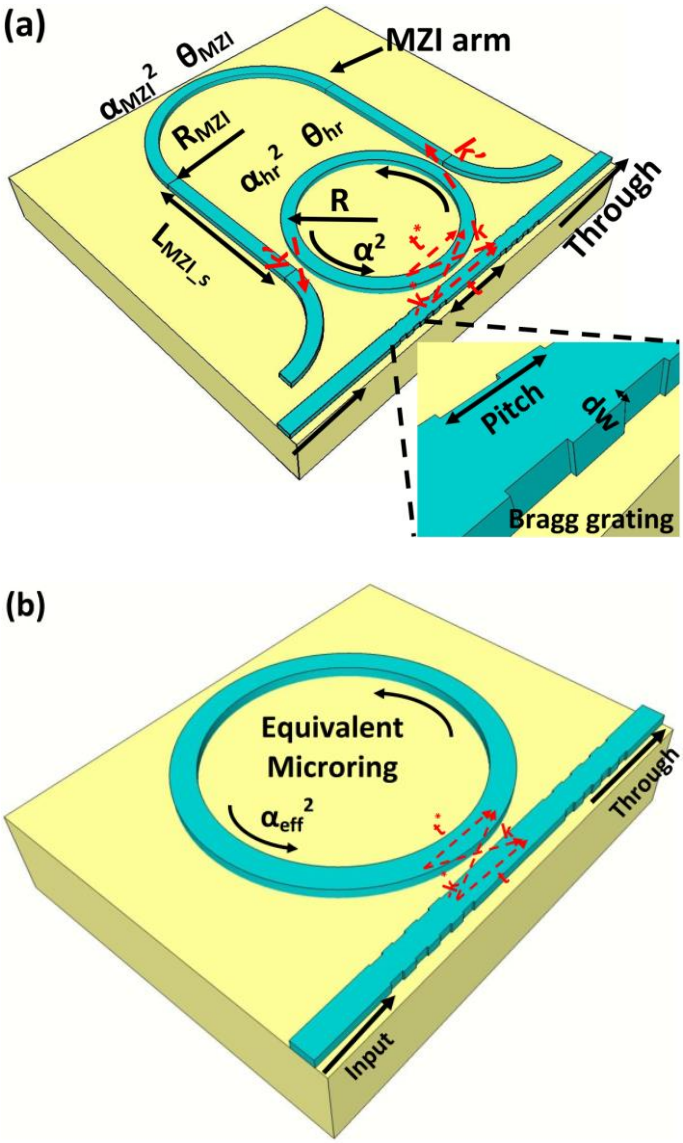

Fig.4.16 (a) The schematic of the MZI-assisted Bragg grating-microring coupled resonant system. (b) The equivalent model of the MZI-assisted Bragg grating-microring coupled resonant system.

The simulations are conducted on a 220 nm-top-silicon-layer SOI platform with 2 μm buried oxide (BOX) layer, based on the transfer matrix method. For an initial design, we chose the parameters as $pitch$ = 315 nm, N = 100, dw = 10 nm, R = 10 μm, R_{MZI} = 10.715 μm (the gap widths between the MZI arm and the microring are set as 115 nm), $k' = 0.4i$, $k = 0.45i$, $t = 0.8930$, $L_{cv} = 10.5 \cdot pitch$. Since the simulations are conducted

in a narrow band, the dispersion of the group index can be ignored and the value of the group index is set as 4.067. As shown in Fig. 4.17(a), the curve of α_{eff} is periodical. By heating up the MZI arm, the curve of α_{eff} is blue-shifted, which is consistent with [34]. $\Delta\varphi$ is the additional phase difference between the MZI arm and the half microring caused by the increased temperature of the MZI arm. The value of t is marked out with a horizontal black long-dashed line as 0.8930. When the curve of α_{eff} is blue-shifted, the value of α_{eff} at the wavelength of the Fano dip or EIT peak changes as well as the coupling status between the two resonators. The transmission spectra under different $\Delta\varphi$ are shown in Fig. 4.17(b). A magnified image of the black dashed-line circled region is presented in Fig. 4.17(c). As seen, when the MZI arm is at room temperature (red line), α_{eff} is much larger than t hence an EIT resonance is generated. While we heat up the MZI arm to increase $\Delta\varphi$ from 0 to 0.257π (blue line), the ER of the EIT peak drops from 16.1 dB to 4.63 dB, and the insertion loss (IL) increases from 3.5 dB to 16.4 dB. At the same time, the full-width-at-half-maximum (FWHM) of the EIT peak becomes smaller from ~ 0.03 nm to ~ 0.213 nm, which corresponds to the decrease of the quality factor (Q factor) from ~ 51200 to ~ 7200. So while $\alpha_{\text{eff}} > t$ and with the decreasing difference between α_{eff} and t, the ER, the IL and the sharpness of the EIT peak are all degraded. When the temperature of the MZI arm is increased until $\Delta\varphi=0.456\pi$, α_{eff} is equal to t and critical coupling occurs, which acts as a threshold point between Fano and EIT lineshapes. At that point, the transmission spectrum is converted from EIT lineshape to Fano lineshape. It

is also noteworthy that the Fano resonance obtains the largest ER of 55 dB at the same time. When we continue raising the temperature of the MZI arm until $\Delta\varphi=0.706\pi$, the Fano resonance lineshape remains but the ER significantly decreases to only 7.8 dB. Besides, the required wavelength shifting between the dip and the peak of the Fano lineshape also increases from ~ 0.405 nm to ~ 0.59 nm. So while $\alpha_{\text{eff}} \le t$ and with the increasing difference between t and α_{eff}, not only the ER of the Fano resonance drops but also the sharpness degrades.

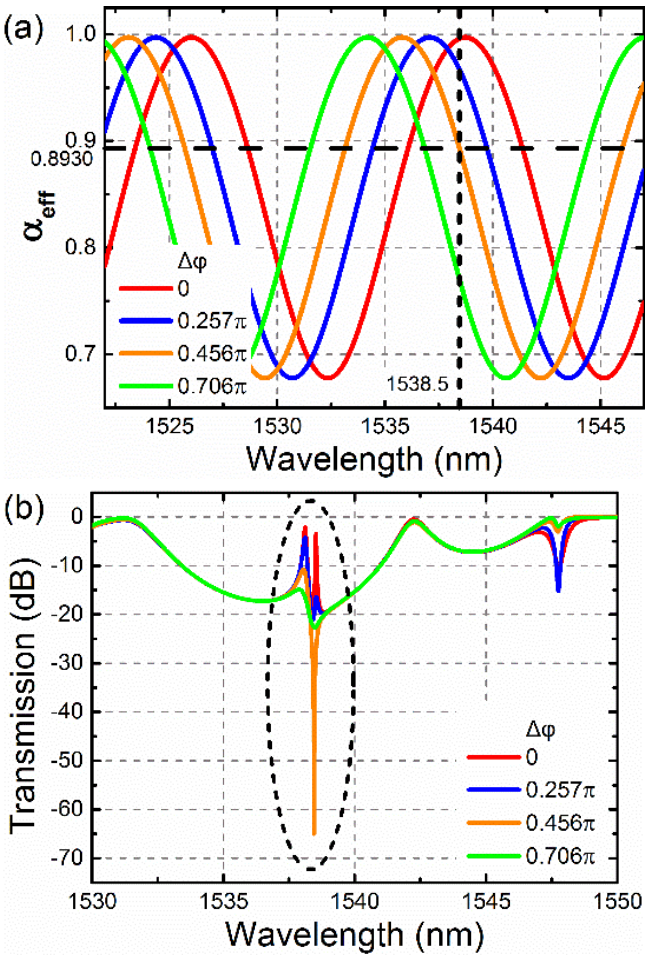

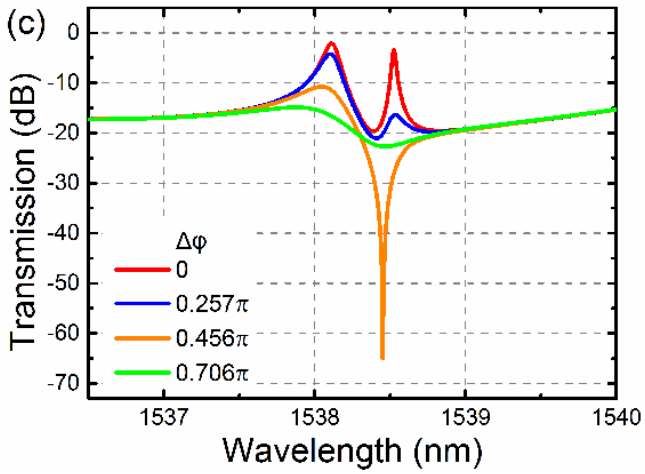

Fig.4.17 (a) The curves of α_{eff} versus wavelength under different $\Delta\varphi$ when $t = 0.8930$. (b) The transmission spectra under different $\Delta\varphi$ when $t = 0.8930$. (c) The magnified spectra of the transmissions circled by the black dashed line in Fig. 4.17(b).

The fabricated device is shown in Fig. 4.18. The grating layer and the waveguide layer were both patterned with electron beam lithography (EBL). The grating layer was etched down to a depth of 70 nm with reactive ion etching (RIE). The waveguide layer was etched down to the BOX layer with deep reactive ion etching (DRIE). Then the sample was coated with a cladding layer of 1 μm SiO_2. A layer of 110 nm Ti was deposited and partially lifted off on the SiO_2 cladding to form the heating wires. Then a 20 nm Ti layer and a 300 nm Au layer were deposited and partially lifted off in sequence to form the conducting wires and the electrode pads. The designed parameters were: $pitch$ = 315 nm, N = 100, dw = 15 nm, R = 10 μm, R_{MZI} = 10.715 μm, $L_{cv} = 10.5 \cdot pitch$. The gap widths between the MZI arm and the microring were set as 115 nm. The gap width between the input-through bus waveguide and the

microring was 85 nm. The width of waveguide was 500 nm. L_{MZI_s} was 21.5 μm. The width of the Ti heating wires was 1.5 μm.

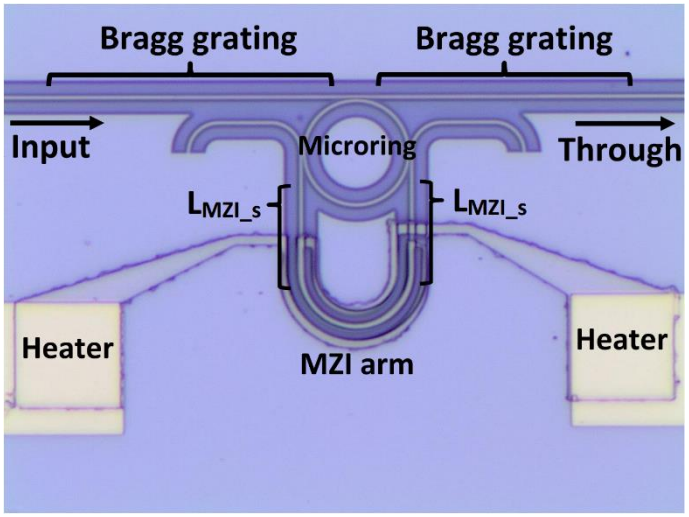

Fig.4.18 The fabricated thermal-optic switch between Fano and EIT resonances based on a MZI-assisted Bragg grating-microring coupled system.

The experimental results under a series of bias voltages of 0 V, 4 V and 8 V are shown in Fig. 4.19(a). It can be clearly seen that while the bias voltage increases from 0 V to 8 V, the transmission spectrum gradually converts from EIT lineshape to Fano lineshape. In Fig. 4.19(b), 4.19(c), 4.19(d), the experimental results of the bias voltage of 0V, 4V and 8V are fitted with our numerical model respectively and the corresponding curves of α_{eff} are also plotted. As seen, all the experimental results and the simulation results are in good agreement. Because the widths of the gaps are kept constant, the values of k and k' are fitted and fixed as 0.45i and 0.4i respectively in all these devices. Besides, in all the fittings, N, dw, R_{MZI} and $pitch$ are kept constant and fitted as 100, 9.5 nm, 10.715 μm and 314.4 nm respectively. The difference between the designed value (15 nm) and fitted value (9.5 nm) of dw is because the

fabricated corrugations of the Bragg grating are not in ideal rectangular shape. The fabricated Bragg gratings are comparable with the ideal rectangular Bragg grating with a corrugation depth of 9.5 nm. The value of t is marked as 0.8930 with horizontal black long-dashed lines and the wavelengths of the EIT peak or the Fano dip are marked with vertical black short-dashed lines. While the bias voltage increases from 0 V to 4V, $\Delta\varphi$ increases from 0 to 0.077π and α_{eff} decreases from 0.9846 to 0.9654. In the meantime, the EIT resonance lineshape maintains but the ER of the EIT peak drops more than a half from 8.73 dB to 3.6 dB and the FWHM increases from ~ 0.07 nm to ~ 0.25 nm (corresponding to the decrease of Q factor from ~ 21900 to ~ 6150). Both the ER and the sharpness are degraded, which are in good agreement with the above simulations. Next, with the increase of bias voltage to 8 V, $\Delta\varphi$ increases from 0.077π to 0.308π as expected and α_{eff} drops from 0.9654 to 0.8716. As a result, the Fano transmission is generated. As measured, the ER is 27.4 dB and the required wavelength shifting between the dip and the peak is 0.557 nm. The small ripples of the curves are probably due to the weak optical reflection at the input and output facets. Besides, it is noteworthy that the wavelength of the EIT peak or the Fano dip is slightly red-shifted while the bias voltage increases. It is because the distance between the Ti heating wire and the microring waveguide is not large enough and the microring waveguide is also heated up by the heater, which results in the red-shifting of the microring resonance peak. The thermal isolation can be improved by etching deep trenches between the microring and the MZI arm. Alternatively, by employing

the phase-changing materials, such as VO_2 and $Ge_2Sb_2Te_5$ [37, 38], to realize the additional phase difference $\Delta\varphi$, the influence on the performance and the lifetime of the device from the thermal heating wires can be avoided. Furthermore, the Bragg grating can be replaced by a Sagnac-loop mirror (SLM) [39] or an offset in the bus waveguide [40] for obtaining a broader operation bandwidth and ease the controlling of fabrication process. However, compared with the SLM, the Bragg grating is much more compact and suitable for high density integration. And the advantage of the Bragg grating over the offset in the bus waveguide is that, the transmission spectrum can be flexibly and conveniently tuned by changing parameters of the Bragg grating. So these three kinds of partially reflective elements can be utilized for the applications with different requirements.

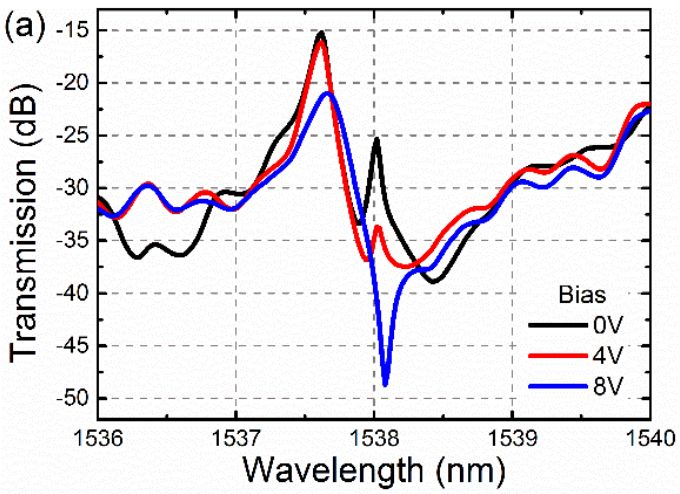

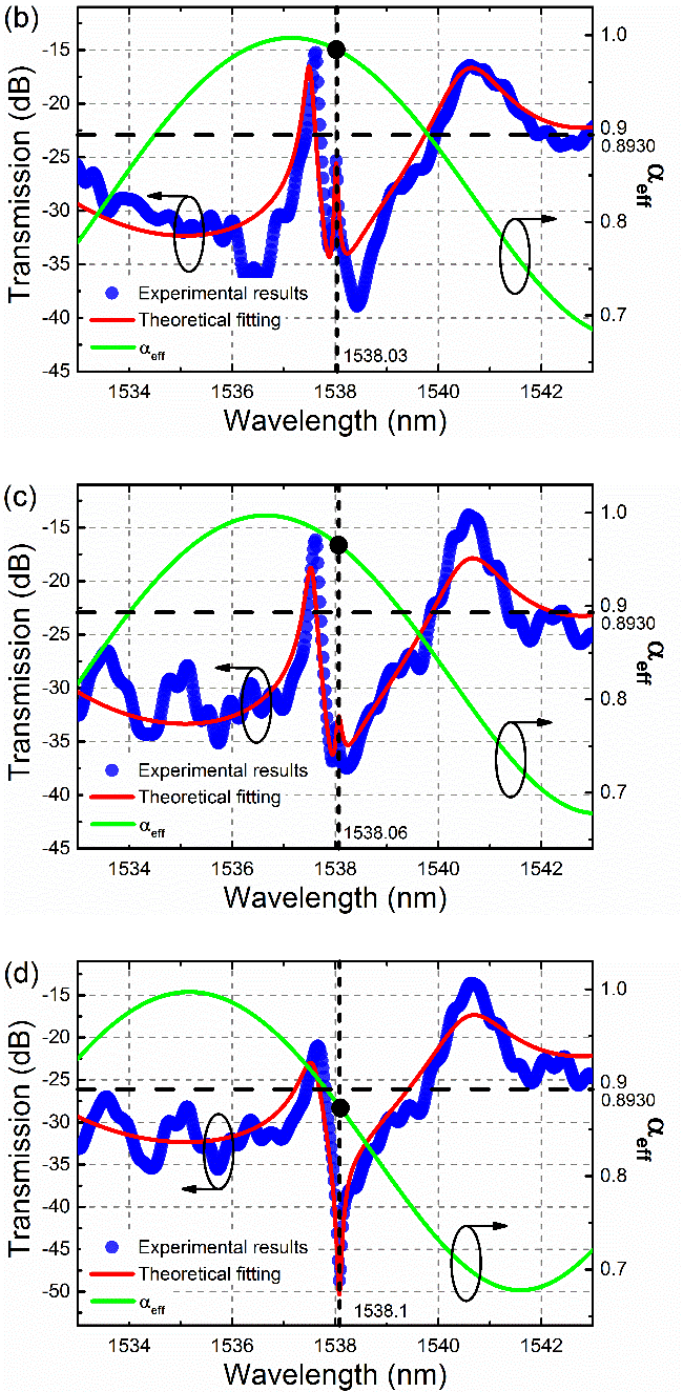

Fig.4.19 (a) The experimental transmission spectra when the bias voltage is 0 V, 4 V and 8 V. (b) The fitted transmission spectrum when the bias voltage is 0 V and the corresponding curve of α_{eff} . (c) The fitted transmission spectrum when the bias voltage is 4 V and the corresponding curve of α_{eff} . (d) The fitted transmission spectrum when the bias voltage is 8 V and the corresponding curve of α_{eff}

4.5 Conclusion and Discussions

In this chapter, an EIT-like spectrum is demonstrated theoretically and experimentally in an APMR-BG based coupling resonant system. The EIT-like spectrum originates from the coupling between two resonators namely the F-P resonator which is formed by two sections of Bragg gratings and the microring resonator. The influence of five main dimensional parameters have been investigated, including the pitch of Bragg grating, the number of Bragg grating periods (N) and the depth of Bragg grating corrugation (dw), the coupling coefficient (k) and the round-trip-power-attenuation (α^2). The EIT-like spectrum is experimentally observed in a compact and fully integrated APMR-BG based coupling resonant system on a SOI wafer. The FWHM is 0.077 nm corresponding to a Q factor of 20200. The IL and the ER are 7.5 dB and 12 dB respectively. The experimental result fits well with the numerical model. Based on the fitted transmission curve, the phase and the group delay have been studied. The slow light with the group delay of 38 ps is obtained at the wavelength of the EIT peak. Based on the APMR-BG system, we demonstrate the conversion between the EIT and the Fano transmission and the operating mechanism. The transformation of the transmission lineshape is achieved by tuning the coupling strength between the F-P resonator and the microring resonator as an abrupt π phase shift of the light in the microring resonator occurs and leads to the transformation from the constructive interference to the destructive interference between the two resonators. For the over-coupling ($t < \alpha$) and the under-coupling ($t > \alpha$) status of the microring resonator, the

phase shift is continuous but in opposite direction, which leads to the continuous changing of the EIT transmission and the Fano transmission respectively. The experimental results are well fitted with the specially developed numerical model. This system has the advantage of a small footprint and the fabrication process is compatible with the planar waveguide fabrication process. In this last part of this chapter, thermally tunable Fano and EIT resonances is theoretically and experimentally demonstrated based on a MZI-assisted Bragg grating-microring coupled resonant system. In this work, the coupling between the MZI-assisted microring resonator and the F-P resonator gives rise to the EIT and Fano resonances. By changing the optical path length of the MZI arm, the resonant status of the MZI-assisted microring can be tuned as well as the resonance lineshape. The performance of the system is theoretically calculated and analyzed with a specially developed numerical model. Active tuning with thermo-optical effect is experimentally verified to be able to achieve the conversion of the resonance lineshape. The experimental and simulation results are in good agreement. With the capability of on-chip tuning and converting the resonance between Fano and EIT lineshapes, great improvements in the versatility, flexibility and compatibility of the system as well as the possibility of high volume monolithic integration become possible. As a result, it is envisaged that more related potential applications in communication, biochemical sensing and on-chip signal processing can be realized. Furthermore, even though in this chapter, the EIT/Fano devices are demonstrated operating at 1.55 μm wavelength, the idea and

concept can be easily extended to MIR band, which only needs to fine tune the dimensional parameters, such as the pitch and corrugation depth of Bragg grating and the width of waveguides.

References

[1] K. J. Boller, A. Imamoğlu, and S. E. Harris, “Observation of electromagnetically induced transparency,” *Phys. Rev. Lett.*, vol. 66, pp. 2593, 1991.

[2] Q. Z. Huang, Z. Shu, G. Song, J. G. Chen, J. S. Xia, and J. Z. Yu, “Electromagnetically induced transparency-like effect in a two-bus waveguides coupled microdisk resonator,” *Opt. Express*, vol. 22, no. 3, pp. 3219–3227, 2014.

[3] Novikova, R. L. Walsworth, and Y. Xiao, “Electromagnetically induced transparency-based slow and stored light in warm atoms,” *Laser Photon. Rev.*, vol. 6, no. 3, pp. 333–353, 2012.

[4] S. Emelett and R. Soref, “Synthesis of dual-microring-resonator cross-connect filters,” *Opt. Express*, vol. 13, no. 12, pp. 4439-4456, 2005.

[5] Q. Li, Z. Zhang, F. Liu, M. Qiu, and Y. Su, “Dense wavelength conversion and multicasting in a resonance-split silicon microring,” *Appl. Phys. Lett.*, vol. 93, no. 8, pp. 081113, 2008.

[6] R. G. Beausoleil, W. J. Munro, D. A. Rodrigues, and T. P. Spiller, “Applications of electromagnetically induced transparency to quantum information processing,” *J. Mod. Opt.*, vol. 51, no. 16–18, pp. 2441–2448, 2004.

[7] Y. F. Xiao, V. Gaddam, and L. Yang, “Coupled optical microcavities: an enhanced refractometric sensing configuration,” *Opt. Express*, vol.16, no. 17, pp. 12538 2008.

[8] Q. Z. Huang, X. L. Zhang, J. S. Xia and Y. J. Zhong, “Dual-band optical filter based on a single microdisk resonator,” *Opt. Lett.*, vol. 36, no. 23, pp. 4494-4496, 2011.

[9] Q. Z. Huang, J. G. Chen, G. Song, K. Jie, Z. Z. Wang, Y. Wang, J. S. Xia, and J. Z. Yu, “Experimental demonstration of a microdisk resonator filter/buffer utilizing two-mode interference,” *Opt. Lett.*, vol. 39, no. 23, pp. 6553-6556, 2014.

[10] T. Hu, W. J. Wang, C. Qiu, P. Yu, H. Y. Qiu, Y. Zhao, X. Q. Jiang and J. Y. Yang, “Thermally tunable filters based on third-order microring resonators for WDM applications,” *Photon. Tech. Lett.*, vol. 24, no. 6, pp. 524-526, 2012.

[11] F. Y. Gardes, A. Brimont, P. Sanchis, G. Rasigade, D. Marris-Morini, L. O'Faolain, F. Dong, J. M. Fedeli, P. Dumon, L. Vivien, T. F. Krauss, G. T. Reed, and J. Martí, “High-speed modulation of a compact silicon ring resonator based on a reverse-biased pn diode,” *Opt. Express*, vol. 17, no. 24, pp. 21986–21991, 2009.

[12] C. Ciminelli, F. Dell’ Olio, D. Conteduca, C. M. Campanella and M. N. Armenise, “High performance SOI microring resonator for biochemical sensing,” *Opt. & Laser Tech.*, vol. 59, pp. 60-67, 2014.

[13] Q. Xu, S. Sandhu, M. L. Povinelli, J. Shakya, S. Fan, and M. Lipson,

"Experimental Realization of an On-Chip All-Optical Analogue to Electromagnetically Induced Transparency," *Phys. Rev. Lett.*, vol. 96, no. 12, pp. 123901, 2006.

[14] Q. Xu, P. Dong, and M. Lipson, "Breaking the delay-bandwidth limit in a photonic structure," *Nat. Phys.*, vol. 3, no. 6, pp. 406–410, 2007.

[15] Y. Zhang, S. Darmawan, L. Y. M. Tobing, T. Mei, and D. H. Zhang, "Coupled resonator-induced transparency in ring-bus-ring Mach–Zehnder interferometer," *J. Opt. Soc. Am. B*, vol. 28, no. 1, pp. 28-36, 2011.

[16] S. Darmawan, L. Y. M. Tobing, and D. H. Zhang, "Experimental demonstration of coupled-resonator-induced transparency in silicon-on-insulator based ring-bus-ring geometry," *Opt. Express*, vol. 19, no. 18, pp. 17813–17819, 2011.

[17] C. Zheng, X. Jiang, S. Hua, L. Chang, G. Li, H. Fan, and M. Xiao, "Controllable optical analog to electromagnetically induced transparency in coupled high-Q microtoroid cavities," *Opt. Express*, vol. 20, no. 16, pp. 18319–18325, 2012.

[18] K. Totsuka, N. Kobayashi, and M. Tomita, "Slow light in coupled-resonator-induced transparency," *Phys. Rev. Lett.*, vol. 98, no. 21, pp. 213904, 2007.

[19] B. Li, Y. Xiao, C. Zou, Y. Liu, X. Jiang, Y. Chen, Y. Li, and Q. Gong, "Experimental observation of Fano resonance in a single whispering-gallery microresonator," *Appl. Phys. Lett.*, vol. 98, pp. 021116, 2011.

[20] B. Li, Y. Xiao, C. Zou, X. Jiang, Y. Liu, F. Sun, Y. Li, and Q. Gong, "Experimental controlling of Fano resonance in indirectly coupled whispering-gallery microresonators," *Appl. Phys. Lett.*, vol. 100, pp. 021108, 2012.

[21] P. Yu, T. Hu, H. Qiu, F. Ge, H. Yu, X. Jiang, and J. Yang, "Fano resonances in ultracompact waveguide Fabry-Perot resonator side-coupled lossy nanobeam cavities," *Appl. Phys. Lett.*, vol. 103, pp. 091104, 2013.

[22] Y. Xiao, L. He, J. Zhu, and L. Yang, "Electromagnetically induced transparency-like effect in a single polydimethylsiloxane-coated silica microtoroid," *Appl. Phys. Lett.*, vol. 94, pp. 231115, 2009.

[23] Q. Z. Huang, Z. Shu, G. Song, J. G. Chen, J. S. Xia, and J. Z. Yu, "Electromagnetically induced transparencylike effect in a two-bus waveguides coupled microdisk resonator," *Opt. Express*, vol. 22, no. 3, pp. 3219–3227, 2014.

[24] W. Liang, L. Yang, J. K. S. Poon, Y. Huang, K. J. Vahala, and A. Yariv, "Transmission characteristics of a Fabry–Perot etalon–microtoroid resonator coupled system," *Opt. Lett.*, vol. 31, no. 4, pp. 510-512, 2006.

[25] C.-H. Dong, C.-L. Zou, Y.-F. Xiao, J.-M. Cui, Z.-F. Han, and G.-C. Guo, "Modified transmission spectrum induced by two-mode interference in a single silica microsphere," *J. Phys. B*, vol. 42, no. 21, pp. 215401, 2009.

[26] L. Chrostowski, V. M. Hochberg, *Silicon Photonics Design from Devices to Systems*, Cambridge University (2015).

[27] J. Cardenas, C. B. Poitras, J. T. Robinson, K. Preston, M. Chen, M. Lipson, “Low loss etchless silicon photonic waveguides,” *Opt. Express*, vol. 17, no. 6, pp. 4752-4757, 2009.

[28] Z. Zhang, G. I. Ng, T. Hu, H. Qiu, X. Guo, M. S. Rouifed, C. Liu, and H. Wang, “Electromagnetically induced transparency-like effect in microring-Bragg gratings based coupling resonant system,” *Opt. Express*, vol. 24, no. 12, pp. 25665-25675, 2016.

[29] W. Bogaerts, P. De Heyn, T. Van Vaerenbergh, K. De Vos, S. Kumar Selvaraja, T. Claes, P. Dumon, P. Bienstman, D. Van Thourhout, and R. Baets, “Silicon microring resonators,” *Laser & Phot. Rev.*, vol. 6, no. 1, pp. 47–73, 2012.

[30] J. Heebner, V. Wong, A. Schweinsberg, R. Boyd, and D. Jackson, “Optical transmission characteristics of fiber ring resonators,” *IEEE J. Quantum Electron.*, vol. 40, no. 6, pp. 726–730, 2004.

[31] K. Takahashi, Y. Kanamori, Y. Kokubun, and K. Hane, “A wavelength-selective add-drop switch using silicon microring resonator with a submicron-comb electrostatic actuator,” *Opt. Express*, vol. 16, pp. 14421-14428, 2008.

[32] C. Errando-Herranz, F. Niklaus, G. Stemme, and K. B. Gylfason, “Low-power microelectromechanically tunable silicon photonic ring resonator add–drop filter,” *Opt. Lett.*, vol. 40, pp. 3556-3559, 2015.

[33] P. Shi, G. Zhou, J. Deng, F. Tian, and F. S. Chau, “Tuning all-Optical Analog to Electromagnetically Induced Transparency in nanobeam cavities using nanoelectromechanical system,” *Sci. Rep.*, vol. 5, pp. 14379, 2015.

[34] L. Chen, N. Sherwood-Droz, and M. Lipson, “Compact bandwidth-tunable microring resonators,” *Opt. Lett.*, vol. 32, pp. 3361-3363, 2007.

[35] H. L. R. Lira, C. B. Poitras, and M. Lipson, “CMOS compatible reconfigurable filter for high bandwidth non-blocking operation,” *Opt. Express*, vol. 19, pp. 20115-20121, 2011.

[36] Z. Zhang, G. I. Ng, T. Hu, H. Qiu, X. Guo, M. S. Rouifed, C. Liu, and H. Wang, “Conversion between EIT and Fano spectra in a microring-Bragg grating coupled-resonator system,” *Appl. Phys. Lett.*, vol. 111, pp. 081105, 2017.

[37] S. Cueff, D. Li, Y. Zhou, F. J. Wong, J. A. Kurvits, S. Ramanathan, and R. Zia, “Dynamic control of light emission faster than the lifetime limit using VO2 phase-change,” *Nature Communications*, vol. 6, pp. 8636, Oct. 2015.

[38] A. B. Pevtsova, A. N. Poddubny, S. A. Yakovlev, D. A. Kurdyukov, and V. G. Golubev, “Light control in $Ge_2Sb_2Te_5$-coated opaline photonic crystals mediated by interplay of Wood anomalies and 3D Bragg diffraction,” *Journal of Applied Physics*, vol. 113, no. 14, pp. 144311 Apr. 2013.

[39] S. Zheng, Z. Ruan, S. Gao, Y. Long, S. Li, M. He, N. Zhou, J. Du, L. Shen, X. Cai, and J. Wang, “Compact tunable electromagnetically induced transparency and Fano resonance on silicon platform,” *Opt. Express*, vol. 25, no. 21, pp.

25655-25662, Oct. 2017.

[40] C. –Y. Chao and L. J. Guo, “Biochemical sensors based on polymer microrings with sharp asymmetrical resonance,” *Appl. Phys. Lett.*, vol. 83, no. 8, pp. 1527-1529, Aug. 2003.

Chapter 5
Dual-Band Optical Filters Based on Partial-Reflective-Element-Embedded Microring Resonator

5.1 Introduction

Dual-band optical filters (DBOFs) have been playing important roles in a wide range of optical applications, such as optical modulation [1], sensing [2], fast/slow light [3], etc. Multiple microring resonators have been utilized in various methods to realize the dual-band filtering spectrum, such as parallel coupling [4], series coupling [5], and some other combinations [6]. However, the multiple-microring-resonator structure is not suitable for high volume integration due to its large form factor. In this chapter, we demonstrate a new design based on a single microring resonator embedded with nanoholes, which is more compact and feasible for large-scale integration. Furthermore, we have improved the design and realized a single microracetrack resonator embedded with Bragg gratings. Through changing the dimensions of the Bragg gratings, the reflectivity of the Bragg grating can be tuned and the transmission spectrum can be engineered as well.

5.2 DBOF Based on A Single Microring Resonator Embedded with Nanoholes

Fig. 5.1(a) shows the schematic of the microring resonator embedded with two nanoholes. The two nanoholes act as two partial reflective elements and form a Fabry–Pérot (F-P) resonator. When the light is coupled into the microring from the bus waveguide, the coupling between the F-P resonator and the microring resonator gives rise to the dual-band optical filtering spectrum. A numerical model was built based on the transfer matrix method. As shown in Fig. 5.1(b), the transmission of light can be written as

$$E_t = E_i \cdot t + E_{t6} \cdot k \tag{5.1}$$

$$E_{t1} = E_i \cdot (-k^*) + E_{t6} \cdot t^* \tag{5.2}$$

$$E_{t2} = E_{t1} \cdot \alpha^{1/4} \cdot e^{1/4\, j\varphi} \tag{5.3}$$

$$E_{t3} = E_{t2} \cdot s + E_{r3} \cdot r \tag{5.4}$$

$$E_{t4} = E_{t3} \cdot \alpha^{1/2} \cdot e^{1/2\, j\varphi} \tag{5.5}$$

$$E_{t5} = E_{t4} \cdot s + E_{r5} \cdot r \tag{5.6}$$

$$E_{t6} = E_{t5} \cdot \alpha^{1/4} \cdot e^{1/4\, j\varphi} \tag{5.7}$$

$$E_{r3} = E_{r4} \cdot \alpha^{1/2} \cdot e^{-1/2\, j\varphi} \tag{5.8}$$

$$E_{r5} = E_{r6} \cdot t^* \cdot \alpha^{1/4} \cdot e^{-1/2\, j\varphi} \tag{5.9}$$

$$E_{r6} = E_{r2} \cdot \alpha^{1/4} \cdot e^{-1/4\, j\varphi} \tag{5.10}$$

$$E_{r2} = E_{r3} \cdot s + E_{t2} \cdot r \tag{5.11}$$

$$E_{r4} = E_{r5} \cdot s + E_{t4} \cdot r \tag{5.12}$$

where t is the transmission coefficient of the coupling region between the bus

waveguide and the microring; k is the coupling coefficient of the coupling region between the bus waveguide and the microring; E_{t1}~E_{t6} and E_{r1}~E_{r6} are the intensity of light at different positions, which have been marked in Fig. 5.1(b); E_i and E_t are the intensity of the input light and the output light respectively; α is the round-trip intensity attenuation and φ is the round-trip phase shift; s is the transmission coefficient of the nanoholes which act as partial reflective elements and r is the reflective coefficient; θ is the angle between the two nanoholes as marked in Fig. 5.1(b). The nanoholes are located at the center of the waveguides as shown in Fig. 5.1(a). The width of the waveguide is 500 nm. The effective indices of the waveguide under different wavelengths around 1.55 μm are calculated with the BeamPROP module of Rsoft software by taking the dispersion into account. Then equations (5.1) ~ (5.12) are calculated with Matlab in order to identify the optimized parameters.

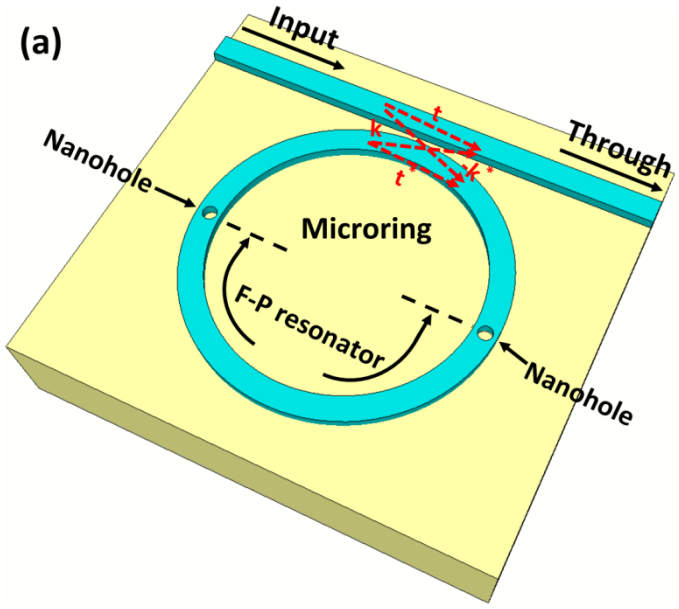

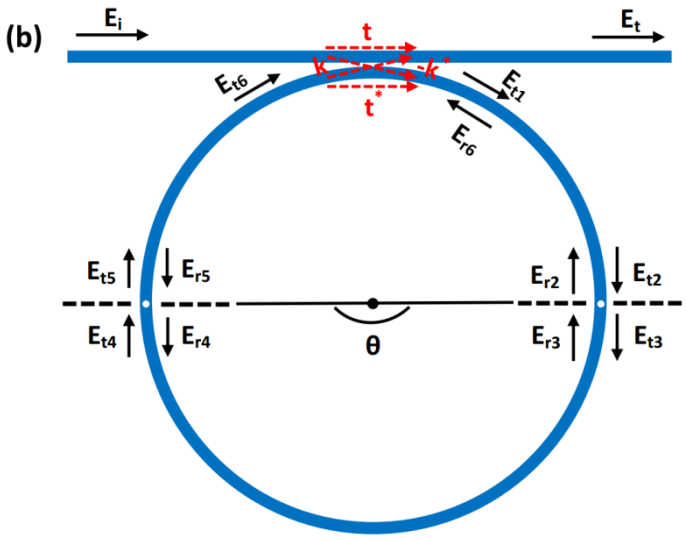

Fig.5.1 (a) The schematic of the microring resonator embedded with nanoholes. (b) The schematic of the light transmission path.

The single microring resonator embedded with nanoholes was fabricated on a silicon-on-insulator (SOI) wafer with a 220 nm-thick top silicon layer and a 2 μm-thick buried oxide (BOX) layer. Both the grating layer and waveguide layer are patterned with electron beam lithography (EBL). The grating layer is etched with reactive ion etching (RIE) to the depth of 70 nm. The waveguide layer is etched down to the BOX layer with deep reactive ion etching (DRIE) in order to have a straight and smooth sidewall. Then the sample is coated with a cladding layer of 1 μm SiO_2 with plasma-enhanced chemical vapor deposition (PECVD). The radius of the microring and the width of the strip waveguides are designed to be 10 μm and 500 nm respectively. The radius of the nanoholes are varied from 20 nm to 200 nm with a step size of 10 nm. After all the fabricated devices were characterized, we found the result of the device with the hole radius of 60 nm is the best. Since the scanning electron microscope

(SEM) images were taken after the removal of SiO_2 cladding layer by wet etching, a small portion of the exposed BOX layer was etched away and a part of the fabricated devices were contaminated including the device with the hole radius of 60 nm. In Fig. 5.2, the fabricated device with the hole radius of 160 nm is shown instead for an example.

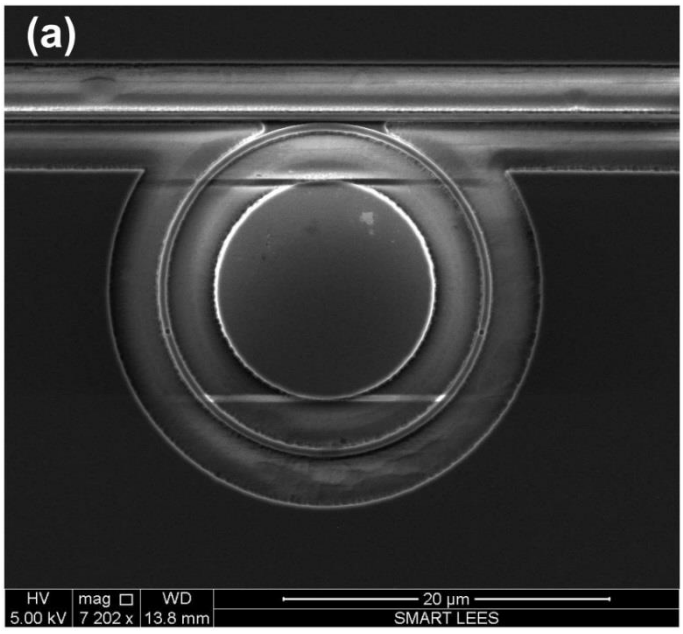

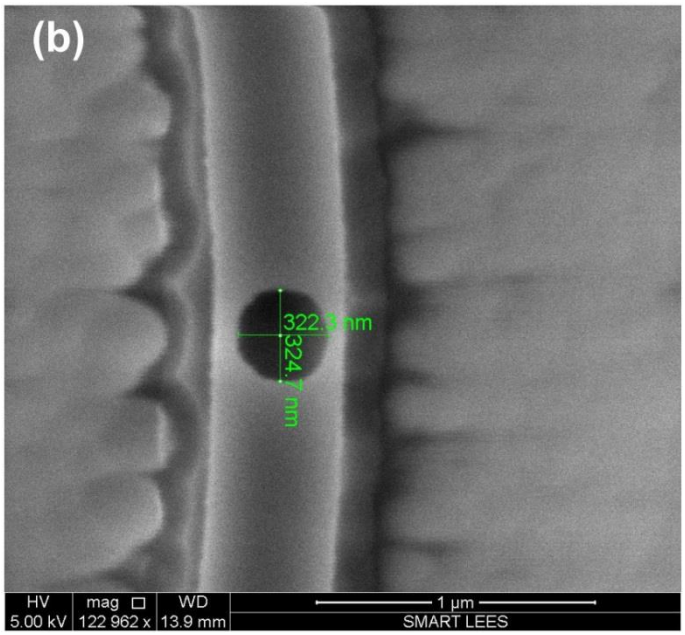

Fig.5.2 (a) The SEM image of the microring resonator embedded with nanoholes. (b) The zoom-in SEM image of a nanohole.

Fig. 5.3(a) shows the experimental transmission spectrum while the two nanoholes are located at two sides of the microring ($\theta = 180°$) as shown in Fig. 5.1(b), the hole radius = 60 nm, and the gap width (between the bus waveguide and the microring) = 110 nm. Fig. 5.3(b) shows the simulated results based on the numerical model mentioned above. As can be seen, two dips are generated and the separation between them is about 1 nm. The right dip is larger than the left one. The extinction ratio (ER) of the right dip can achieve ~ 9 dB. And the full-width-at-half-maximum (FWHM) is 0.13 nm, which corresponds to a quality factor (Q factor) of 11900. The insertion loss is lower than 1 dB. The small ripples are due to the weak optical reflection at the input and output facets. It can be clearly seen that the simulation and experimental results are in good agreement. The small difference of wavelength is probably due to the slight difference between the designed and fabricated radius of the microring or the difference between the real refractive index and the calculated refractive index by BeamPROP software.

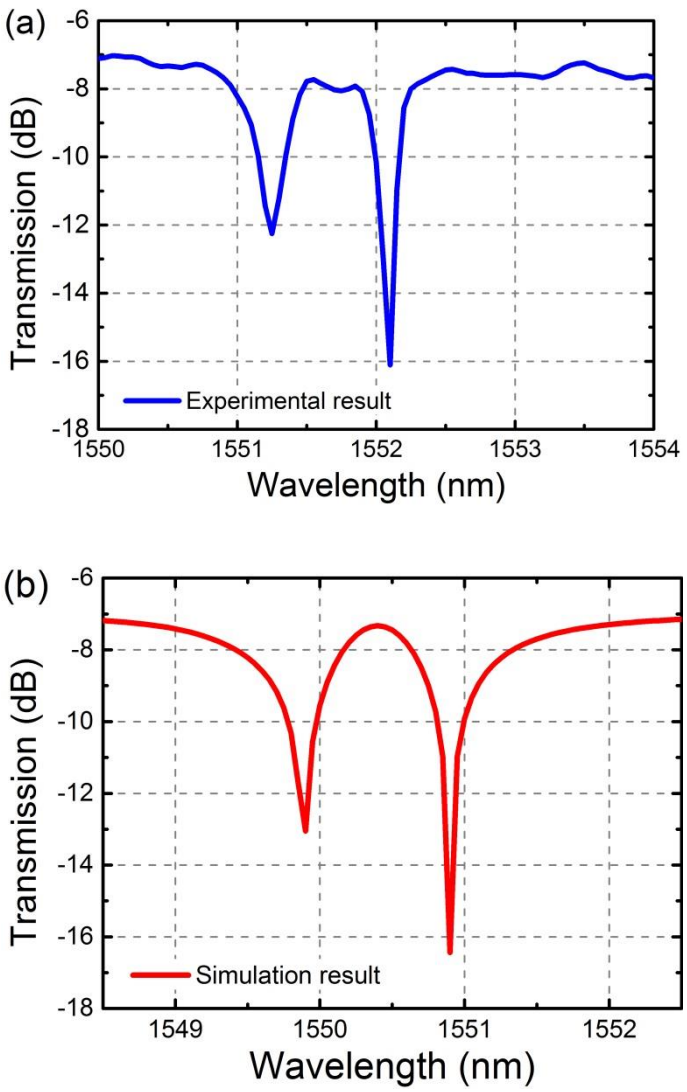

Fig.5.3 (a) The transmission spectrum when θ = 180°, the hole radius is 60 nm and the gap width is 110 nm. (b) The simulated transmission spectrum.

5.3 DBOF Based on A Microracetrack Resonator Embedded with Bragg Gratings

The schematic of the microracetrack resonator embedded with Bragg gratings is shown in Fig. 5.4. Two embedded Bragg gratings act as partial reflective elements to

form a Fabry-Perot resonator with a part of the microracetrack. The coupling between the F-P resonator and the microracetrack gives rise to the dual-band filtering transmission spectrum. In the simulation, we regard the Bragg grating as a periodic structure consisting of wide waveguide segments, narrow segments and reflective interfaces [7]. As shown in Fig. 5.5, the transmission spectrum is calculated with a specially designed numerical model based on the transfer matrix method. In this simulation, the parameters are chosen as: width of the waveguides = 500 nm, dw = 20 nm, pitch = 324 nm, the number of pitches = 20, radius of the microracetrack = 10.2 μm. The effective indices of the waveguides under different wavelengths around 1.55 μm are calculated with the BeamPROP module of Rsoft software by taking the dispersion into account.

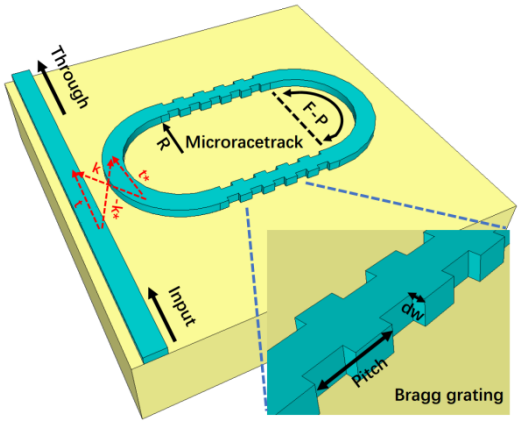

Fig.5.4 The schematic of the microracetrack resonator embedded with Bragg gratings.

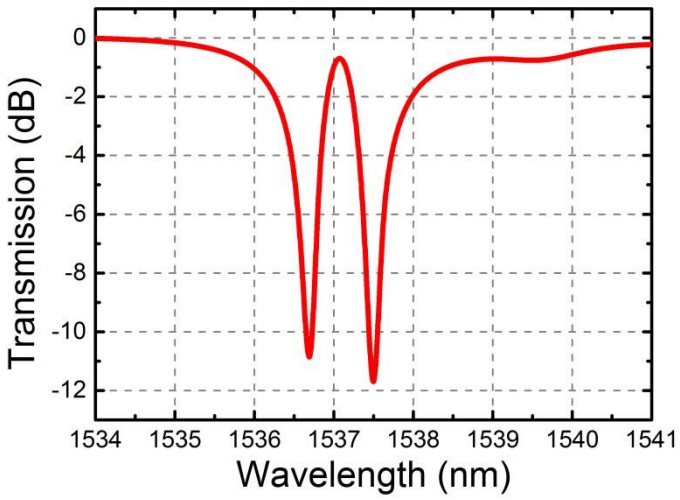

Fig.5.5 The simulated transmission spectrum of the microracetrack resonator embedded with Bragg gratings.

As shown in Fig. 5.6, the microracetrack resonator embedded with Bragg is fabricated on a SOI platform with a 220-nm top silicon slayer and a 2 μm BOX layer. The grating layer and the waveguide layer both are patterned with electron beam lithography. The grating layer is etched with RIE to the depth of 70 nm. The waveguide layer is etched down to the BOX layer. Then the sample is coated with a 1 μm SiO2 cladding layer. The characterizations are carried out at room temperature. The experimental results are plotted in Fig. 5.7. As it can be seen, the ERs of the dual-band filtering spectrum are ~ 4.5 dB. The separation between two notches is ~ 0.5 nm. The FWHMs are 0.05 nm and 0.045 nm, which correspond to the Q factors of 30900 and 34400. The insertion loss is < 0.5 dB. The uneven transmission may be caused by the F-P resonator formed by the two end facets of the bus waveguide. By reducing the roughness of the waveguide sidewalls, the ER can be further increased.

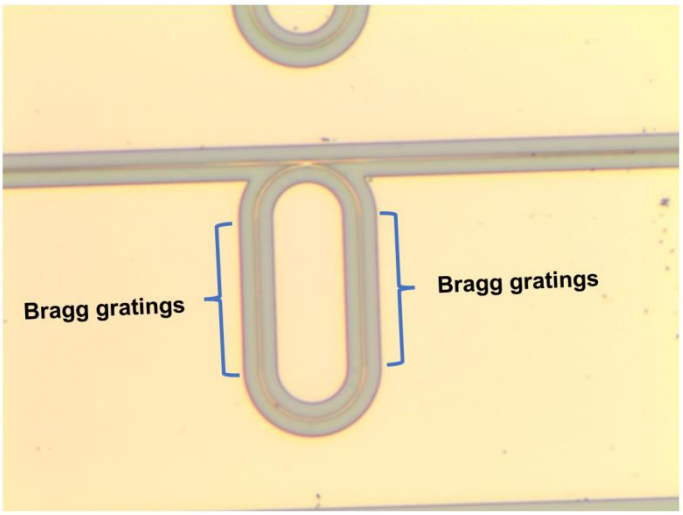

Fig.5.6 The fabricated microracetrack resonator embedded with Bragg gratings**.**

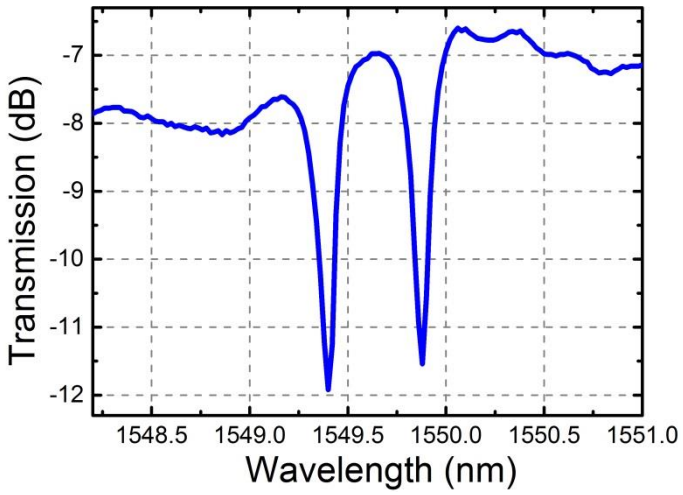

Fig.5.7 The experimental transmission spectrum of the microracetrack resonator embedded with Bragg gratings.

5.4 Conclusion and Discussions

In this chapter, we demonstrate a DBOF based on a single microring resonator embedded with nanoholes. The coupling between the F-P resonator formed by two nanoholes and the microring resonator gives rise to the dual-band optical filtering

spectrum. The ER is ~ 9 dB and the insertion loss is lower than 1 dB. Meanwhile, the Q factor can reach 11900. The separation between two dips is about 1 nm. Furthermore, we have also successfully demonstrated an improved DBOF based on a single microracetrack resonator embedded with Bragg gratings. Through changing the dimensions of the Bragg gratings, the reflectivity of the Bragg grating can be tuned and the transmission spectrum can be engineered as well. From the experimental results, the ERs of the dual-band filtering spectrum are ~ 4.5 dB. The separation between two notches is ~ 0.5 nm. The FWHMs are 0.05 nm and 0.045 nm, which correspond to the Q factors of 30900 and 34400. The insertion loss is < 0.5 dB. These two compact dual-band optical filters show great potential in applications, including modulators, sensors and time delay lines.

References

[1] S. Emelett and R. Soref, “Analysis of dual-microring-resonator cross-connect switches and modulators,” *Opt. Express*, vol. 13, no. 20, pp. 7840-7853, 2005.

[2] Y. F. Xiao, V. Gaddam, and L. Yang, “Coupled optical microcavities: an enhanced refractometric sensing configuration”, *Opt. Express*, vol. 16, no. 17, pp. 12538-43, 2008.

[3] T. Wang, F. Liu, J. Wang, Y. Tian, Z. Zhang, T. Ye, M. Qiu, and Y. Su, “Pulse Delay and Advancement in SOI Microring Resonators With Mutual Mode Coupling”, *J. Lightwave Technol.*, vol. 27, no. 21, pp. 4734-4743, 2009.

[4] T. Kato, Y. Goebuchi, and Y. Kokubun, “Improvement of Switching Characteristics of Hitless Wavelength-Selective Switch with Double-Series-Coupled Microring Resonators”, *Jpn. J. Appl. Phys.*, vol. 45, pp. 7741, 2006.

[5] Y. Tian, L. Zhang, R. Ji, L. Yang, P. Zhou, H. Chen, J. Ding, W. Zhu, Y. Lu, L. Jia, Q. Fang, and M. Yu, “Proof of concept of directed OR/NOR and AND/NAND logic circuit consisting of two parallel microring resonators”, *Opt. Lett.*, vol. 36, issue 9, pp. 1650-1652, 2011.

[6] L. Y. Mario, D. C. S. Lim, and M. K. Chin, “Proposal of ultranarrow passband using two coupled rings”, *IEEE Photon. Technol. Lett.*, vol. 19, issue 20, pp. 1688-1690, 2007.

[7] L. Chrostowski, V. M. Hochberg, *Silicon Photonics Design from Devices to Systems*, Cambridge University, (2015).

Chapter 6
Sensor Based on Suspended Microracetrack Resonator

6.1 Introduction

In the last several decades, silicon photonics based on the silicon-on-insulator (SOI) platform has attracted a lot of research interest, because it can utilize the mature fabrication processes developed within the CMOS industry, resulting in low cost fabrication. A great deal of effort has been invested in SOI based bio-chemical sensing in the near-infrared (NIR) band, typically around 1.3-1.6 μm wavelength [1-6]. Various structures have been utilized to achieve high sensitivity. In 2014, Sahba Talebi Fard et al. obtained a sensitivity of 100 nm/RIU with a TE resonator sensor based on ultra-thin Si waveguides [7]. Series' of slot-waveguide-based microring sensors have been reported to reach a sensitivity of 298 nm/RIU [8-10]. Additionally, sub-wavelength-grating waveguide-based microring sensors have been demonstrated to achieve a sensitivity as high as 490 nm/RIU [11-15]. The mid-infrared (MIR) band (2–20 μm) is also very crucial in analyzing and sensing various important organic and inorganic materials as their molecules have vibration modes with frequency fingerprints in this band [16-18]. However, limited work has been reported on SOI platform based MIR sensors. One of the limitations of MIR sensing based on the SOI platform is the large optical absorption in buried-oxide-layer (BOX) at wavelengths beyond 4 μm. One solution to this problem is to form suspended structures with the

BOX layer etched away, which can also enhance the interaction between the mode field and the material under test, and therefore increase the sensitivity of the device [19-22]. In 2012, Z. Cheng et al. claimed a suspended membrane waveguide based microring resonator operating at 2.75 μm [23]. In 2013, Y. Xia et al. experimentally reported a suspended Si resonator operating at 3.4 μm and 5.2 μm [24]. However, to form their structures, multiple etching processes are required, including a partial Si etching to form the rib waveguides and a Si full etching to form the via-holes for the subsequent hydrofluoric acid (HF) etching of the BOX layer. Furthermore, the wide and thin slabs supporting the rib waveguides, which aim to suppress the mode leakage, provide limited mechanical stability.

In this chapter, we theoretically and experimentally demonstrate a MIR bio-chemical sensor based on a one-time Si etching suspended microracetrack resonator with a lateral sub-wavelength-grating (SWG) metamaterial cladding on a commercial SOI platform. A quality factor (Q factor) of 15300 and an extinction ratio (ER) of 12.1 dB were obtained at 2 μm wavelength. Furthermore, we have also calculated and analyzed the influence of three important parameters (the duty-cycle of the SWG cladding, the thickness of the waveguides and the width of the waveguides) on the sensitivity with a specially developed numerical model. The expected sensitivity of the fundamental TE mode is calculated to be 337.5 nm/RIU. Compared with the state-of–the-art reported data, this system shows great potential for sensing applications in the MIR band.

6.2 Design and Optimization of Suspended SWG Waveguide

The one-time Si etching suspended microracetrack resonators with lateral SWG metamaterial claddings are designed on a commercial SOI wafer with 340 nm-thick-top-silicon and 2 μm-thick BOX layer. The cladding layer is air. At first, designing and optimizing the fundamental building block, namely the suspended waveguide, as shown in Fig. 6.1, was carried out.

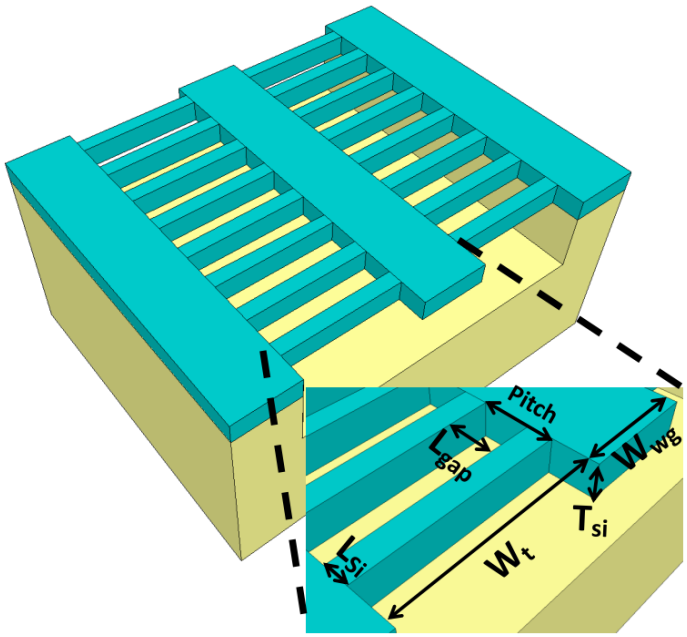

Fig.6.1 The schematic of the one-time etching suspended waveguide with lateral SWG metamaterial cladding.

For the optimization of the suspended waveguide, three crucial points need to be addressed: (1) diffractive effect and back-reflections caused by the SWG structure; (2) mechanical stability; and (3) enhancement of the interaction between the evanescent field and the chemicals under test. Firstly, in order to suppress the diffractive effect

and back-reflections caused by the SWG structure, the pitch of the SWG ($Pitch = L_{si} + L_{gap}$) needs to follow the Bragg condition [21]:

$$Pitch < Pitch_{Bg} = \frac{\lambda}{2n_{B-F}} \tag{6.1}$$

where $Pitch_{Bg}$ is the Bragg period; λ is the operating wavelength; and n_{B-F} is the effective index of the fundamental Bloch-Floquet mode propagating in the waveguide. Secondly, in order to obtain a mechanically robust structure to overcome the fluctuations caused by testing liquid or gas flow, wide silicon pillars are required. However, it is known that the sensitivity is determined by the interaction between the evanescent field and the chemicals under test [25]. The trade-off is that whilst the pitch is fixed and the duty-cycle ($DC = L_{si} / (L_{si} + L_{gap}) = L_{si} / Pitch$) increases, the exposed area of waveguide becomes smaller, as well as the overlap between the evanescent field and the chemicals under test, which results in the degradation of sensitivity. So a balance between mechanical stability and sensitivity needs to be considered under the precondition of a small enough *Pitch* that can suppress the diffractive effect and back-reflections caused by the SWG structure. The width of the lattice is set as 2 μm to prevent lateral mode leakage. Two further important parameters are the width and the thickness of the waveguides. A shrink of the waveguide cross-section area will compress the mode field. Consequently, more energy will gather at the surface of the waveguide, thus bringing a stronger interaction between the evanescent field and the chemicals under test, but at the expense of a

higher propagation loss. This is another trade-off to be considered when designing the device.

In order to test and verify the above discussions, suspended waveguides with different dimensions were fabricated on a commercial SOI wafer with a 340 nm-thick-top-silicon layer and a 2 μm BOX layer. The waveguide and SWG cladding are simultaneously defined with electron beam lithography (EBL), and subsequently fully etched to the BOX layer with deep reactive ion etching (DRIE) in order to have a straight and smooth sidewall. Finally, the BOX layer is removed with buffered oxide etching (BOE) solution (6 parts 40% NH_4F and 1 part 49% HF) for 25 minutes at an average etch rate of ~ 65 nm/min.

All the characterizations are conducted under room temperature with the fundamental TE mode. As shown in Fig. 6.2(a), when $DC = 0.3$, $Pitch > 450$ nm, the propagation loss suddenly increases significantly and reaches the limitation of our detector (-32 dB) due to the serious diffractive effect and back reflections caused by the SWG supporting structure. With an increase of DC to 0.8, the cut-off point moves to smaller pitches, which is consistent with the reported simulation results [21]. In order to avoid the diffractive effect and back reflections whilst retaining a large exposed waveguide area, we choose the dimensions as $Pitch = 350$ nm and $DC = 0.3$. Fig. 6.2(b) shows the influence of the waveguide width on the propagation loss with $Pitch = 350$ nm and $DC = 0.3$. As seen, with the increase of width from 600 nm to 800 nm, the propagation loss drops dramatically. But with further width increases, the

propagation loss does not decrease significantly. Although wider waveguides (W_{wg} > 800 nm) can offer better mode confinement and slightly lower propagation losses, the sensor sensitivity is degraded by a reduction in the interaction between the evanescent field and the chemicals under test. As a result, we set W_{wg} = 800 nm in order to have a balance between the propagation loss and the sensitivity. Due to the limitation of experimental setup, the impact of the thickness is investigated by simulations instead of experiments, which will be demonstrated in section 3. With all the above optimized parameters and T_{si} = 340 nm, the propagation loss has been plotted and fitted in Fig. 6.2(c). As seen, the propagation loss of the one-time Si etching suspended waveguide is approximately 9.2 dB/cm.

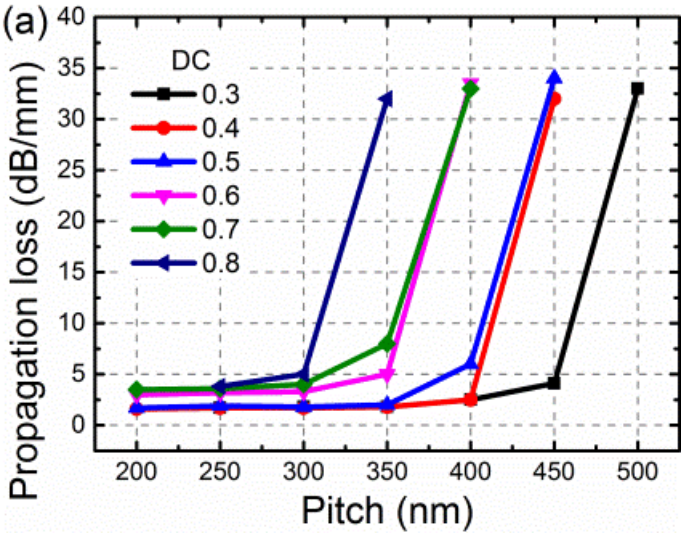

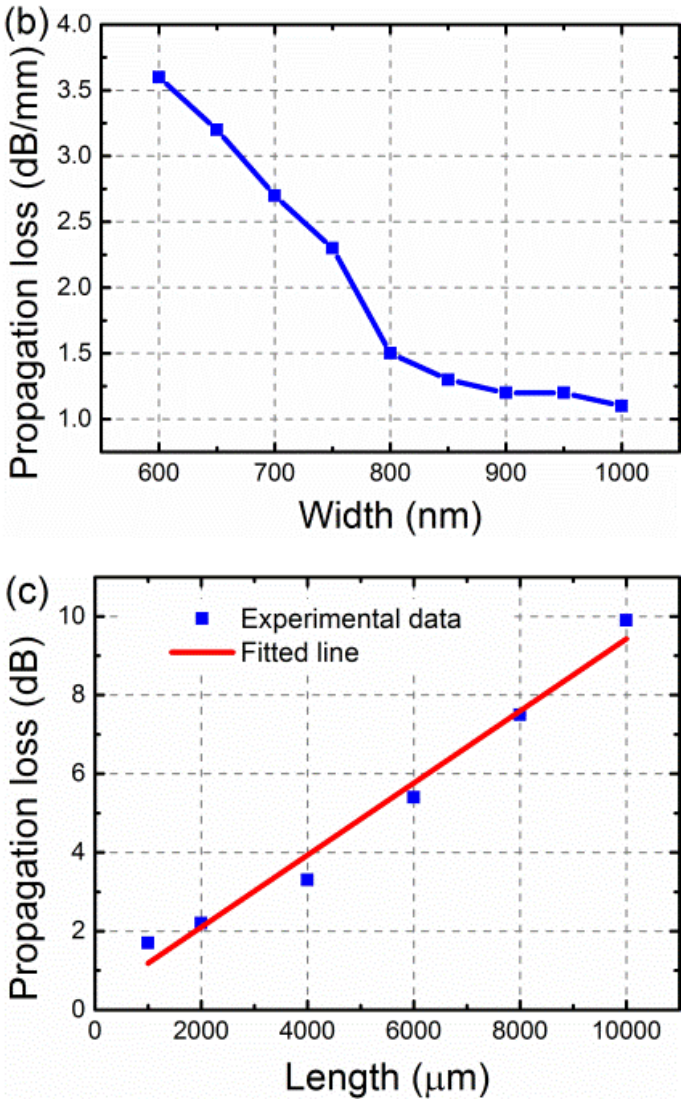

Fig.6.2 (a) The propagation loss under different DC and Pitch when W_{wg} = 800 nm and T_{si} = 340 nm. (b) The propagation loss under different W_{wg} when DC=0.3, Pitch = 350 nm and T_{si} = 340 nm. (c) The experimental measured propagation loss and fitted line when DC=0.3, Pitch = 350 nm, W_{wg} = 800 nm and T_{si} = 340 nm.

Based on the above suspended waveguides ($Pitch$ = 350 nm, DC = 0.3, W_{wg} = 800 nm, and T_{si} = 340 nm), the suspended microracetrack resonator was fabricated and characterized. The scanning electron microscope (SEM) images of the fabricated device are shown in Fig. 6.3. The coupling length (CL) and the gap width (W_g)

between the bus waveguide and the microracetrack are 10 μm and 200 nm respectively. The bend radius (R) is 50 μm. The shadow area at the outside of the lattice is due to the removal of the BOX layer with a width of ~1.6 μm. Since the etching of BOE is isotropic, it can be confirmed that the waveguide is fully suspended.

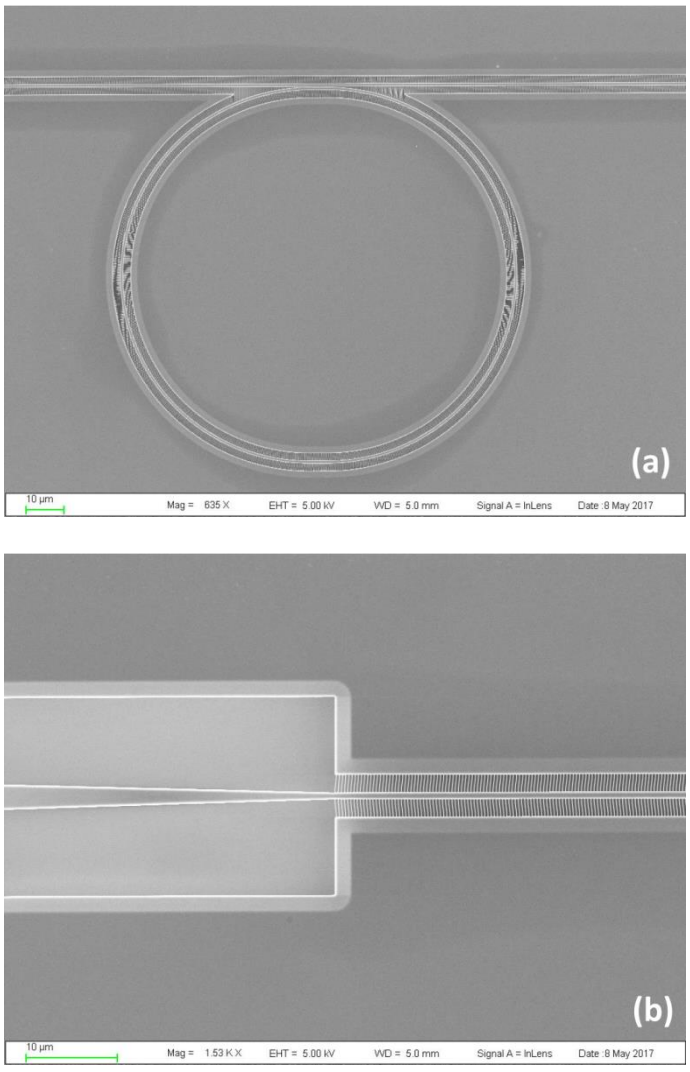

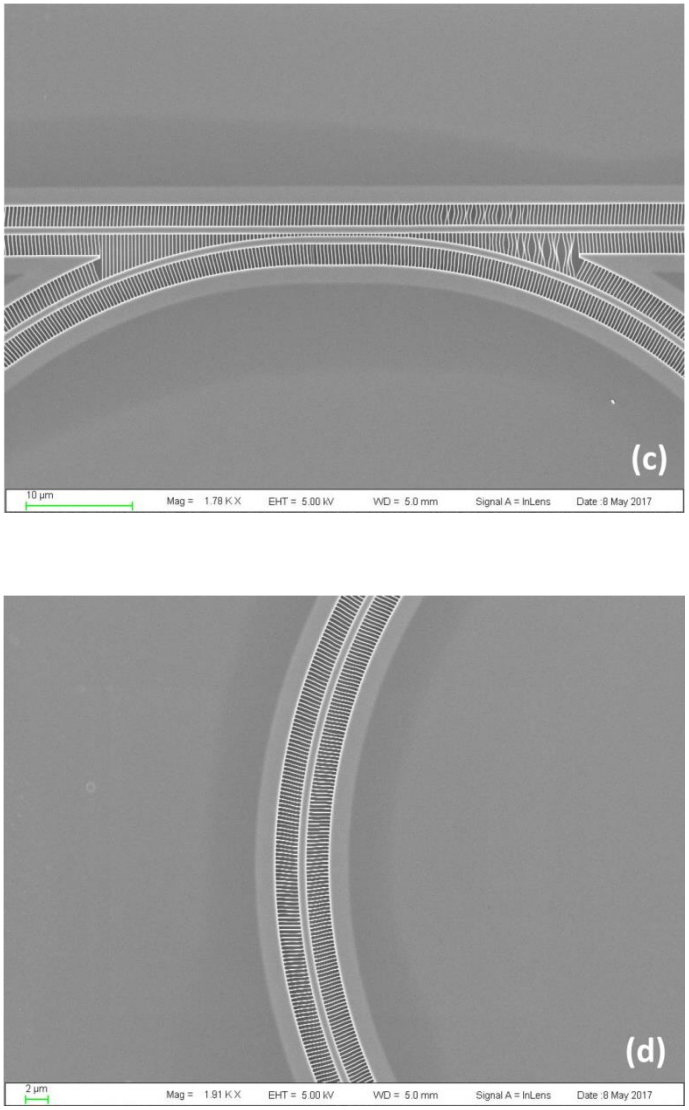

Fig.6.3 SEM images of (a) The one-time Si etching suspended microracetrack resonator. (b) The transition region. (c) The coupling region. (d) The microracetrack bend.

The experimental and theoretical fitting results are shown in Fig. 6.4. The fitting numerical model is specially developed with the equivalent refractive index model. The equivalent refractive index model is a convenient and helpful approach for facilitating the design of SWG based structures, which has been utilized and validated in many reported works [14,15,26-33]. But it needs to be noted that this approach is a

narrowband approximation, especially when the dimensions of the SWG is close to the Bragg condition, as shown in equation (1). For an accurate broadband simulation, full 3D-FDTD simulation or some more complex numerical models as reported in [34-41] should be used. Here, since *Pitch* = 350 nm is far smaller than the Bragg period, and the calculation is conducted in a narrowband (1995-2005 nm), the equivalent refractive index model can be applied for the lateral SWG cladding metamaterial, which can be written as:

$$n_{eq} = n_{cladding} + DC * (n_{si} - n_{cladding}) \tag{6.2}$$

where $n_{cladding}$ is the refractive index of the cladding layer, such as the chemicals under test; and n_{si} is the refractive index of silicon. With this equivalent refractive index of the lateral cladding layer, the effective indices of the suspended waveguide at different wavelengths can be calculated with the BeamPROP module of Rsoft software by taking the dispersion into account. Then, by substituting the effective indices into our numerical model and tuning the coupling coefficient k and round-trip power attenuation α^2, the fitted transmission spectrum can be obtained. The fitting parameters are: k = 0.41i, and α^2 = 0.895. From the measurements, the full-width-at-half-maximum (FWHM) is approximately 0.13 nm, which corresponds to a Q factor of ~15300. The ER is approximately 12.1 dB.

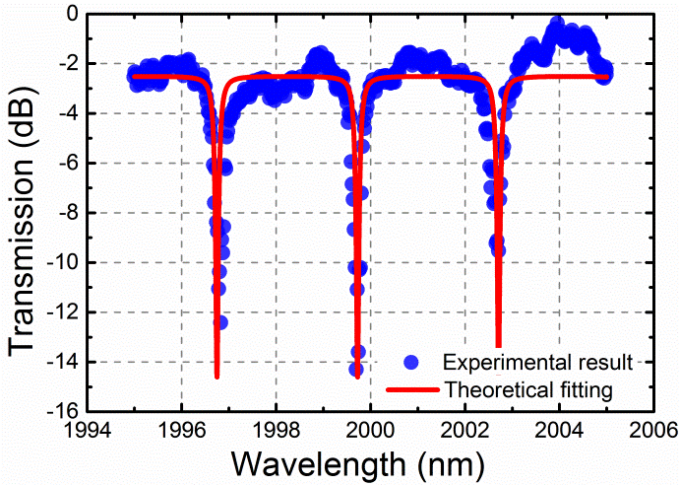

Fig.6.4 The experimental and theoretical fitting results of the one-time etching suspended microracetrack with SWG metamaterial cladding under CL = 10 μm, W_g = 200 nm, and R = 50 μm.

6.3 Sensing Performance Simulation and Analysis

With the equivalent refractive index method and our numerical model, the expected sensitivity for the microracetrack resonator can be calculated. Here, we calculate the sensitivity of our device to ethanol-water solutions of different concentrations (0% ~ 4%). The refractive index of pure water is 1.306 at 2 μm wavelength. When the concentration increases by 1%, the refractive index of the ethanol-water solution increases by 0.00047. As demonstrated in equation (6.2), DC will directly influence the equivalent refractive index of the lateral cladding metamaterial, and consequently impact the device sensitivity. Additionally, W_{wg} and T_{si} also influence the sensitivity by compressing the mode field and changing the interaction between the evanescent field and the chemicals under test. So here we mainly discuss the impact of these

three factors on the sensitivity. In all the simulations, the other parameters are fixed as: k = 0.35i, α^2 = 0.9331. Through calculating the transmission spectra with the ethanol-water solution cladding of different concentrations and measuring the wavelength shifts of the microracetrack resonant dip, the sensitivities can be obtained. As shown in Fig. 6.5(a), when DC increases, the sensitivity of the fundamental TE mode decreases as the exposed area to the chemicals under test becomes smaller. Furthermore, it can be seen that the sensitivity when W_{wg} = 600 nm is higher than when W_{wg} = 800 nm. This is because, when W_{wg} is smaller, the fundamental TE mode is more compressed and the field energy is closer to the side walls, which results in a stronger interaction between the evanescent field and the chemicals under test. However, more energy gathering at the side walls also leads to a larger impact from the dimensions of the corrugations, such as DC, which is the reason why the total decrease of sensitivity when W_{wg} = 600 nm is also larger than W_{wg} = 800 nm. As demonstrated in Fig. 6.5(b), with the increase of W_{wg} from 600 nm to 1000 nm, the sensitivity of the fundamental TE mode drops by ~46.7%. This is due to the fact that when the width increases, the confinement of the mode field is stronger, and the interaction between the evanescent field and the chemicals under test becomes weaker. As seen in Fig. 6.5(c), with an increase in thickness, the sensitivity of the fundamental TE mode drops considerably. Meanwhile, the decreasing rate of the sensitivity gradually reduces. This is because when the thickness is small and the mode field is compressed, the interaction between the evanescent field and the

chemicals occurring at the upper and the lower surfaces of the waveguide is much stronger compared to when the thickness is larger. It is noteworthy that when T_{si} = 120 nm, the expected sensitivity of the fundamental TE mode can achieve 337.5 nm/RIU. This sensitivity is more than 3 times the reported ultra-thin TE resonator sensor (100nm/RIU) [7], and is comparable to the reported slot-waveguide-based microring sensors (298 nm/RIU) [8-10]. Although the sensitivity is lower than the reported sub-wavelength-grating waveguide-based microring sensors (490 nm/RIU) [11-15], the advantage of this suspended microracetrack resonator sensor is that it can avoid absorption from the BOX layer, especially when one extends the use of this structure to longer wavelengths in the MIR band.

Furthermore, as the change of thickness has a larger impact on the mode field in the vertical direction than the lateral direction, the sensitivity of the fundamental TM mode may have a larger benefit than the fundamental TE mode from the same reduction of the waveguide thickness. Hence, a higher sensitivity of the fundamental TM mode can be expected. Besides, by utilizing post-fabrication treatments such as Piranha etch/HF cycling and annealing, the surface roughness and therefore round-trip propagation loss can be reduced leading to a further improved sensitivity.

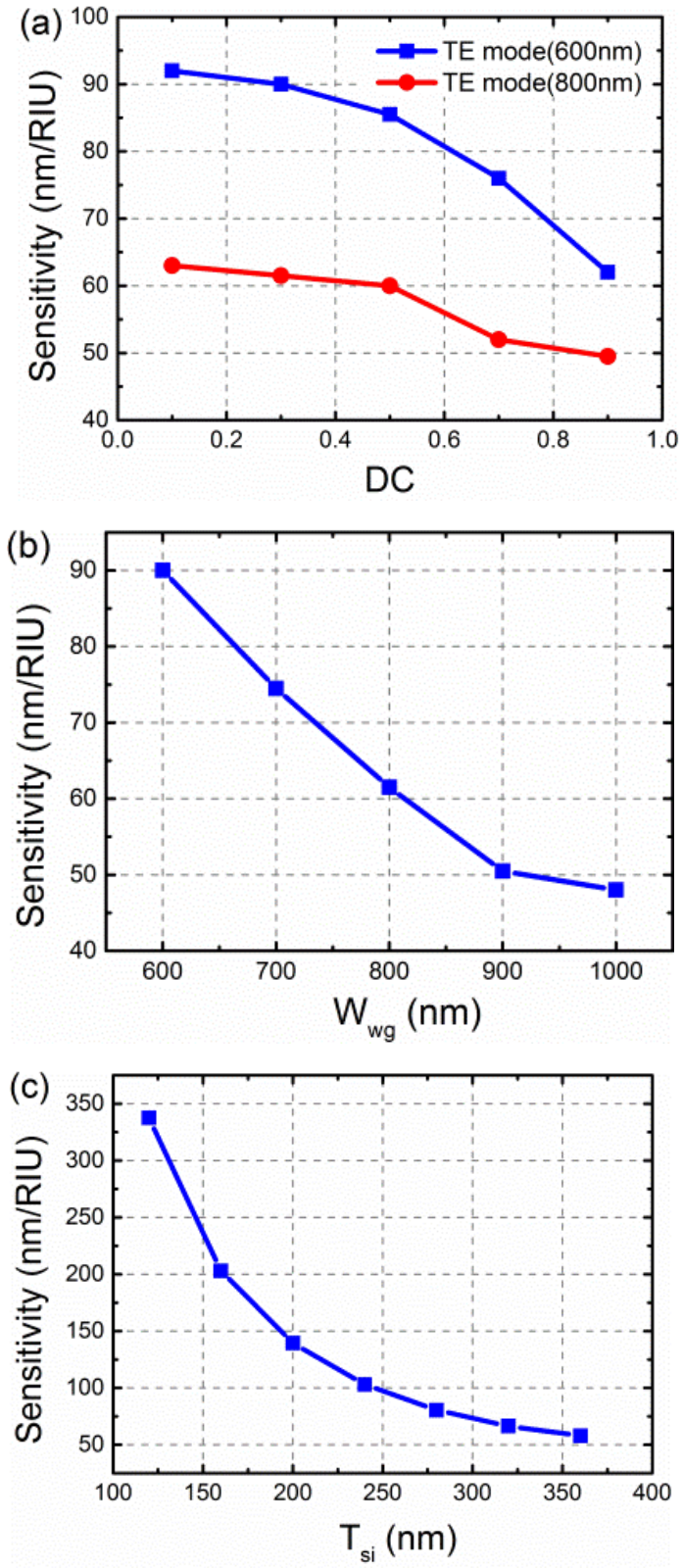

Fig.6.5 (a) The sensitivities of fundamental TE mode under different DC when W_{wg} is 600 nm and 800 nm (T_{si} = 340 nm). (b) The sensitivities of fundamental TE mode at different W_{wg} when DC = 0.3 and T_{si} = 340 nm. (c) The sensitivities of fundamental

TE mode under different T_{si} when DC = 0.3 and W_{wg} = 800 nm.

6.4 Conclusion and Discussions

In this chapter, we theoretically and experimentally demonstrate a MIR sensor based on a one-time Si etching suspended microracetrack resonator with lateral SWG metamaterial cladding. With the suspended structure, the interaction between the evanescent field and the chemicals under test is enhanced, which is helpful for improving the sensitivity. The one-time Si etching process also simplifies the device fabrication. Various suspended waveguides with different dimensions were fabricated and characterized. The propagation loss of the optimized suspended waveguide is experimentally measured as ~9.2 dB/cm. Based on the optimized suspended waveguide, the one-time Si etching suspended microracetrack resonator was fabricated and tested. The experimental data is well fitted with our specially developed numerical model. The ER of the suspended microracetrack resonator is ~12.1 dB. The FWHM is approximately 0.13 nm, which corresponds to a Q factor of ~15300. With the equivalent refractive index method and our numerical model, the influence of three key parameters on the sensitivity are simulated and analyzed. The expected sensitivity of the fundamental TE mode is calculated as 337.5 nm/RIU. The results presented in this chapter show great potential for ultra-sensitive, simple to fabricate, low cost MIR integrated optical bio-chemical sensing applications.

References

[1] K. D. Vos, I. Bartolozzi, E. Schacht, P. Bienstman, and R. Baets, "Silicon-on-Insulator microring resonator for sensitive and label-free biosensing," *Opt. Express*, vol. 15, no. 12, pp. 7610-7615, 2007.

[2] K. D. Vos, J. Girones, S. Popelka, E. Schacht, R. Baets, and P. Bienstman, "SOI optical microring resonator with poly(ethylene glycol) polymer brush for label-free biosensor applications," *Biosensors and Bioelectronics*, vol. 24, no. 8, pp. 2528–2533, 2009.

[3] A. L. Washburn, L. C. Gunn, and R. C. Bailey, "Label-free quantitation of a cancer biomarker in complex media using silicon photonic microring resonators," *Anal. Chem.*, vol. 81, no. 22, pp. 9499–9506, 2009.

[4] L. Washburn, M. S. Luchansky, A. L. Bowman, and R. C. Bailey, "Quantitative, label-free detection of five protein biomarkers using multiplexed arrays of silicon photonic microring resonators," *Anal. Chem.*, vol. 82, no. 1, pp. 69–72, 2010.

[5] J. G. W.-Pérez, P. Cheben, A. Ortega-Moñux, C. A.-Ramos, D. P.-Galacho, R. Halir, I. M.-Fernández, D.-X. Xu, and J. H. Schmid, "Evanescent field waveguide sensing with subwavelength grating structures in silicon-on-insulator," *Opt. Lett.*, vol. 39, no. 15, pp. 4442-4445, 2014.

[6] X. Wang, J. Flueckiger, S. Schmidt, S. Grist, S. T. Fard, J. Kirk, M. Doerfler, K. C. Cheung, D. M. Ratner, and L. Chrostowski, "A silicon photonic biosensor

using phaseshifted Bragg gratings in slot waveguide," *J. Biophoton.*, vol. 6, no. 10, pp. 821-828, 2013.

[7] S. T. Fard, V. Donzella, S. A. Schmidt, J. Flueckiger, S. M. Grist, P. T. Fard, Y. Wu, R. J. Bojko, E. Kwok, N. A. F. Jaeger, D. M. Ratner, and L. Chrostowski, "Performance of ultra-thin SOI-based resonators for sensing applications," *Opt. Express*, vol. 22, no. 12, pp. 14166-14179, 2014.

[8] W. C. Jiang and Q. Lin, "Suspended silicon slotted microring resonators with ultra-high optical quality," *Proc. SPIE 9367 Silicon Photonics X*, pp. 936708, 2015.

[9] T. Claes, J. G. Molera, K. D. Vos, E. Schacht, R. Baets. and P. Bienstman, "Label-free biosensing with a slot waveguide-based ring resonator in silicon on insulator," *IEEE Photonics J.*, vol. 1, no. 3, pp. 197–204, 2009.

[10] K. B. Gylfason, C. F. Carlborg, A. Kaźmierczak, F. Dortu, H. Sohlström, L. Vivien, C. A. Barrios, W. V. D. Wijngaart, and G. Stemme, "On-chip temperature compensation in an integrated slot-waveguide ring resonator refractive index sensor array," *Opt. Express*, vol. 18, no. 4, pp. 3226-3237, 2010.

[11] P. J. Bock, P. Cheben, J. H. Schmid, J. Lapointe, A. Delâge, S. Janz, G. C. Aers, D.-X. Xu, A. Densmore, and T. J. Hall, "Subwavelength grating periodic structures in silicon-on-insulator: a new type of microphotonic waveguide," *Opt. Express*, vol. 18, no. 19, pp. 20251-20262, 2010.

[12] J. Wang, I. Glesk, and L. R. Chen, "Subwavelength grating filtering devices,"

Opt. Express, vol. 22, no. 13, pp. 15335-15345, 2014.

[13] V. Donzella, A. Sherwali, J. Flueckiger, S. T. Fard, S. M. Grist, and L. Chrostowski, "Sub-wavelength grating components for integrated optics applications on SOI chips," *Opt. Express*, vol. 22, no. 17, pp. 21037-21050, 2014.

[14] V. Donzella, A. Sherwali, J. Flueckiger, S. M. Grist, S. T. Fard, and L. Chrostowski, "Design and fabrication of SOI micro-ring resonators based on sub-wavelength grating waveguides," *Opt. Express*, vol. 23, no. 4, pp. 4791-4803, 2015.

[15] J. Flueckiger, S. Schmidt, V. Donzella, A. Sherwali, D. M. Ratner, L. Chrostowski, and K. C. Cheung, "Sub-wavelength grating for enhanced ring resonator biosensor," *Opt. Express*, vol. 24, no. 14, pp. 15672-15686, 2016.

[16] K. Miyamoto, K. Ishibashi, K. Hiroi, Y. Kimura, H. Ishii, and M. Niwano, “Label-free detection and classification of DNA by surface vibration spectroscopy in conjugation with electrophoresis,” *Appl. Phys. Lett.*, vol. 86, pp. 053902, 2005.

[17] F. K. Tittel, Y. Bakhirkin, A. Kosterev, R. Lewicki, S. So, G. Wysocki, and R. F. Curl, “Recent advances and applications of mid-infrared based trace gas sensor technology,” *Proc. SPIE 6900*, pp. 69000Z, 2008.

[18] M. Sieger and B. Mizaikoff, “Toward On-Chip Mid-Infrared Sensors,” *Anal. Chem.*, vol. 88, no. 11, pp. 5562-5573, 2016.

[19] R. Soref, “Mid-infrared photonics in silicon and germanium,” *Nat. Photonics*, no.

4, pp. 495-497, 2010.

[20] Z. Cheng, X. Chen, C. Y. Wong, K. Xu, C. K. Y. Fung, Y. M. Chen, and H. K. Tsang, "Focusing subwavelength grating coupler for mid-infrared suspended membrane waveguide," *Opt. Lett.*, vol. 37, no. 7, pp. 1217-1219, 2012.

[21] J. S. Penadés, C. A.-Ramos, A. Z. Khokhar, M. Nedeljkovic, L. A. Boodhoo, A. O.-Moñux, I. M.-Fernández, P. Cheben, and G. Z. Mashanovich, "Suspended SOI waveguide with sub-wavelength grating cladding for mid-infrared," *Opt. Lett.*, vol. 39, no. 19, pp. 5661-5664, 2014.

[22] J. S. Penades, A. O.-Moñux, M. Nedeljkovic, J. G. W.-Pérez, R. Halir, A. Z. Khokhar, C. A.-Ramos, Z. Qu, I. M.-Fernández, P. Cheben, and G. Z. Mashanovich, "Suspended silicon mid-infrared waveguide devices with subwavelength grating metamaterial cladding," *Opt. Express*, vol. 24, no. 20, pp. 22908-22916, 2016.

[23] Z. Cheng, X. Chen, C. Y. Wong, K. Xu, and H. K. Tsang, “Mid-infrared Suspended Membrane Waveguide and Ring Resonator on Silicon-on-Insulator,” *IEEE Photon. J.*, vol. 4, no.5, pp. 1510-1519, 2012.

[24] Y. Xia, C. Qiu, X. Zhang, W. Gao, J. Shu, and Q. Xu, "Suspended Si ring resonator for mid-IR application," *Opt. Lett.*, vol. 38, no. 7, pp. 1122-1124, 2013.

[25] H. Sohlström; K. B. Gylfason; D. Hill, “Real-time label-free biosensing with integrated planar waveguide ring resonators,” *Proc. SPIE 7719 Silicon Photonics and Photonic Integrated Circuits II*, pp. 77190B, 2010.

[26] L. Li and J. J. Burke, “Linear propagation characteristics of periodically segmented waveguides,” *Opt. Lett.*, vol. 17, no. 17, pp. 1195–1197, 1992.

[27] J. D. Bierlein, “Propagation in segmented waveguide structures,” *Quantum Electronics and Laser Science Conference*, pp. QTuE2, 1992.

[28] V. Rastogi, V. Mahalakshmi, M. R. Shenoy, K. Thyagarajan, “Propagation characteristics of a novel complementary-structure planar segmented waveguide,” *Optics Communications*, vol. 148, pp. 230-235, 1998.

[29] Z. Weissman and A. Hardy, “Modes of Periodically Segmented Waveguides,” *Journal of Lightwave Technology*, vol. 11, no. 11, 1993.

[30] Z. Weissman and I. Hendel, “Analysis of Periodically Segmented Waveguide Mode Expanders,” *Journal of Lightwave Technology*, vol. 13, no. 10, 1995.

[31] D. Ortega, J. M. Aldariz, J. M. Arnold, and J. S. Aitchison, “Analysis of “Quasi-Modes” in Periodic Segmented Waveguides,” *Journal of Lightwave Technology*, vol. 17, no. 2, 1997.

[32] Z. Weissman, “Evanescent field sensors with periodically segmented waveguides,” *Applied Optics*, vol. 36, no. 6, pp. 1218-1222, 1997.

[33] P. J. Bock, P. Cheben, J. H. Schmid, J. Lapointe, A. Delâge, S. Janz, G. C. Aers, D.-X. Xu, A. Densmore, and T. J. Hall, “Subwavelength grating periodic structures in silicon-on-insulator: a new type of microphotonic waveguide,” *Optics Express*, vol. 18, no. 19, pp. 20251-20262, 2010.

[34] S. Fan, J. D. Joannopoulos, J. N. Winn, A. Devenyi, J. C. Chen, and R. D. Meade,

"Guided and defect modes in periodic dielectric waveguides," *J. Opt. Soc. Am. B*, vol. 12, no. 7, pp. 1267–1272, 1995.

[35] S. F. Helfert and R. Pregla, "Efficient Analysis of Periodic Structures," *J. Lightwave Technol.*, vol. 16, no. 9, pp. 1694–1702, 1998.

[36] S. G. Johnson and J. D. Joannopoulos, "Block-iterative frequency-domain methods for Maxwell's equations in a planewave basis," *Opt. Express*, vol. 8, no. 3, pp. 173–190, 2001.

[37] J. Ctyroky, S. Helfert, R. Pregla, P. Bienstman, R. Baets, R. De Ridder, R. Stoffer, G. Klaasse, J. Petrac ´ˇek, P. Lalanne, J. Hugonin, and R. De LaRue, "Bragg waveguide grating as a 1D photonic band gap structure: COST 268 modelling task," *Opt. Quantum Electron.*, vol. 34, pp. 455–470, 2002.

[38] J. Hugonin, P. Lalanne, I. D. Villar, and I. Matias, "Fourier modal methods for modeling optical dielectric waveguides," *Opt. Quantum Electron.*, vol. 37, no. 1-3, pp. 107–119, 2005.

[39] G. Lecamp, J. P. Hugonin, and P. Lalanne, "Theoretical and computational concepts for periodic optical waveguides," *Opt. Express,* vol. 15, no.18, pp. 11042–11060, 2007.

[40] L. Zavargo-Peche, A. Ortega-Monux, J. G. Wanguemert-Perez, and I. Molina-Fernandez, "Fourier based combined techniques to design novel sub-wavelength optical integrated devices," *Prog. Electromagn. Res.*, vol. 123, pp. 447–465, 2012.

[41] J. Ctyroky, “3-D Bidirectional Propagation Algorithm Based on Fourier Series,” *J. Lightwave Technol.*, vol. 30, no. 23, pp. 3699–3708, 2012.

Chapter 7
Thermal-Optic and Electro-Optic Modulators at 2 μm Wavelength

7.1 Introduction

Optical modulators are key components for optical signal processing. So far most of the efforts are focused on the development and improvement of optical modulators operating in near-infrared (NIR) tele- and data- communication band (1.3-1.6 μm) [1-10]. Two of the widely used mechanisms for tuning the refractive index of silicon are: thermo-optic effect and free-carrier plasma dispersion effect [11,12]. And the commonly utilized passive structures for building modulators are microring resonators and Mach-Zehnder interferometers (MZI). Generally, MZI based modulators can offer a better performance, such as high ER and fast modulating speed. However, MZI based modulators need a DC bias for operation and thus increase the power consumption. Besides, the footprint of MZI based modulators is usually very large ~1 to 2 mm. Compared with MZI based modulators, the footprints of microring resonator based modulators are much smaller, which is crucial for dense integration. Although the performance of microring resonator based modulators may not be as good as MZI based modulators, the microring based modulators have other advantages, such as low insertion loss and low power consumption.

As the demand for high volume information transmission increases, 2 μm wavelength offers a promising solution to extend the operating wavelength of communication

system to short MIR wavelengths. So far very limited work has been reported on the optical modulator on silicon-on-insulator (SOI) platform operating at 2 μm wavelength. In this chapter, a microracetrack resonator based thermal-optic (TO) modulator and a MZI-based electro-optic (EO) modulator operating at 2 μm wavelength are experimentally demonstrated.

7.2 Thermal-Optic Modulator Design and Fabrication

The working principle of a microring resonator based TO modulator is as follows: as a result of the relatively large thermo-optical coefficient of silicon [13], when the temperature of silicon increases, the refractive index of silicon will change as well as the effective refractive index of waveguides, which in turn leads to the shifting of transmission spectrum. The transmission intensity at the original wavelength of the resonance dip will be consequently changed and hence the modulation of light is realized. In this work, the thermal electrodes are placed above the microracetrack cavity. Since metals have high absorption of light field, a SiO_2 cladding layer is deposited on the SOI wafer in order to separate the thermal electrodes and light field as shown in Fig. 7.1.

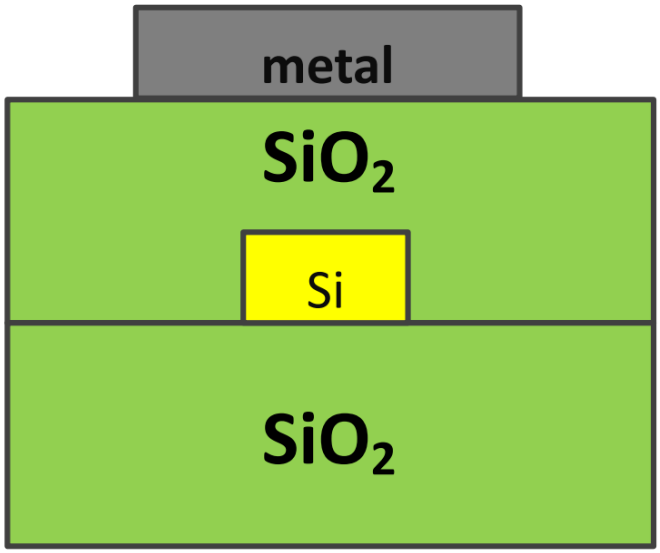

Fig.7.1 The cross-section of the thermos-optical phase shifter.

The microracetrack resonator is fabricated on a commercial SOI platform with a 340 nm-thick top-silicon layer and a 2 μm-thick buried oxide (BOX) layer. The width of the waveguide is 600 nm. The bending radius of the microracetrack is 25 μm. The coupling length is 20 μm. The gap width between the bus waveguide and the microracetrack is 160 nm. The patterns of the grating couplers and waveguides both are written with electron beam lithography (EBL) system. The grating coupler layer is etched to a depth of 100 nm with reactive ion etching (RIE). The waveguide layer is etched directly to the BOX layer with deep reactive ion etching (DRIE) in order to have smooth and vertical sidewalls. Next, a 1 μm-thick SiO_2 cladding layer is deposited with plasma-enhanced chemical vapor deposition (PECVD). Subsequently, the patterns of electrodes are written with EBL system. A layer of 110 nm-thick Ti is firstly deposited with electron beam evaporator as the heat-generating part and the unwanted part of Ti is removed with lift-off process. Then the contact electrode pad is

deposited, which is consisted of 20 nm Ti and 300 nm Au. Based on above design of the heating wires, as simulated with a bias of 3V, when the distance to the heating wire is larger than 12 μm, the temperature influence on the silicon waveguide can be ignored. So the distance between the heating wire and the bus waveguide is kept larger than 12 μm in order to avoid the unwanted thermo-optical effect. The fabricated microracetrack resonator based thermal-optic modulator is shown in Fig. 7.2. The width of the heat-generating part is 1.5 μm, which fully covers the waveguide region. The contact electrode pad is designed as a square of 80 μm * 80 μm for probing purpose.

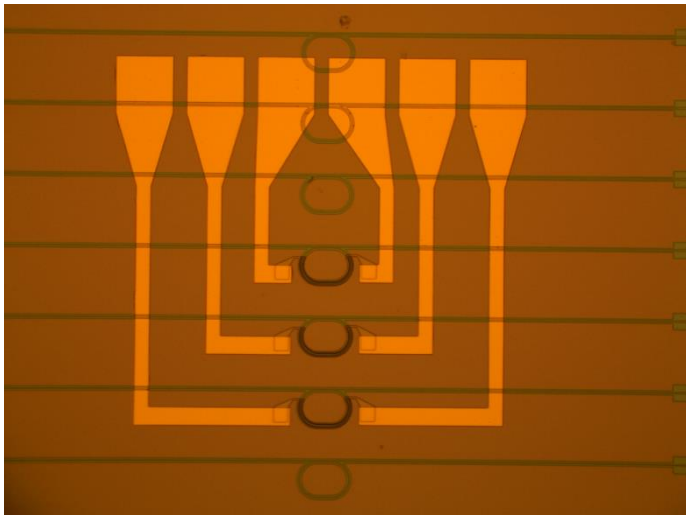

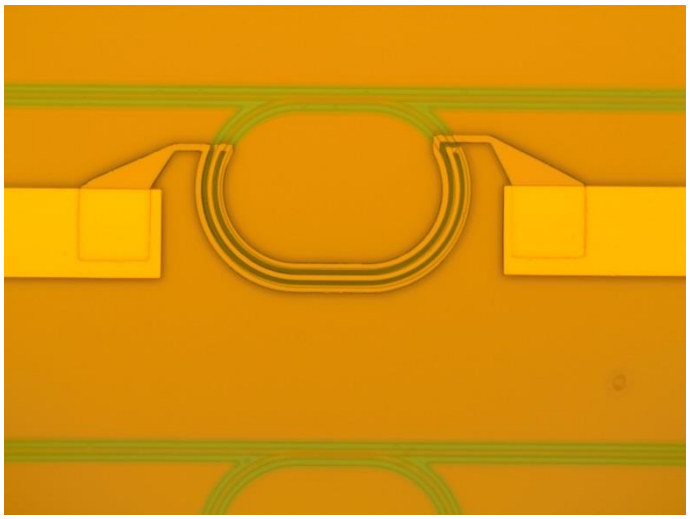

Fig.7.2 The fabricated microracetrack resonator based thermal-optic modulator.

7.3 Experimental Results of Thermal-Optic Modulator

The schematic of our thermal-optic DC characterization setup is shown in Fig. 7.3. We utilize the DC power supply to apply different bias to the thermal phase shifter. The temperature change is proportional to the applied voltage. Then at each bias, we utilize the tunable laser source to scan the transmission spectrum of the microracetrack resonator. The images of the testing platform are shown in Fig. 7.4.

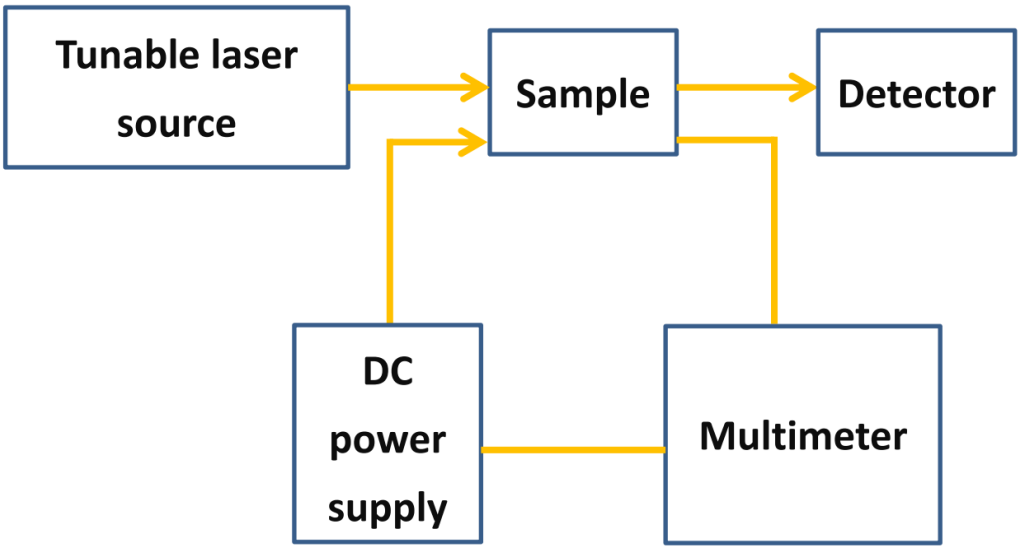

Fig.7.3 The DC characterization setup of the thermal-optic modulator.

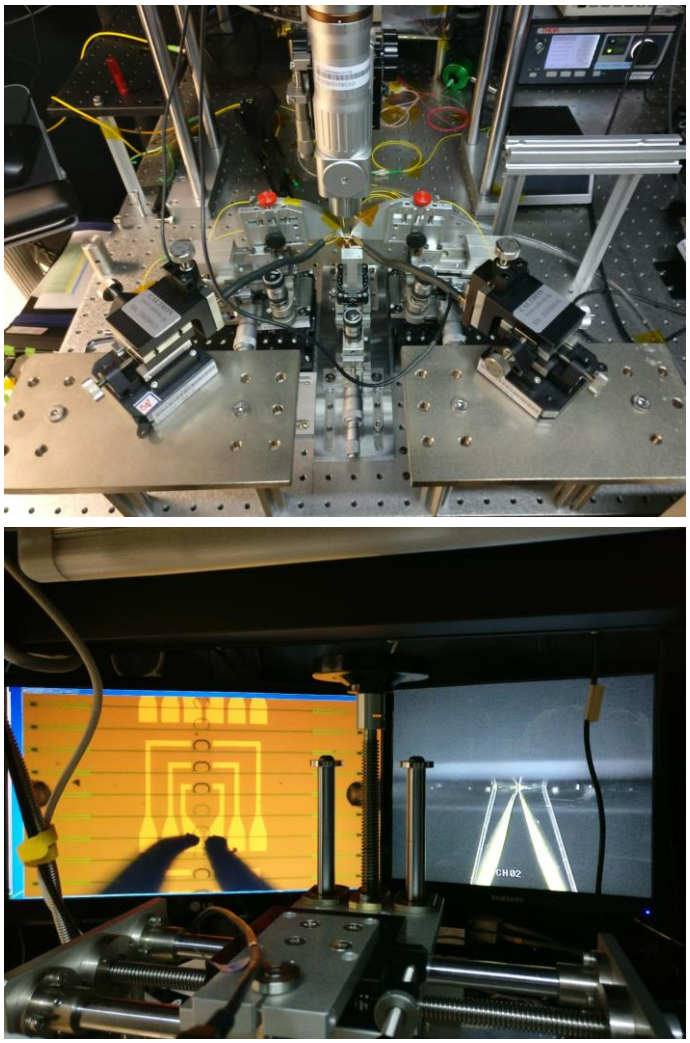

Fig.7.4 The images of the testing platform for the DC characterization of the thermal-optic modulator.

The tested spectra under different bias are shown in Fig. 7.5. It can be seen that, with the increase of applied voltage, a red-shift was observed for the resonance dip. As measured, the DC shifting efficiency is ~0.05 nm/V. It is noteworthy that, when the applied voltage is larger than 3V, the depth of resonance dip significantly increases. This is because under such a high voltage, the temperature is so high that it even influences the coupling region and the bus waveguide. When the temperature of the

SiO_2 at the coupling region increases, the refractive index of SiO_2 also changes. Consequently, the coupling coefficient k is changed as well as the resonant status of the microracetrack resonator. Because of the change of the coupling coefficient k, the resonant status is closer to the critical coupling status, which results in a larger extinction ratio (ER).

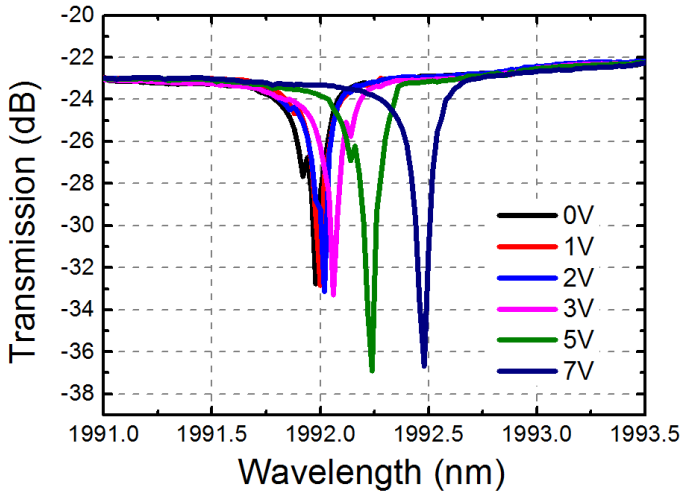

Fig.7.5 The transmission spectra of the microracetrack resonator under different bias.

The schematic of our thermal-optical RF characterization setup is shown in Fig. 7.6. At first, we need to use a tunable laser source to scan the transmission spectrum of the microracetrack resonator without applying any modulating signal as we need to find and record the wavelength of the resonance dip. Then we use a fixed wavelength laser source to replace the tunable laser source and set the wavelength at the resonance dip. By applying the square wave RF signal to the electrodes, the resonance dip will shift and the intensity of the output light will be modulated. Because of the high input power requirement of our 2 μm wavelength high-speed detector, a thulium-doped

fiber amplifier (TDFA) is applied between the fixed wavelength laser source and the sample in order to increase the input light power. With the help of the oscilloscope, we can find out the intensity change of the output light by reading the recovered electric signal from the detector.

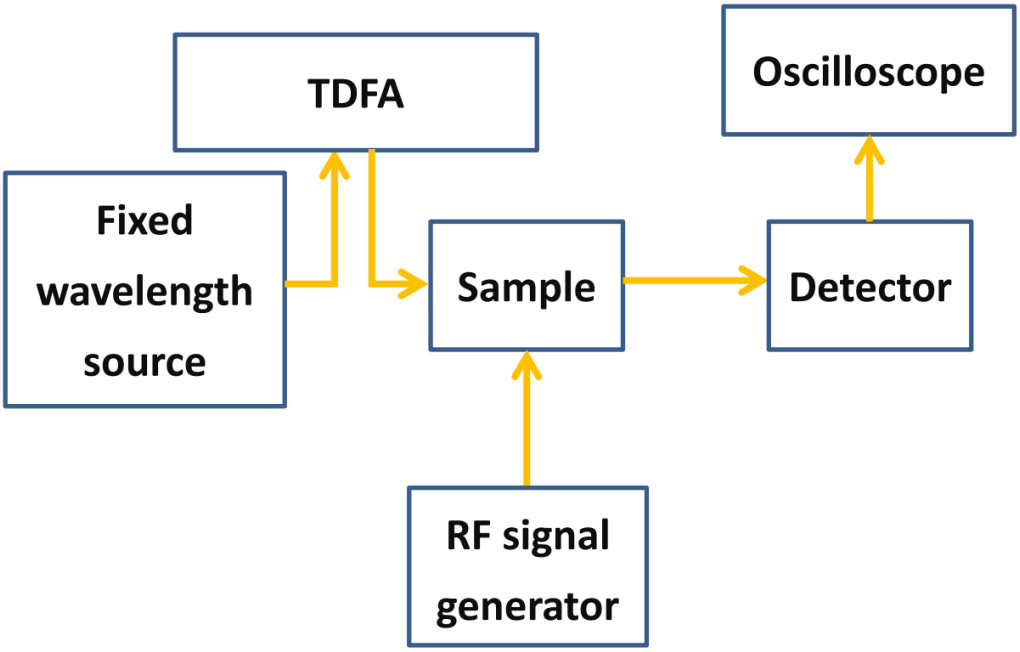

Fig.7.6 The RF characterization setup of the thermal-optic modulator.

As shown in Fig. 7.7, the yellow line is the input RF square wave signal and the blue line is the output light signal. As seen, the rise time of the input RF signal is 69.24 ns which is much smaller than the rise time of our TO modulator (11.35 μs). This means that the speed of the RF signal generator and the detector is fast enough for testing our TO modulator. Based on this rise time, we can calculate the -3 dB bandwidth with equation (7.1):

$$Bandwdith(GHz) = \frac{0.35}{risetime(ns)} \tag{7.1}$$

As calculated, the -3 dB bandwidth of our TO modulator is ~30.8 KHz.

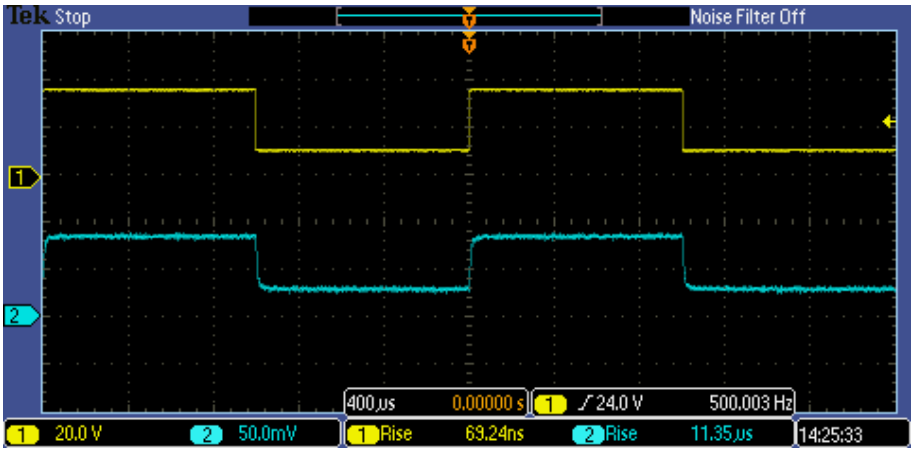

Fig.7.7 The waveform of the input RF signal and the output light.

7.4 Electro-Optic Modulator Design and Fabrication

Through applying and changing the bias voltage, the carriers in the waveguide are depleted. As reported in [12], due to the free carrier dispersion effect and the change of the carrier concentration in the waveguide region, the phase of the output light is changed and hence the modulation of light is realized. The asymmetric MZI-based EO modulator is fabricated on a commercial 220 nm-top-silicon-layer SOI wafer as shown in Fig. 7.8. By applying a reverse bias voltage to the phase shifter on the modulation arm of the MZI, the phase of the light in the modulation arm is changed and then the interference output between the modulation arm and the reference arm is changed. Thus the phase modulation of light is converted to into intensity modulation. As designed, the width of the waveguides is 600 nm. The length of the phase shifter is 1500 µm. The length difference between the modulating arm and the reference arm is

50 μm. The thickness of the slab is 70 nm. Two identical multimode interferometers (MMI) are used to split and recombine the optical beam in the MZI. The PN junction in the core area of waveguides is interleaved and the ratio (the heavy P-type doping area: heavy N-type doping area) is set as 1:1 in order to have a higher modulation efficiency. The width of RF coplanar waveguide (CPW) is designed as 10 μm and the gap width between two CPWs is set as 6.4 μm. A 50 Ohm resistance was connected to the end of the RF electrode to realize the impedance match. The heavy P-type and N-type doping concentration of the electrode-contact regions are ~1.5E20 ions/cm^3 and ~8.5E20 ions/cm^3 respectively. The light P-type and N-type doping concentration of the waveguide region are ~2.2E17 ions/cm^3 and ~1.2E17 ions/cm^3 respectively.

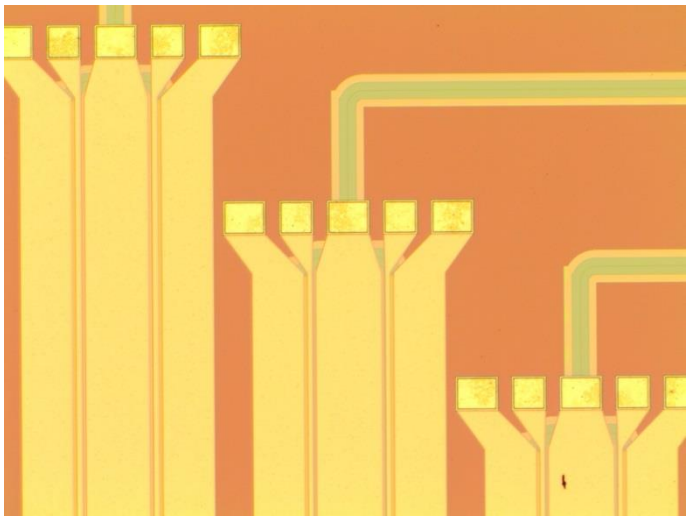

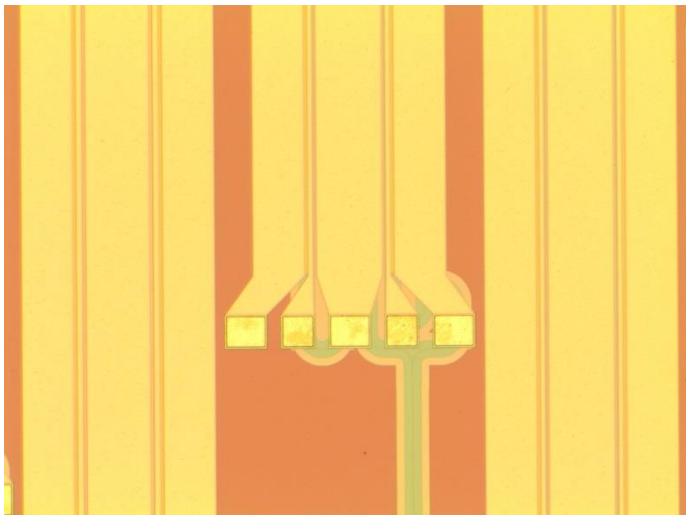

Fig.7.8 The fabricated MZI-based electro-optic modulator.

7.5 Experimental Results of Electro-Optic Modulator

At first, the DC characterization was conducted. The transmission spectra of the MZI were scanned over a wavelength range of 10 nm between 1971 nm and 1981 nm. Different bias from -1 V to -5 V was applied to the phase shifter for each transmission scan. The transmission spectra are shown in Fig. 7.9. The modulation efficiency $V_\pi \cdot L_\pi$ (voltage-length required to achieve a π phase shift for a given length) can be calculated as 3.84 V•cm.

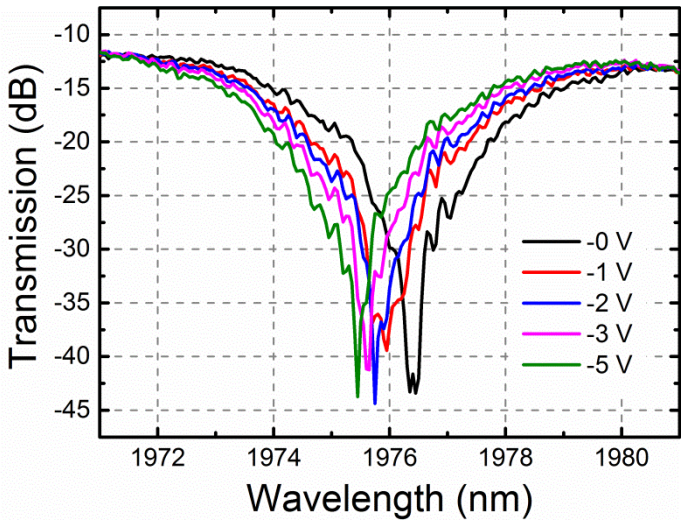

Fig.7.9 The transmission spectra of the MZI under different bias.

Next, the RF performance of the MZI based EO modulator is characterized. Firstly, the electro-optic bandwidth is characterized with the setup as shown in Fig. 7.10. The images of the characterization platform are shown in Fig. 7.11. The DC signal and the RF signal from the network analyzer are applied to the phase shifter with a bias tee. And the CPW was terminated by a DC block and 50 Ohm load. The DC bias is set at -3 V. The -3 dB working point is selected at the wavelength of 1973.2 nm. The V_{pp} is set as 2V.

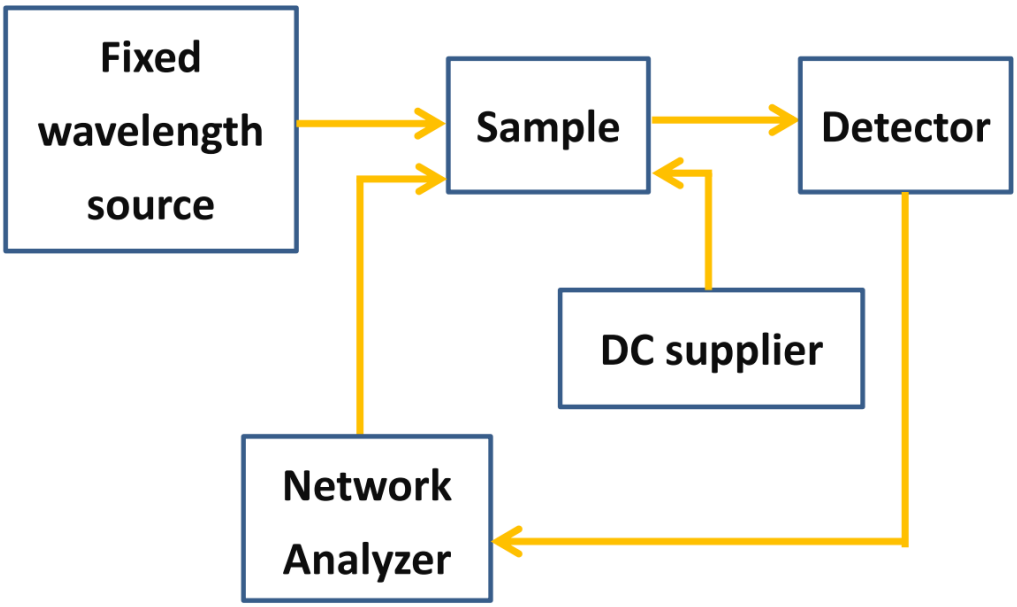

Fig.7.10 The characterization setup for testing the electro-optic bandwidth.

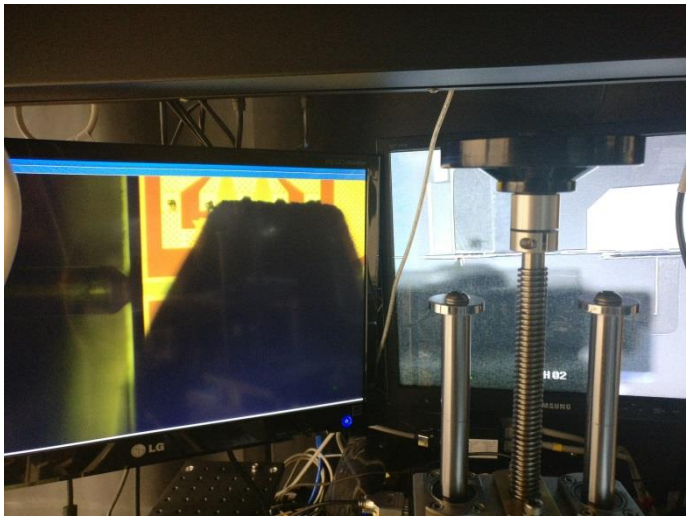

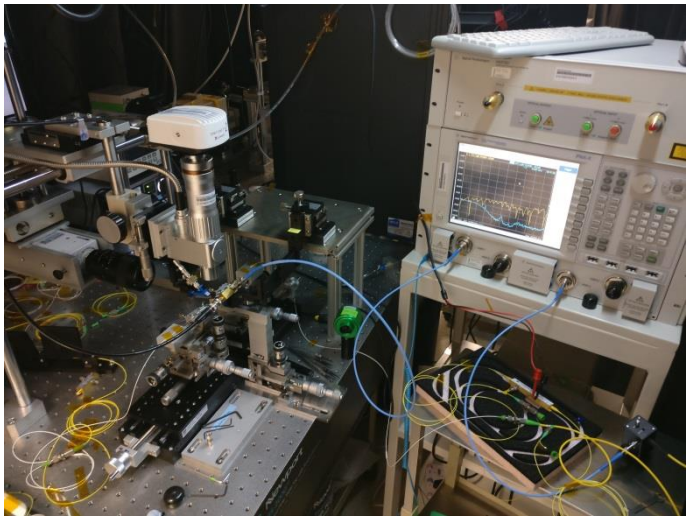

Fig.7.11 The images of the characterization platform for measuring the electro-optic bandwidth.

Before the characterization of our device, we tested a commercial modulator operating at 2 μm wavelength in order to have a reference for the normalization. The speed limitations of the commercial modulator and the detector both are 12.5 GHz. The normalized characterization result of our modulator is shown in Fig. 7.12. It can be clearly seen that when the frequency is 12.5 GHz, the transmission only drops by ~2 dB. Hence, it is believed that the -3 dB bandwidth of our modulator is beyond the limitation of the commercial modulator and the detector (12.5 GHz). Compared with the reported modulators operating in NIR band, such as 30 Gb/s in [14], 40 Gb/s in [15], 50Gb/s in [16], and 56 Gb/s in [17], our modulator still has a large room to improve. By optimizing the doping ratio between P++ and N++ or utilizing the interdigitated PN junction, the modulation efficiency can be improved as well as the modulating speed. By using the push-pull traveling wave electrodes, the modulation power consumption can be reduced and the modulating speed can be increased. And by removing the substrate, the electrode transmission loss can be reduced and the modulation efficiency can be improved.

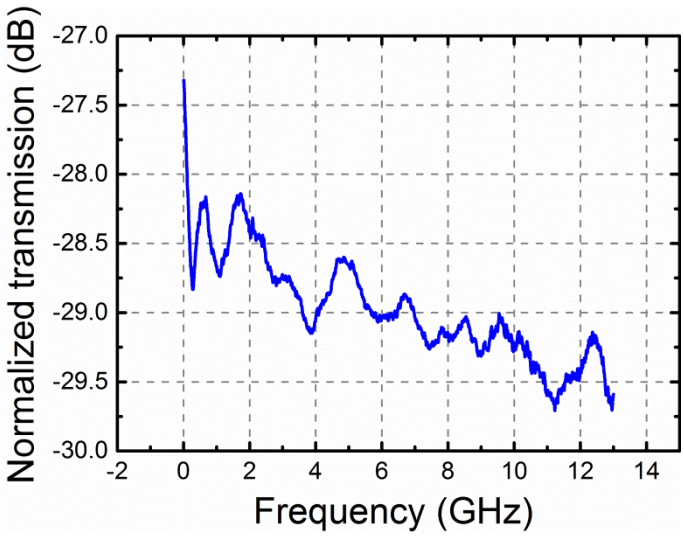

Fig.7.12 The normalized electro-optic bandwidth.

Secondly, eye-diagrams were measured with the setup as shown in Fig. 7.13. A signal generator (speed up to 12.5 Gb/s) and a 30 GHz oscilloscope are utilized to replace the network analyzer. Because the RF output of the detector is low and the 30 GHz oscilloscope is not sensitive enough, two methods are used to increase the output RF signal: 1) A TDFA is used to pump up the total input light power; 2) A RF small signal amplifier is used to amplify the output RF signal. The images of the characterization platform are shown in Fig. 7.14.

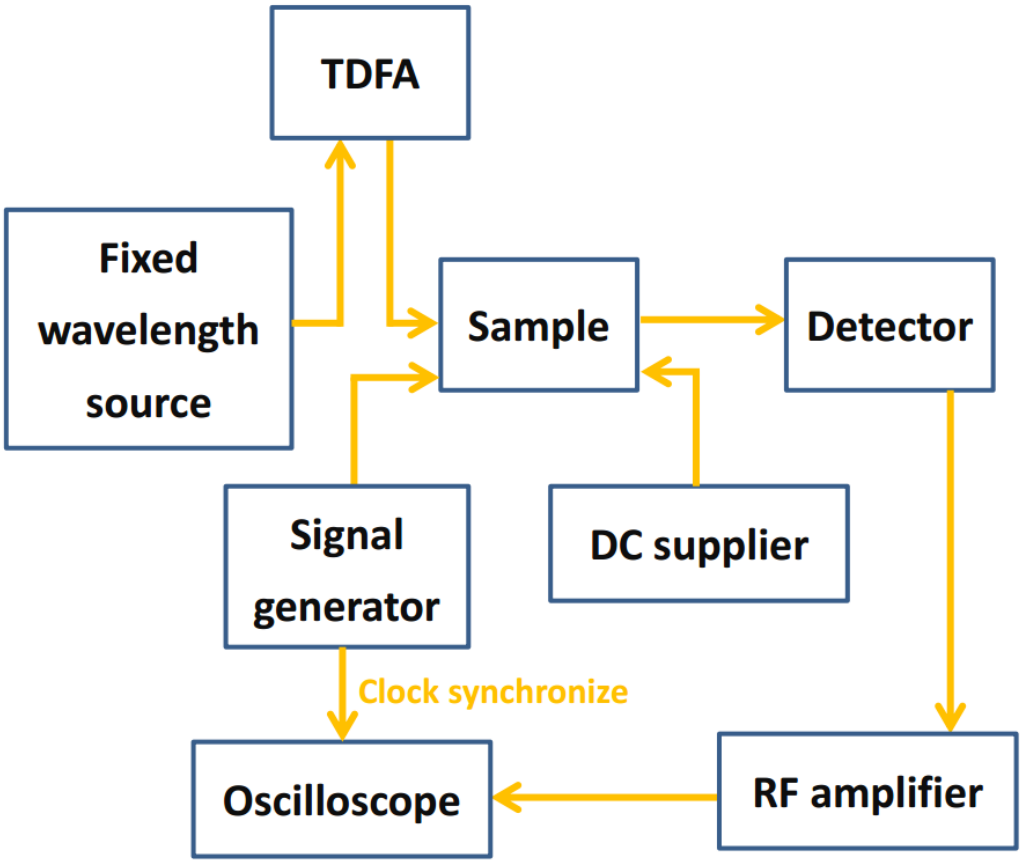

Fig.7.13 The characterization setup for measuring the eye-diagram.

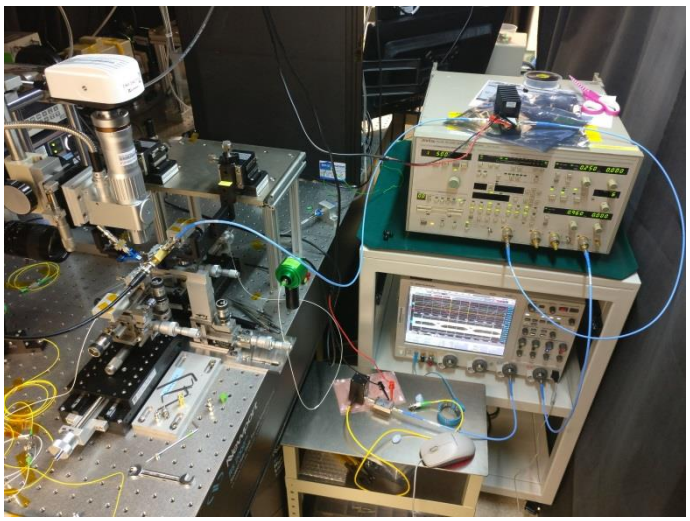

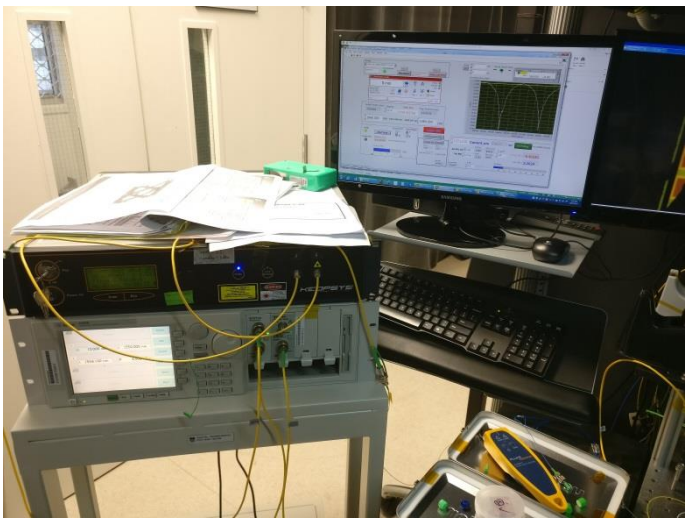

Fig.7.14 The images of the characterization platform for measuring the eye-diagrams.

The DC bias and the working wavelength are kept as -3 V and 1973.2 nm respectively. The measurements were performed using PRBS signal. The V_{pp} is set as 2 V. The eye-diagrams measured at the speed of 5 Gb/s, 7.5 Gb/s, 10 Gb/s and 12.5 Gb/s are shown in Fig. 7.15. The signal-to-noise ratio (SNR) at 12.5 Gb/s was calculated as 8.325.

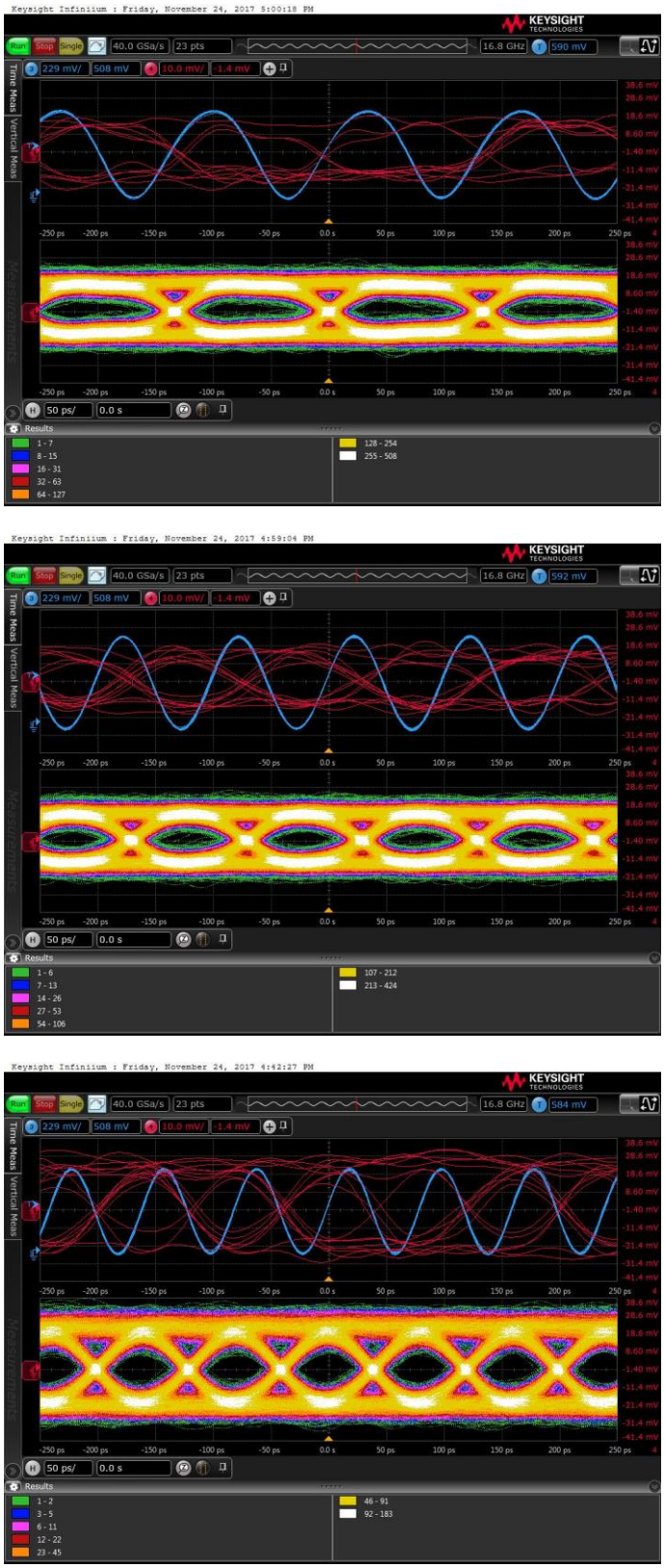

Fig.7.15 The eye-diagrams measured at the speed of 5 Gb/s, 7.5 Gb/s, 10 Gb/s and 12.5 Gb/s (from top to bottom).

7.6 Conclusion and Discussions

In this chapter, we designed, fabricated and characterized the microracetrack resonator based TO modulator and the MZI-based EO modulator. As characterized, the DC shifting rate and the -3 dB bandwidth of the TO modulator are 0.05 nm/V and ~30.8 KHz respectively. The -3 dB bandwidth of the EO modulator is measured as >12.5 GHz. The eye-diagrams at the speed of 5 Gb/s, 7.5 Gb/s, 10 Gb/s and 12.5 Gb/s are measured. And the SNR at 12.5 Gb/s was calculated as 8.325. Although the performances of these modulators are not as good as the reported works at the NIR communication band so far, they pave the way for extending the communication operating wavelength to the MIR band.

References

[1] T. Baehr-Jones, R. Ding, Y. Liu, A. Ayazi, T. Pinguet, N. C. Harris, M. Streshinsky, P. Lee, Y. Zhang, and A. E.-J. Lim, "Ultralow drive voltage silicon traveling-wave modulator," *Opt. Express*, vol. 20, pp. 12014–12020, 2012.

[2] A. Novack, Y. Liu, R. Ding, M. Gould, T. Baehr-Jones, Q. Li, Y. Yang, Y. Ma, Y. Zhang, K. Padmaraju, K. Bergmen, A. E.-J. Lim, G.-Q. Lo, and M. Hochberg, "A 30 GHz silicon photonic platform," in *SPIE Optics Optoelectronics,* (SPIE, 2013), pp. 878107.

[3] Q. Xu, S. Manipatruni, B. Schmidt, J. Shakya, and M. Lipson, "12.5 Gbit/s

carrier-injection-based silicon microring silicon modulators," *Opt. Express*, vol. 15, no. 2, pp. 430–436, 2007.

[4] X. Zheng, J. Lexau, Y. Luo, H. Thacker, T. Pinguet, A. Mekis, G. Li, J. Shi, P. Amberg, N. Pinckney, K. Raj, R. Ho, J. E. Cunningham, and A. V. Krishnamoorthy, "Ultra-low-energy all-CMOS modulator integrated with driver," *Opt. Express*, vol. 18, no. 3, pp. 3059–3070, 2010.

[5] N. C. Harris, Y. Ma, J. Mower, T. B.-Jones, D. Englund, M. Hochberg, and C. Galland, "Efficient, compact and low loss thermo-optic phase shifter in silicon," *Opt. Express*, vol. 22, pp. 10487-10493, 2014.

[6] B. Pile and G. Taylor, "Small-signal analysis of microring resonator modulators," *Opt. Express*, vol. 22, pp. 14913-14928, 2014.

[7] Q. Xu, B. Schmidt, S. Pradhan, and M. Lipson, "Micrometre-scale silicon electro-optic modulator," *Nature*, vol. 435, pp. 325-327, 2005.

[8] G. Reed, G. Mashanovich, F. Y. Gardes, M. Nedeljkovic, Y. Hu, D. J. Thomson, K. Li, P. R. Wilson, S.-W. Chen, and S. S. Hsu, "Recent breakthroughs in carrier depletion based silicon optical modulators," *Nanophotonics*, vol. 3, pp. 229-245, 2014

[9] M. Pantouvaki, H. Yu, M. Rakowski, P. Christie, P. Verheyen, G. Lepage, N. V. Hoovels, P. Absil, and J. V. Campenhout, "Comparison of Silicon Ring Modulators With Interdigitated and Lateral p-n Junctions," *IEEE Journal of Selected Topics in Quantum Electronics*, vol. 19, no. 2, pp. 7900308-7900308,

2013.

[10] D. J. Thomson, F. Y. Gardes, Y. Hu, G. Mashanovich, M. Fournier, P. Grosse, J-M. Fedeli, and G. T. Reed, "High contrast 40Gbit/s optical modulation in silicon," *Opt. Express*, vol. 19, pp. 11507-11516, 2011.

[11] B. Jalali and S. Fathpour, "Silicon photonics," *IEEE J. Lightwave Technol.*, vol. 24, pp. 4600–4615, 2006.

[12] M. Nedeljkovic, R. Soref, and G. Z. Mashanovich, "Free-Carrier Electrorefraction and Electroabsorption Modulation Predictions for Silicon Over the 1–14 μm Infrared Wavelength Range," *IEEE Photonics Journal*, vol. 3, no. 6, pp. 1171-1180, 2011.

[13] I. Rendina, "Thermo-optical modulation at 1.5m in silicon etalon," *Electron. Lett.*, vol. **28**, no. 1, pp. 83–85, 1992.

[14] H. Xu, X. Li, Xiao Xi, Z. Li, Y. Yu and J. Yu, "High-speed and broad optical bandwidth silicon modulator," *Chinese Physics B*, vol. 22, no. 11, pp. 114212, 2013.

[15] Z. Xuan, Y. Ma, Y. Liu, R. Ding, Y. Li, N. Ophir, A. Eu-Jin Lim, G. Lo, P. Magill, K. Bergman, T. Baehr-Jones, and M. Hochberg, "Silicon microring modulator for 40 Gb/s NRZ-OOK metro networks in O-band," *Opt. Express*, vol. 22, no. 23, pp. 28284-28291, 2014.

[16] M. Li, X. Xiao, Q. Yang, and S. Yu, "40 Gbaud binary phase shift keying signal modulation using a substrate removed silicon modulator," *Modern Physics*

Letters B, vol. 31, no. 1740009, 2017.

[17] T. Baba, S. Akiyama, M. Imai, N. Hirayama, H. Takahashi, Y. Noguchi, T. Horikawa, and T. Usuki, "50-Gb/s ring-resonator-based silicon modulator," *Optics Express*, vol. 21, no. 10, pp. 11869-11876, 2013.

Chapter 8
Conclusions and Future Work

8.1 Conclusions

Silicon photonics has attracted a lot of research interests and been used in many applications, such as short-reach interconnects [1-4], signal processing [5-10], and bio-chemical sensors [11-14]. So far, majority of the research effort in Si photonics is focused on tele- and data- communication wavelengths between 1.3 and 1.6 μm. Besides, the mid-infrared (MIR, λ = 2 - 20 μm) regime is also a very crucial band as many molecules have unique absorption fingerprints in this regime. Hence there is considerable interest to realize practical passive and optoelectronic applications operating in the MIR range, such as optical sensing and environmental monitoring, free-space communications, bio-medical and thermal imaging [15-17]. 2 μm wavelength is also a promising solution to extend the operating wavelength of communication system to short MIR wavelengths. Therefore, MIR is a very useful wavelength regime which needs further exploration.

In this thesis, various silicon photonics devices operating at near-infrared (NIR) and mid-infrared (MIR) bands based on silicon-on-insulator (SOI) platform are designed, fabricated and characterized, including passive fundamental components, Fano and EIT devices, dual-band optical filters, sensors, and modulators. The main works of this thesis are summarized below:

Acting as the cornerstone of various silicon photonics devices, the fundamental building blocks operating at 2 μm wavelength, including waveguides, grating couplers and microring resonators, were optimized and fabricated for the first time. As characterized, the grating coupler operating at 2 μm wavelength was 6.5 dB, which is comparable to the widely used grating couplers operating at 1.55 μm communication band. The extinction ratio (ER) and the quality factor (Q factor) of the compact microring resonator (radius = 10 μm) integrated with above grating couplers were measured as 12 dB and 11200 respectively.

As one of the practical methods to improve the efficiency of sensors and modulators, Fano and electromagnetically-induced-transparency (EIT) devices were theoretically and experimentally demonstrated. For the first time, an EIT transmission lineshape was experimentally generated in the all-pass microring-Bragg grating coupled resonant system. And with the same system, the conversion between Fano and EIT transmission lineshape was experimentally verified and the inner mechanism was studied in detail. Furthermore, the tunable and convertible Fano and EIT transmission lineshapes were experimentally realized in the Mach–Zehnder interferometer (MZI)-assisted microring-Bragg grating based coupling resonant system for the first time.

Aside from the Fano and EIT transmission, the dual-band optical filter (DBOF), which possesses double modulating channels, can also dramatically increase the volume of signal processing. In this work, two kinds of DBOFs based on partially-reflective-element-embedded microring resonators were fabricated and analyzed,

including the DBOF based on a single microring resonator embedded with nanoholes and the DBOF based on a single microring resonator embedded with Bragg gratings. As measured, the separation between two resonance dips and the insertion loss are 0.5 nm and <0.5 dB respectively. The Q factors of the two dips achieve 30900 and 34400 respectively.

By taking the advantages of the suspended structure, which includes reducing the absorption of buried oxide (BOX) layer at MIR band and enhancing the interaction between mode field and chemicals under investigation, the bio-chemical sensor operating at 2 μm wavelength based on a suspended microracetrack resonator with sub-wavelength-grating (SWG) lateral metamaterial cladding is designed, fabricated and characterized for the first time. The expected sensitivities were calculated based on the specially developed numerical model with equivalent refractive index method. The expected sensitivity of the fundamental TE mode was calculated as 337.5 nm/RIU.

Based on the fundamental building blocks and with additional implantation and electrode fabrication processes, the thermal-optic (TO) and electro-optic (EO) modulators operating at 2 μm wavelength were experimentally demonstrated for the first time. As measured, the DC shifting rate and the -3 dB bandwidth of the TO modulator are measured as 0.05 nm/V and ~30.8 KHz respectively. The -3 dB bandwidth of the EO modulator is measured as >12.5 GHz. The eye-diagrams at the speed of 5 Gb/s, 7.5 Gb/s, 10 Gb/s and 12.5 Gb/s are measured. And the SNR at 12.5

Gb/s was calculated as 8.325.

8.2 Key Contributions

The motivation of this thesis is to design, fabricate and characterize the passive and active photonic devices operating at the NIR and the MIR bands based on SOI platform. The key contributions of this thesis include:

(1) The fundamental components operating at 2 μm wavelength, including the waveguides, grating couplers and microring resonators, were optimized, fabricated and measured for the first time. The performance of the grating couplers based on pitch, duty-cycle, etching depth, and input/output angle has been discussed in detail. The influences of the transmission coefficient on the Q factor and the ER of the microring resonator have been demonstrated. The microring resonators integrated with grating couplers have been fabricated and characterized. The experimental results and the simulation results are in good agreement. These fundamental components are well prepared for the more complicated photonics devices in the future.

(2) The EIT transmission was experimentally generated in the all-pass microring-Bragg grating coupled resonant system for the first time. The influence of five main parameters, including pitch, the number of Bragg grating periods, the corrugation depth of Bragg gratings, coupling coefficient, and the round-trip attenuation, have been simulated and analyzed. The group delay at the EIT peak

has been calculated based our specially designed numerical model to verify the EIT effect. Based on the same system, the tuning and conversion of EIT and Fano transmission was studied and experimentally verified. We found that the conversion depends on the coupling status of the microring resonator. By changing the gap width between the microring and the bus waveguide, the coupling status can be changed between over-coupling and under-coupling, which leads to various transmission spectra. Furthermore, the thermally tunable and convertible EIT and Fano transmission were theoretically and experimentally realized in the MZI-assisted microring-Bragg grating based coupling resonant system for the first time. We utilized the MZI-assisted structure to generate a tunable round-trip attenuation of the microring resonator. By tuning the optical path length of the MZI arm, the round-trip attenuation can be changed as well as the coupling status of the microring resonator. Then the tuning and the conversion between the EIT and Fano transmission can be obtained. Although the EIT and Fano devices mentioned in this PhD project only operates at 1.55 μm wavelength, the ideas and concepts can be referred to build the similar devices operating at MIR band. When transferring to MIR band, the dimensional parameters, such as the pitch, corrugation depth of Bragg gratings, and the waveguide width etc., need to be adjusted to be suitable for the longer wavelength.

(3) Two kinds of DOBFs were designed, fabricated and characterized for the first time, which includes the DBOF based on a single microring resonator embedded

with nanoholes and the DBOF based on a single microring resonator embedded with Bragg gratings. We consider that the interference between the F-P resonator, which is formed by the embedded partially reflective elements, and the microring resonator gives rise to the dual filtering transmission spectra. The dual filtering transmission spectra have double modulating channels, which can greatly increase the volume and the efficiency of signal processing. The experimental performance is comparable to the up-to-date reported works.

(4) The bio-chemical sensor operating at 2 μm wavelength based on a suspended microracetrack resonator with SWG lateral metamaterial cladding was designed, fabricated and characterized for the first time. The influences of the SWG pitch and the waveguide width on the propagation loss have been experimentally demonstrated. With the optimized suspended waveguides, we fabricated and tested the suspended microracetrack. The influence of three crucial factors, including the duty-cycle of SWG, the width and the thickness of waveguides, on the sensitivity have been calculated and analyzed with our specially designed numerical model. The expected sensitivity is comparable to the latest reported results at the NIR communication band.

(5) The TO and EO modulators operating at 2 μm wavelength were experimentally demonstrated for the first time. The microring-resonator-based TO modulator and the MZI-based EO modulator have been fabricated and characterized. Although the performances of these modulators are not as good as the reported works at the

NIR communication band so far, they pave the way for extending the communication operating wavelength to the MIR band.

8.3 Recommendations for Future Work

So far, various passive and active photonic devices have been theoretically and experimentally demonstrated in this thesis. In spite of the promising results that have been demonstrated in this work, there are some areas which can be improved. These are:

(1) By utilizing the developed Fano devices in building modulators, the efficiency of the modulators can be greatly improved. As the Fano transmission can offer more than 10-time larger extinction ratio (ER) than the conventional microring symmetric transmission lineshape with the same wavelength shift, the modulator can obtain a much larger on/off contrast. In another word, the same modulation depth can be achieved with a smaller wavelength shift as well as a lower bias voltage. As a result, the threshold voltage and the power consumption can be much lower.

(2) Since the EIT transmission possesses a narrow transparency peak (high quality factor) with a time delay, it can be utilized in building modulators and time delay lines. With the help of the narrow transparency peak and the high quality factor, the switching between on and off status can be realized with a very low bias

voltage and the modulation speed can be improved as well. Besides, by cascading the introduced EIT device, a large time delay can be obtained to provide a solution of building time delay lines.

(3) Through combining the Fano transmission and the suspended microracetrack resonator sensor, the sensitivity can be greatly improved. Since Fano transmission has the large ER and the sharp asymmetric lineshape, even a small shift of the resonant dip caused by a small change of the refractive index of the cladding layer can result in a large variation of the output light power. Consequently, the sensitivity and the sensing limitation can be improved a lot.

References

[1] M. J. R. Heck, H. Chen, A. W. Fang, B. R. Koch, D. Liang, H. Park, M. N. Sysak, and J. E. Bowers, "Hybrid Silicon Photonics for Optical Interconnects," *IEEE Journal of Selected Topics in Quantum Electronics*, vol. 17, no. 2, pp. 333-346, Mar. 2011.

[2] G. Roelkens, L. Liu, D. Liang, R. Jones, A. Fang, B. Koch, and J. E. Bowers, "III-V/silicon photonics for on-chip and intra-chip optical interconnects," *Laser & Photon. Rev*, vol. 4, pp. 751–779, 2010.

[3] T. Barwicz, H. Byun, F. Gan, C. W. Holzwarth, M. A. Popovic, P. T. Rakich, M. R. Watts, E. P. Ippen, F. X. Kärtner, H. I. Smith, J. S. Orcutt, R. J. Ram, V. Stojanovic, O. O. Olubuyide, J. L. Hoyt, S. Spector, M. Geis, M. Grein, and T.

Lyszczarz, and J. U. Yoon, "Silicon photonics for compact, energy-efficient interconnects [Invited]," *J. Opt. Netw.*, vol. 6, pp. 63-73, 2007.

[4] A. V. Krishnamoorthy, R. Ho, X. Zheng, H. Schwetman, J. Lexau, P. Koka, G. Li, Ivan Shubin, and J. E. Cunningham, "Computer Systems Based on Silicon Photonic Interconnects," *Proceedings of the IEEE*, vol. 97, no. 7, pp. 1337-1361, Jul. 2009.

[5] Q. Xu, B. Schmidt, S. Pradhan, and M. Lipson, "Micrometre-scale silicon electro-optic modulator," *Nature*, vol. 435, pp. 325-327, May, 2005.

[6] G. T. Reed and C. E. J. Png, "Silicon optical modulators," *Materialstoday*, vol. 8, no. 1, pp. 40-50, Jan. 2005.

[7] F. Y. Gardes, D. J. Thomson, N. G. Emerson, and G. T. Reed, "40 Gb/s silicon photonics modulator for TE and TM polarisations," *Opt. Express*, vol. 19, pp. 11804-11814, 2011.

[8] W. M. J. Green, M. J. Rooks, L. Sekaric, and Y. A. Vlasov, "Ultra-compact, low RF power, 10 Gb/s silicon Mach-Zehnder modulator," *Opt. Express*, vol. 15, pp. 17106-17113, 2007.

[9] A. Liu, L. Liao, D. Rubin, H. Nguyen, B. Ciftcioglu, Y. Chetrit, N. Izhaky, and M. Paniccia, "High-speed optical modulation based on carrier depletion in a silicon waveguide," *Opt. Express*, vol. 15, pp. 660-668 (2007)

[10] C. Batten, A. Joshi, J. Orcutt, A. Khilo, B. Moss, C. W. Holzwarth, M. A. Popovi, H. Li, H. I. Smith, J. L. Hoyt, F. X. Kartner, R. J. Ram, V. Stojanovic, and K.

Asanovic, "Building Many-Core Processor-to-DRAM Networks with Monolithic CMOS Silicon Photonics," *IEEE Micro*, vol. 29, no. 4, pp. 8-21, Jul. 2009

[11] A. Densmore, D.-X. Xu, P. Waldron, S. Janz, P. Cheben, J. Lapointe, A. Delâge, B. Lamontagne, J. H. Schmid, and E. Post, "A Silicon-on-Insulator Photonic Wire Based Evanescent Field Sensor," *IEEE Photonics Technology Letters*, vol. 18, no. 23, pp. 2520-2522, Dec.1, 2006.

[12] F. Dell'Olio and V. M. N. Passaro, "Optical sensing by optimized silicon slot waveguides," *Opt. Express*, vol. 15, pp. 4977-4993, 2007.

[13] M. Iqbal, M. A. Gleeson, B. Spaugh, F. Tybor, W. G. Gunn, M. Hochberg, T. Baehr-Jones, R. C. Bailey, and L. Cary Gunn, "Label-Free Biosensor Arrays Based on Silicon Ring Resonators and High-Speed Optical Scanning Instrumentation," *IEEE Journal of Selected Topics in Quantum Electronics*, vol. 16, no. 3, pp. 654-661, May, 2010.

[14] Y. Chen, H. Lin, J. Hu, and M. Li, "Heterogeneously Integrated Silicon Photonics for the Mid-Infrared and Spectroscopic Sensing," *ACS Nano*, vol. 8, no. 7, pp. 6955-6961, 2014.

[15] G. Z. Mashanovicha, S. Stankovicb, P. Y. Yanga, E. J. Teoc, F. Dell'Oliod, V. M. N. Passarod, A. A. Bettiolc, M. B. H. Breesec, G. T. Reeda, "Silicon waveguides for the mid-infrared wavelength region," *Proc. of SPIE.*, vol. 6898, no. 68980T, pp. 1-7, 2008.

[16] R. W. Waynant, I. K. Ilev and I. Gannot, "Mid-infrared laser applications in

medicine and biology," *Phil. Trans. R. Soc. Lond. A* , vol. 359, pp. 635–644, 2001.

[17] F. K. Tittel, D. Richter, and A. Fried, "Mid-infrared laser applications in spectroscopy," *Solid-State Mid-Infrared Laser Sources, Topics Appl. Phys.*, vol. 89, pp. 445–510, 2003.

List of Publications

Journal Papers:

1. Zecen Zhang, Geok Ing Ng, Ting Hu, Haodong Qiu, Xin Guo, Mohamed Saïd Rouifed, Chongyang Liu, and Hong Wang, "Electromagnetically induced transparency-like effect in microring-Bragg gratings based coupling resonant system," *Opt. Express*, vol. 24, pp. 25665-25675, 2016.

2. Zecen Zhang, Geok Ing Ng, Haodong Qiu, Wanjun Wang, Xin Guo, Mohamed S. Rouifed, Chongyang Liu, and Hong Wang, "Compact microring resonators integrated with grating couplers working at 2 μm wavelength on silicon-on-insulator platform," *Appl. Opt.*, vol. 56, pp. 5444-5449, 2017.

3. Zecen Zhang, Geok Ing Ng, Haodong Qiu, Wanjun Wang, Xin Guo, Mohamed S. Rouifed, Chongyang Liu, and Hong Wang, "Conversion between EIT and Fano spectra in a microring-Bragg grating coupled-resonator system," *Appl. Phys. Lett.*, vol. 111, pp. 081105, 2017.

4. Zecen Zhang, Geok Ing Ng, Ting Hu, Haodong Qiu, Xin Guo, Wanjun Wang, Mohamed S. Rouifed, Chongyang Liu, Jiaxu Sia, Jin Zhou, Callum G. Littlejohns, Milos Nedeljkovic, Graham T. Reed, and Hong Wang, "Experimental Demonstration of Thermally Tunable Fano and EIT Resonances in Coupled Resonant System on SOI Platform," submitted to *IEEE Photonics Journal*.

5. Zecen Zhang, Geok Ing Ng, Ting Hu, Haodong Qiu, Xin Guo, Wanjun Wang, Mohamed S. Rouifed, Chongyang Liu, Jiaxu Sia, Jin Zhou, Callum G. Littlejohns, Graham T. Reed, and Hong Wang, “Mid-infrared sensor based on suspended microracetrack resonator with lateral sub-wavelength-grating metamaterial cladding,” *IEEE Photonics Journal*, vol. 10, no. 2, pp. 6801608, 2018.

6. Ting Hu, Haodong Qiu, Zecen Zhang, Xin Guo, Chongyang Liu, Mohamed S. Rouifed, Callum G. Littlejohns, Graham T. Reed, and Hong Wang, “A Compact Ultrabroadband Polarization Beam Splitter Utilizing a Hybrid Plasmonic Y-Branch,” *IEEE Photonics Journal*, vol. 8, no. 4, pp. 1-9, 2016.

7. Mohamed S. Rouifed, Callum G. Littlejohns, Guo Xin Tina, Qiu Haodong, Ting Hu, Zecen Zhang, Chongyong Liu, Graham T. Reed, and Hong Wang, "Low Loss SOI Waveguides and MMIs at the MIR Wavelength of 2 μm," *IEEE Photonics Technology Letters*, vol. 28, no. 24, pp. 2827-2829, 2016.

8. Mohamed S. Rouifed, Callum G. Littlejohns, Guo Xin Tina, Haodong Qiu, Jordi Soler Penades, Milos Nedeljkovic, Zecen Zhang, Chongyong Liu, David J. Thomson, Goran Z. Mashanovich, Graham T. Reed, and Hong Wang, "Ultra-compact MMI-based beam splitter demultiplexer for the NIR/MIR wavelengths of 1.55 μm and 2 μm," *Opt. Express*, vol. 25, pp. 10893-10900, 2017.

9. Xiaocong Yuan, Zhenwei Xie, Ting Lei, Fan Li, Haodong Qiu, Zecen Zhang, Hong Wang, Changjun Min, Luping Du, and Zhaohui Li, “Ultra-broadband On-

chip Twisted Light Emitter for Optical Communications," accepted by *Light: Science & Applications*

Conference Papers:

1. Zecen Zhang, Geok Ing Ng, Ting Hu, Haodong Qiu, Xin Guo, Mohamed S. Rouifed, Chongyang Liu, and Hong Wang, "The Switchable EIT-like and Fano Resonances in Microring-Bragg Grating Based Coupling Resonant System," in *Conference on Lasers and Electro-Optics*, 2017.
2. Zecen Zhang, Geok Ing Ng, Haodong Qiu, Xin Guo, Wanjun Wang, Mohamed S. Rouifed, Chongyang Liu, and Hong Wang, "Dual-band optical filter based on a single microring resonator embedded with nanoholes." in *Conference on Lasers and Electro-Optics Pacific Rim*, 2017.
3. Zecen Zhang, Geok Ing Ng, Haodong Qiu, Xin Guo, Wanjun Wang, Mohamed S. Rouifed, Chongyang Liu, and Hong Wang, "Dual-band optical filter based on a microracetrack resonator embedded with Bragg gratings." in *Proceedings of the Optofluidics*, 2017.
4. Wanjun Wang, Zecen Zhang, Xin Guo, Jin Zhou, Sia Jia Xu Brian, Mohamed S. Rouifed, Chongyang Liu, Callum G. Littlejohns, Graham T. Reed, and Hong Wang, "Mid-infrared (MIR) Mach-Zehnder Silicon Modulator at 2 μm Wavelength based on Interleaved PN Junction," in *The Optical Networking and Communication Conference & Exhibition*, 2018.
5. Wanjun Wang, Haodong Qiu, Zecen Zhang, Xin Guo, Sia Jia Xu Brian,

Mohamed S. Rouifed, Chongyang Liu, and Hong Wang, "Integrated Optical Mode Converter for Mid Infra-red (MIR) Mode-division Multiplexing System," in *The 7th International Multidisciplinary Conference on Optofluidics*, 2017.

6. Mohamed S. Rouifed, Callum G. Littlejohns, Xin Guo, Haodong Qiu, Jordi Soler Penades, Milos Nedeljkovic, Zecen Zhang, Wanjun Wang, Chongyang Liu, David J. Thomson, Goran Z. Mashanovich, Graham T. Reed, and Hong Wang, “Hybrid NIR/MIR silicon photonics passive devices,” in *Proceedings of the Optofluidics*, 2017.

7. Ting Hu, Haodong Qiu, Xin Guo, Zecen Zhang, Chongyang Liu, Hong Wang, "Four port mode-selective optical router based on silicon-on-insulator microring resonators", in *Advanced Optical Manufacturing and Testing Technologies*, 2016.